CHALMERS

Towards Full Predictions of the Unsteady Incompressible Flow in Rotating Machines, Using OpenFOAM

OLIVIER PETIT

Department of Applied Mechanics
Division of Fluid Dynamics
CHALMERS UNIVERSITY OF TECHNOLOGY
Gothenburg, Sweden 2012

Towards Full Predictions of the Unsteady Incompressible Flow in Rotating Machines, Using OpenFOAM

OLIVIER PETIT

Cover:
Axial Velocity component of the computed unsteady flow in the U9 Kaplan runner and
draft tube. Blue represents the lowest velocity and red the highest.

Towards Full Predictions of the Unsteady Incompressible Flow in Rotating Machines, Using OpenFOAM

OLIVIER PETIT
Department of Applied Mechanics
Division of Fluid Dynamics
Chalmers University of Technology

Abstract

The main objective of the present work is to validate methodologies for accurate numerical predictions of the incompressible flow of water in the U9 Kaplan turbine model. The term "prediction" implies that the use of detailed experimental data for boundary conditions should be avoided, and that all important features of the studied case should be included. That includes specifying boundary conditions at locations where the flow conditions can be easily estimated, and where reasonable variations in those estimations do not significantly affect the flow prediction. As an example, the U9 Kaplan turbine model has a sharply bent inlet pipe, and it is here argued that the secondary flow from that should be taken into account by including the pipe in the simulation. In the case of rotating machines, such as the U9 Kaplan turbine model, the interaction between rotating and stationary components (rotor-stator interaction) is a feature that must be included in the simulations.

Three highly relevant well-documented cases have been used in the present work, the ERCOFTAC Centrifugal Pump, the Timisoara Swirl Generator and the U9 Kaplan turbine model. All three cases include rotor-stator interaction. The latter, being the main goal of the studies, has just recently been studied experimentally and is a computationally demanding case. Thus, the former two cases were used while validating the new implementations and evaluating the numerical settings, until the results were reliable and efficient. Two rotor-stator interaction methods were investigated, the steady-state frozen-rotor approach, and the unsteady sliding grid approach, and the results from four turbulence models were compared.

The results show that both approaches can be used to couple the rotating and stationary parts of the domain. However, the frozen rotor yields an unphysical advection of the runner wakes, and such results should only be used for a first estimation or as initial conditions for full unsteady sliding grid simulations. The predictions compare very well with the experimental results, and the main differences can be explained by the geometrical simplifications that were made. The four turbulence models behave similarly, with a minor preference for different models in the different cases.

The present work is done using the OpenFOAM OpenSource CFD toolbox. The code is chosen to facilitate an OpenSource distribution of the developments, to be shared in the scientific community, and to be directly useful in industry. It was not possible to achieve the results presented here with OpenFOAM before the start of the present work, which has significantly contributed to the validation of, and trust in, the new implementations.

Keywords: OpenFOAM, CFD, Kaplan Turbine, Hydro Power, Sliding Grid, Turbulent Flow

Empty your mind, be formless.
Shapeless, like water.
If you put water into a cup, it becomes the cup.
You put water into a bottle and it becomes the bottle.
You put it in a teapot it becomes the teapot.
Now, water can flow or it can crash.
Be water my friend.
Bruce Lee

Acknowledgements

Nomenclature

Latin symbols

$\dot{M}$	Mass flow
$\tilde{C}_p$	Static pressure coefficient
A	Area
A_0, A_S	Model Constants
b	Blade span
$C_{\varepsilon 1}, C_{\varepsilon 2}, C_\mu$	Model Constants
D	Diameter
E	Potential energy
g	Gravitational acceleration
G_i	Circumferential pitch
H, h	Head
k	Turbulent kinetic energy
l	Impeller chord length
n	Rotational speed
P	Time-averaged pressure quantity
p	Pressure
P_h	Hydraulic power
P_e	Electric power
P_k	Production term
Q	Volume flow rate
R	Radius
r	Radial coordinate
S_{ij}	Strain rate tensor
T_i	Rotor blade passing period
U_i, U_j	Time-averaged velocity quantity
u_i, u_j	Velocity vector
W_r	Radial velocity
W_u	Tangential velocity
x_i, x_j	Spatial coordinates
y_i	Circumferential coordinate in the relative frame
z	Number of blades

Greek symbols

α_1, α_2	Model constants
β, β_1, β^*	Model constants
δt	Time step
δ_{ij}	Kronecker delta tensor
η_0	Model constant
η_h	Hydraulic efficiency
μ	Dynamic molecular viscosity
μ_t	Dynamic eddy-viscosity (turbulent viscosity)
ν	Kinematic molecular viscosity
ν_t	Kinematic eddy-viscosity (turbulent viscosity)
ω	Specific dissipation rate
Ω_{ij}	Rotation tensor
ϕ	Generic model coefficient
Ψ	Total pressure rise coefficient
ρ	Fluid density
$\sigma_k, \sigma_\varepsilon, \sigma_\omega$	Model constants
τ_{ij}	Reynolds stress tensor
ε	Kinetic energy dissipation rate
ε_{ijk}	Levi-Civita symbol
φ	Flow rate coefficient

Mathematical operators and symbols

$(\cdot)'$	Fluctuating quantity
∇	Gradient operator
$\overline{(\cdot)}$	Time-averaged quantity
∂	Partial derivatives

Abbreviations

BEP	Best Efficiency Point
CFD	Computational Fluid Dynamics
CPU	Central Processing Unit
DES	Detached Eddy Simulation
DNS	Direct Numerical Simulation
ECP	ERCOFTAC Centrifugal Pump
ERCOFTAC	European Research Community on Flow, Turbulence and Combustion
FOAM	Field Operation And Manipulation
GGI	General Grid Interface
GPL	General Public License
LES	Large Eddy Simulation
MFR	Multiple Frame of Reference
RANS	Reynolds Averaged Navier-Stokes
RNG	ReNormalization Group

SST	Shear Stress Transport
TSG	Timisoara Swirl Generator
URANS	Unsteady Reynolds Average Navier-Stokes

x

List of Publications

This thesis consists of an extended summary and the following appended papers:

Paper I   O. Petit, M. Page, M. Beaudoin and H. Nilsson. "The ERCOFTAC Centrifugal Pump OpenFOAM Case-Study", *3rd IAHR International Meeting of the Workgroup on Cavitation and Dynamic Problems in Hydraulic Machinery and Systems - Brno (2009)*

               Division of work: Petit produced all the numerical results and wrote the paper. Page provided background knowledge and experiences for the studied case. Beaudoin implemented the GGI interface and provided that technical description. Nilsson supervised the planning, performance analysis and writing. All authors proofread the final paper.

Paper II   O. Petit, B. Mulu, H. Nilsson, and M. Cervantes. "Comparison of Numerical and Experimental Results of the Flow in the U9 Kaplan Turbine Model", *25th Symposium on Hydraulic Machinery and Systems - Timisoara (2010)*

               Division of work: Petit produced all the numerical results and wrote the paper. Mulu provided the experimental results and the description of the experimental method. Nilsson and Cervantes supervised the planning, performance analysis and writing. All authors proofread the final paper.

Paper III   O. Petit, A.I. Bosioc, H. Nilsson, S. Muntean and R.F. Susan-Resiga. "Unsteady Simulations of the Flow in a Swirl Generator, Using OpenFOAM", *International Journal of Fluid Machinery and Systems (2011)*, vol.4, pp. 199-208

               Division of work: Petit produced all the numerical results and wrote the paper. Muntean provided the geometry for the studied case. Bosioc provided the experimental results and the description of the experimental method. Nilsson and Susan-Resiga supervised the planning, performance analysis and writing. All authors proofread the final paper.

Paper IV   O. Petit and H. Nilsson. "Numerical Investigations of Unsteady Flow in a Centrifugal Pump with a Vaned Diffuser", *Submitted for journal publication.*

Division of work: Petit produced all the numerical results and wrote the paper. Nilsson supervised the planning, performance analysis and writing. Both authors proofread the final paper.

Paper V   O. Petit and H. Nilsson. "Towards a Full Prediction of the 3D Unsteady Flow in the U9 Kaplan Turbine Model", *Submitted for journal publication.*

Division of work: Petit produced all the numerical results and wrote the paper. Nilsson supervised the planning, performance analysis and writing. Both authors proofread the final paper.

Contents

Chapter 1

Introduction

Since Michael Faraday discovered how to generate electricity in the 1820s, its use has taken a very important role in our day-to-day life. Both population growth and increasing standards of living in developing countries cause strong growth in energy demand, especially cleanly-generated electricity, according to the International Energy Agency [1].

Figure 1.1 shows the production of electricity in the last three decades. Just for the year 2010, the Global Energy Intelligence [2] announced a worldwide growth of 5% in energy and predicted a growth of 1.5% per year over the next 30 years. With the human impact on climate change becoming evident in recent years and the prospect of lacking fossil fuels in the coming decades, the development of infrastructure and technologies that minimize social and environmental impacts represents a huge challenge for mankind. As a solution, the contribution of renewable electric energy is expected to grow in the future [1].
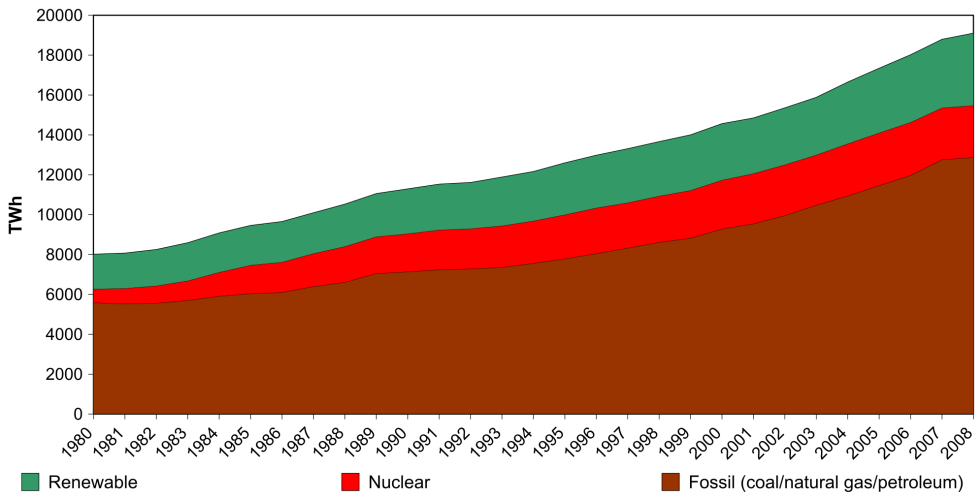
Figure 1.1: Annual net electricity generation in the world [1]

Figure 1.2 shows the generation of electricity from renewable sources over the past three decades. Hydro power is currently the most common form of renewable energy and plays a very important part in global electric power generation. It was at the end of the 19th century that hydro power started to be used to generate electricity [3]. The technology of today is thus a result of 100 years of development. Hydro electric power is a unique technology, giving a possibility to store the energy in a reservoir and extract the power on demand with very high efficiency. The impact on the environment of an existing hydro power plant is minimal and, while in production, a hydraulic turbine does not produce emissions or leave behind waste. Hydro power provides about 17.5% of the world's electricity, accounting for almost 85% of the electricity from renewable sources [4]. In Europe and North America, most of the hydroelectric potential is exploited. In Asia, on the other hand, only a small part of the hydroelectric potential is exploited. Many hydro power plants are being built, and the contribution of hydro power in Asia is expected to grow considerably over the next 30 years [5].
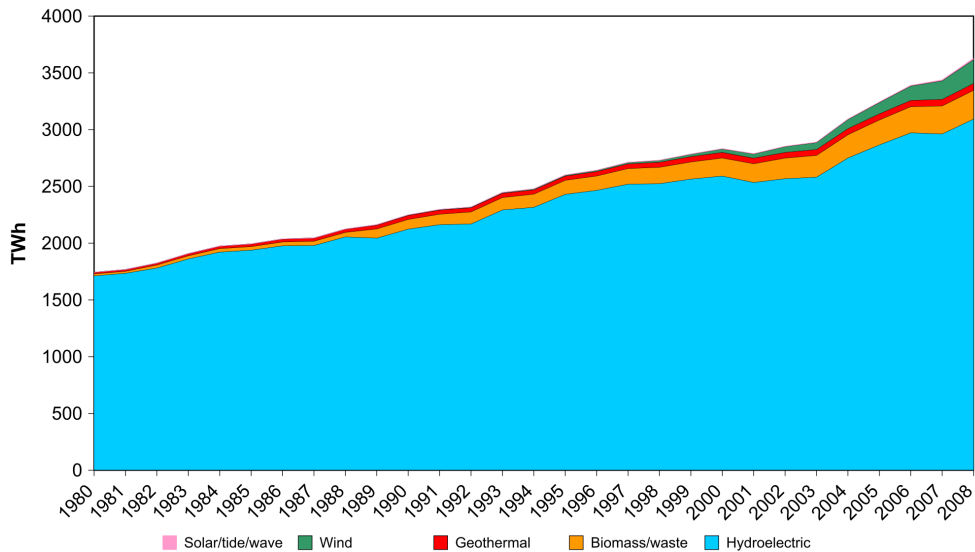
Figure 1.2: Annual net electricity generation from renewable energy in the world [1]

1.1 The Changing Role of Hydro Power

Due to the impact of climate change, the use of renewable energy is becoming very popular. Governmental incentives, and a great amount of research, allow the use of new technologies to generate clean energy. In Sweden, for example, the energy agency plans to build wind turbine parks regrouping more than 500 wind turbines by the end of 2020, dramatically increasing the contribution of wind power in Sweden. However, most forms of renewable energy, such as wind, solar or tidal energy are intermittent sources of energy.

Wind turbines provide energy only when the wind blows. In contrast, other technologies such as coal and nuclear power plants generate energy continuously and can not be used for regulating the intermittent sources. Hydro power is a unique way of generating energy, as water can be stored and used to generate energy on demand. As the use of intermittent renewable energy increases, the flexibility of hydro power will gain greater importance [5]. However, this flexibility in turn creates stress on the water turbines. Initially built to run as a base load, the hydro turbines are designed to be constantly running at their best efficiency point. The new role of hydro power brings a significant increase in off-design operation, load variations and start-stops, which is harmful to the hydro turbine.

1.2 Overview of Hydro Power Plants

An overview of a hydro power plant is shown in Fig. 1.3. When water is stored in a dam, its kinetic energy is negligible compared to its potential energy. The available hydraulic power, P_h [W], results from the product of the mass flow, $\dot{M} = \rho Q$, and the specific potential energy, $E = g.H$, where Q $[m^3/s]$ is the volume flow, ρ $[kg/m^3]$ is the density of the water and H [m] is the static head, i.e. the height difference between the head and the tail water, see Fig. 1.3. The hydraulic power is then given by $P_h = \dot{M} * E = \rho g Q H$. The actual electric power, P_e [W], that can then be generated from hydraulic power is $P_e = P_h * \eta_h = \eta_h \rho g Q H$, where η_h [-] is the hydraulic efficiency. The power of a hydro power station is thus directly related to the static head and to the flow rate of the water in the turbine, and, for a given head and flow rate, the type of turbine that will be used in the hydro power plant will vary. If the static head is low, the volume flow (or discharge) through the turbine will be optimized to generate maximum electrical power. Thus, low head turbines often have a large diameter (up to several meters).

There are two main categories of turbine designs:

- Impulse turbines, such as waterwheels or Pelton turbines. Impulse turbines convert the potential energy of the water into kinetic energy. In the case of the Pelton turbine, this is achieved through a convergent section (high-speed nozzle). The nozzle is placed in front of the Pelton turbine. The water exits the nozzle at very high speed, which creates a change of momentum when it hits the buckets of the Pelton turbine and in turn generates the motion of the turbine. The Pelton turbine does not need a house and operates in open air. The Pelton turbine is the most common type of impulse turbine and usually operates for a very high static head ($H > 400$ m).

- Reaction turbines, such as the Francis turbine, Kaplan turbine, propeller or bulb. To work properly, a reaction turbine needs to be submerged in water. The pressure difference and the kinetic energy are used to generate the rotation motion of the turbine. The pressure difference between the suction side and pressure side of the turbine blades forces the turbine to react and find an equilibrium, and thus rotate.

Reaction turbines are the most commonly used turbines in Europe and North America, particularly the Kaplan turbine and the Francis turbine. An overview of those two types of turbine is shown in Fig. 1.4. The static head and the volume flow control the selection

of the turbine for each given hydro power plant. Kaplan turbines are commonly used for a low static head, up to 70 m, while, for the Francis turbines, the head can vary between 10 and several hundred meters. The present work studies the flow through a Kaplan turbine. Thus further details on the Kaplan turbine are given in the following section.
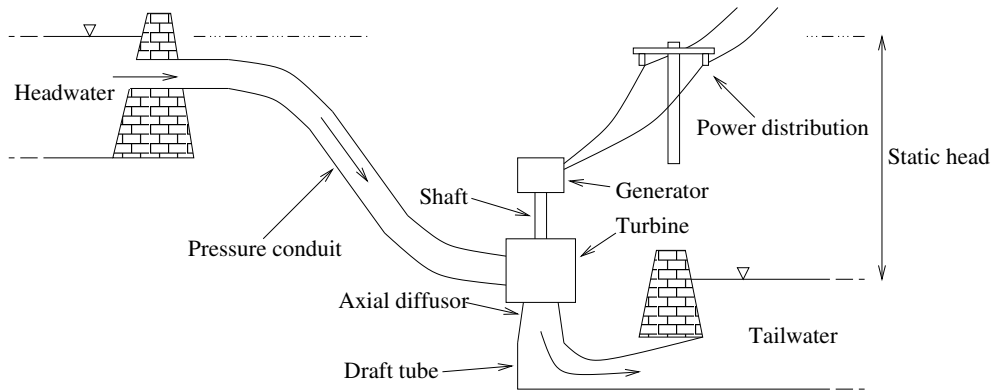
Figure 1.3: Overview of a hydraulic power plant
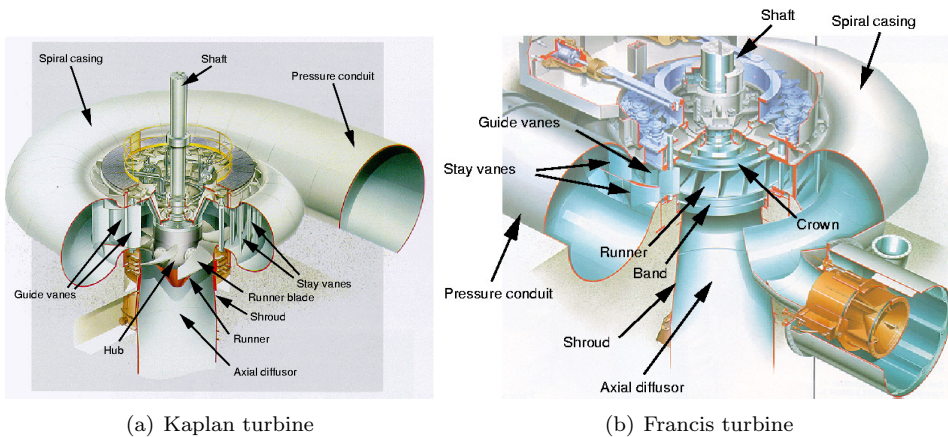
(a) Kaplan turbine   (b) Francis turbine

Figure 1.4: Overview of the two main turbine designs

1.3 The Kaplan Turbine

The Kaplan turbine was invented in 1913 by Victor Kaplan in Brno, Czechoslovakia. In 1924, the first large Kaplan turbine was installed in a hydro power plant in Lilla Edet, Sweden. It had a runner diameter of 5.2 m for a static head of 6.5 m and generated about 8 MW. Kaplan turbines are now widely used world wide for their low-head, high discharge power production. The different parts of the Kaplan turbine are listed below.

- The spiral casing. An example of the spiral casing geometry is shown in Fig. 1.5. Its purpose is to distribute the water flow evenly over the circumference of the runner inlet and to create a swirl. The spiral casing, together with the diffuser, changes part of the available head into a moment of momentum that provides torque to the runner.
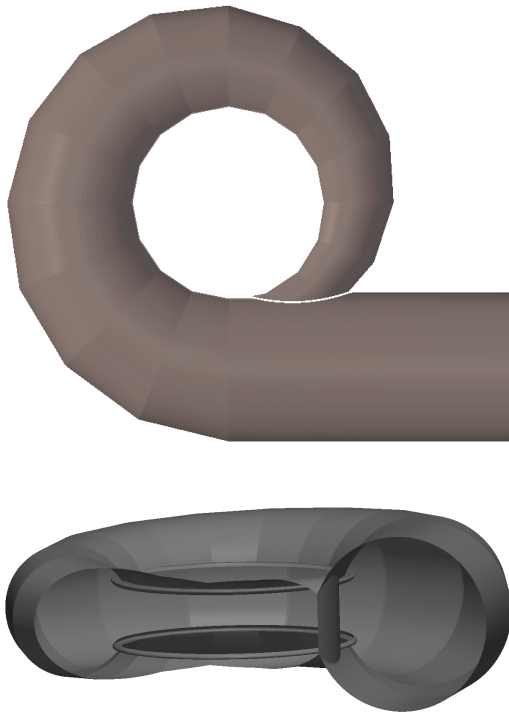
Figure 1.5: Example of a spiral casing for a Kaplan turbine

- The stay and guide vanes. An example of the stay and guide vanes geometry is shown in Fig. 1.6. The stay and guide vanes consist of 20 to 32 wing designed profile vanes that help to create a swirl flow and guide the flow tangentially towards the runner. The stay vanes act as a support for construction and ensure the stability of the spiral casing. The guide vanes are mounted on hydraulic pistons that can

change the blades' angle of attack at any time, changing the runner inlet flow area, and thus the volume flow. It is the guide vanes that regulate the flow and, as such, regulate the electricity production in the hydro power plant.
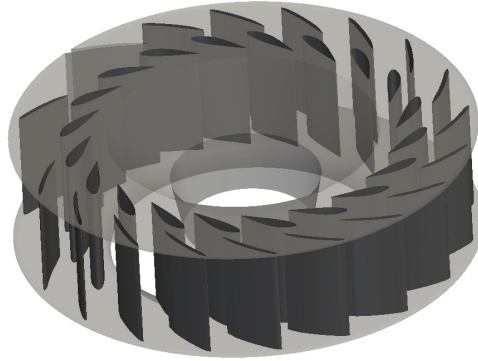
Figure 1.6: Example of the guide and stay vanes geometry for a Kaplan turbine

- The Kaplan runner. An example of a Kaplan runner geometry is shown in Fig. 1.7. This is the part where most of the total energy is converted into mechanical energy. Almost all the swirl entering the runner is removed as it flows through the runner. Usually equipped with four to eight blades, the Kaplan runner is a propeller with adjustable blades. The advantage is the higher efficiency over a wider operating range. Contrary to the propeller design, the Kaplan runner can operate at a variable hydraulic power, P_h (that is to say different discharge or static head), without losing efficiency. However, a small gap at the runner blades' end and the casing end need to be included to allow the blade to rotate. This in turn induces a leakage flow that decreases the efficiency of the runner.
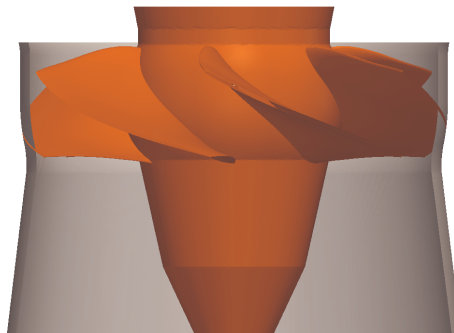
Figure 1.7: Example of a Kaplan runner geometry

- The draft tube. An example of a draft tube for a Kaplan runner is shown in Fig. 1.8. Located downstream of the runner, its purpose is to reduce the velocity of the flow with as minimum an energy loss as possible. The remaining kinetic energy of the flow is thus converted back to potential energy. The draft tube is a region where large unsteadiness occurs, and the design of the draft tube is crucial to the efficiency of the Kaplan runner.
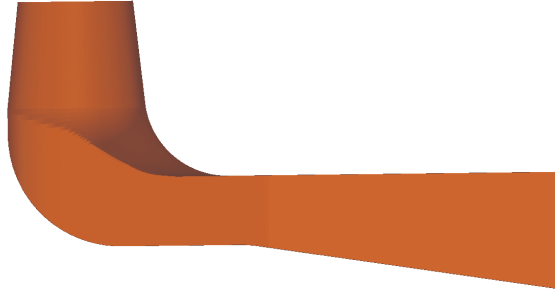
Figure 1.8: Example of a draft tube geometry for a Kaplan turbine

1.4 The Porjus Hydro Power Plant

Sweden is one of ten largest hydroelectric producers in the world, and the second largest in western Europe, after Norway. Most of its potential is harvested, and the average annual capability covers about 72% of the economic potential [5]. Hydro electricity production covers about 50 % of the generation of electricity. Similar to its European neighbor and North America, Sweden has largely ceased its construction of new hydro plants, owing to environmental and political considerations. The increase in hydro power electricity in Sweden thus mainly comes from small hydro projects and refurbishment of old hydraulic power plants. A better design for the hydro turbine often creates a gain in efficiency that represents a significant increase of the production capability.

The life of a hydraulic power plant is generally longer than that of any other power plants. Some power plants have run more than 100 years. Although the dam itself stays unchanged, the water turbines become damaged due for example to cavitation problems or vibration in the shaft between the turbine and the generator. Owing to those diverse issues, some turbine parts need to be replaced. With time come new technology and new designs. Fitting such new designs in an old power house can be a challenge, and sometimes solutions are found that are not beneficial to the flow in the turbine.

This is the case for the Porjus hydraulic power plant, located in the north of Sweden. Active since 1915, one of its Kaplan units (turbine and generator), called U9, was replaced during the last decade. The main focus of the new U9 unit is to allow research on a real scale turbine rather than production of electric power [6]. The new turbine is somewhat smaller than the previous unit, and a sharp bent pipe was inserted into the old penstock when the new prototype was assembled. The prototype Kaplan runner has a diameter

of 1.55 m and an operational head of 55 m, with a maximum discharge capacity of 20 m^3/s and a power output of 10 MW. It is composed of a bent inlet pipe, a spiral casing, 18 stay vanes, 20 guide vanes, 6 runner blades and an elbowed draft tube. A 1:3.1 scale model of the same geometry was built for scientific studies, and a detailed measurement database is available.

The U9 Kaplan turbine presents a unique opportunity to validate numerical methods used to investigate the rising problems that hydro power faces, such as refurbishment problems (insertion of a sharp inlet bent at the inlet of the spiral casing for example) or transient phenomena due to load variations. The present work presents a study of this kind. It focuses on the impact that the bent inlet pipe has on the flow inside the turbine and analyzes the different available rotor-stator interfaces that can perform well for transient phenomena.

Chapter 2

CFD in Water Turbines

The use of computational fluid dynamics (CFD) to numerically investigate the flow of water through water turbines has become increasingly popular in the past three decades. Its flexibility, detailed flow description and cost effectiveness makes it an attractive complement to experimental investigations. It is now widely used in the design and refurbishment process, and to get a good understanding of the flow in the water turbine for different operating conditions. With a broad diversity of numerical models, CFD offers the possibility to approximate the flow features differently. The Reynolds decomposition is used on the Navier-Stokes equations to treat turbulent flow, see Appendix A. This creates an unbalance between the number of unknowns and the number of equations. Approximations therefore need to be made to solve the equations. For example, the first CFD analysis computed the 2D Euler equations to predict the behavior of the fluid, thus neglecting the effects of viscosity and turbulence [7]. Using a large number of approximations makes it possible to compute the problem faster but does not resolve all the details of the flow. If too large approximations are made, some of the important features of the flow will not be or will be wrongly predicted. With the development of computational software, the use of CFD and its accuracy has drastically increased. Nowadays, the effect of the fluid viscosity is included, and the effect of turbulence is modeled. The majority of the CFD software available uses the finite volume method to discretize the equations in time and space. The principle of the finite volume method is to divide the flow region into a large number of control volumes. These control volumes can be of different shapes, but they are often chosen to be hexahedral (six faces) to reduce the numerical errors and convergence problems. The totality of these control volumes is called the computational grid, or mesh. The viscous fluid flow equations, including a turbulence model, are then solved, and the different flow properties are computed at the center of each control volume.

2.1 The OpenFOAM CFD Tool

Predicting the flow in water turbines requires a great deal of computational resources. Running a simulation on only one CPU, when possible, takes a very long time for most cases. The computational speed can be increased however by running in parallel, computing different parts of the problem on different CPUs. The memory requirements for solving the equations on the discretized region are thus also distributed between the different CPUs. When proprietary software is used, parallel simulations require many licenses, which tend to be costly.

The present work used the relatively new OpenFOAM CFD tool. The OpenFOAM CFD solver was released as Open Source software in the end of 2004. It is a C++ object-oriented library for numerical simulations of partial differential equations [8]. Because of the OpenSource distribution under the GPL license, it can be used at no cost. The OpenSource concept also makes it possible to have full insight into the code, which is necessary for scientific studies and impossible with proprietary codes. The OpenFOAM community is growing every year and contributes to the development of this software. Previous studies show that the OpenFOAM CFD tool is as accurate as proprietary codes for many applications [9, 10, 11]. Since it is still a rather new CFD tool however, there is a need to develop and validate some features.

The present work is part of an international collaboration with the OpenFOAM turbomachinery Working Group, which aims to develop, extend and validate OpenFOAM for turbomachinery applications [12]. Most of the present work was shared to the OpenFOAM community through tutorials and test cases to create guidelines and help new OpenFOAM users.

2.2 The Boundary Condition Challenge

To numerically simulate the flow in a domain, it is necessary to specify the conditions at the boundaries of the flow region, such as the inlet, the walls and the outlet. The flow features predicted by the equations that govern the flow will largely depend on the quality of the boundary conditions. If the boundary conditions are not correct, the prediction of the flow will be less accurate, or incorrect. In a draft tube, the adverse pressure gradient generated below the runner is notorious to be very difficult to predict numerically [13]. To understand the impact of boundary conditions on the flow in the draft tube, international workshops were organized and numerical results using different boundary conditions were presented. The GAMM Francis runner was used as a test case in the *1989 GAMM Workshop on 3D Computation of Incompressible Internal Flows* [14]. The Hölleforsen Kaplan runner was used in three *Turbine-99* international workshops aiming to determine the state-of-the-art simulation of the flow in an elbowed draft tube [15, 16, 17, 18]. The GAMM workshop showed that, although the different numerical results concurred with the experiments, a large majority failed to catch an important unsteadiness behavior of the flow. The Turbine-99 workshops showed that it is very important to take into account the radial velocity at the inlet of a draft tube to get a good prediction of the flow in the draft tube. However, the flow in the draft tube is the result of the swirling flow that is

generated by the runner and the adverse pressure gradient created by the cone of the draft tube, followed by the sharp bend. To get accurate results, the interaction between the runner and the draft tube needs to be included in the simulation. For example, Nilsson and Davidson [10] showed that secondary flow between the runner and the shroud and hub plays an important role in the flow in the the draft tube.

More and more simulations tend to couple the different parts of the hydro turbine, to include the interaction of its different components in the simulation [19], but coupling different components together brings in turn a new boundary condition issue. The different parts of the computational domain are often meshed separately to ease the process and create better quality meshes. This often creates a non-conformal mesh, and a new boundary condition needs to be created to couple the different non-conformal parts together. The General Grid Interface (GGI) was implemented in OpenFOAM by Beaudoin and Jasak [20], using weighted interpolation to evaluate and transmit flow values across a pair of conformal or non-conformal coupled patches. The present work helped in the validation of this boundary condition [21].

More and more numerical work now includes the main components of the turbine. The spiral casing, stay and guide vanes, runner and draft tube are included in the simulation to better understand the interaction between those components and get a more accurate prediction of the flow. Common practice for such simulations is to set a plug flow inlet boundary condition at the inlet of the spiral casing. However, this is often not the case in reality. The penstock upstream is sometimes elbowed with a sharp angle close to the inlet of the spiral casing. In such a case, a plug flow at the inlet of the spiral casing is not realistic [22].

Thus, handling boundary conditions is crucial to obtaining accurate numerical results. It plays a very important role in the numerical results and is often the reason for a diverging simulation or an incorrect prediction of the flow features.

2.3 Rotor-Stator Interaction

When rotating and stationary parts are coupled together, high pressure fluctuations, vibration and unsteadiness occur. Dring *et al.* [23] demonstrated that, for turbomachinery applications, the two major sources of unsteadiness are potential and blade/wake interaction. To numerically predict accurately the unsteadiness, a rotor-stator interaction approach must be used. The three most common approaches for turbomachinery applications are given below.

2.3.1 The *Mixing Plane* Approach

Also called the *stage* approach in proprietary software, this approach circumferentially averages the flow through the interface. Doing so, it is thus sufficient to include only one blade in each stage and assume that the flow is periodic for the other blades in the same stage. It is a very common approach, as it reduces the computational domain and speeds up the simulation. With this approach, the flow through the different parts of the turbomachine can be simulated. However, tangential variations of the flow such as the wakes are not transported through the interface due to the circumferential average, see

Fig. 2.1(a). This is thus a simple approach and, although it gives an overall understanding of the flow, it does not correctly predict the rotor-stator interaction. The *mixing plane* is the latest addition to the OpenFOAM simulation toolbox and was mainly developed by Martin Beaudoin [24, 25].

2.3.2 The *Frozen Rotor* Approach

In the *frozen rotor* approach, the complete runner is mostly included but its position is frozen and the rotation is accounted for by the source terms. The rotating flow field is solved in a rotating frame of reference, and the Coriolis force is accounted for by the source term while the stationary flow is solved in a fixed frame of reference [21]. It enables the disturbance to be transported from one interface into the other, but in the wrong way, which can lead to unrealistic overestimation of the effect of the disturbance, as shown in Fig. 2.1(b). It is a steady-state approach, and the Reynolds Average Navier Stokes equations are solved. Thus, it does not resolve the unsteadiness of the wakes in time, and the results of this approach resemble a snapshot in time of the flow.

This is nevertheless a computationally fast method that gives a general overview of the flow [21]. It is very common to use this method at design phase for water turbine, where the general behavior of the flow is needed rather than the runner wake features in the draft tube cone.

2.3.3 The Unsteady Sliding Grid Approach

This rotor-stator approach solves the Unsteady Reynolds Averaged Navier-Stokes equations. The time dimension is added to the Navier-Stokes equations, and the unsteadiness of the flow is resolved. The physical motion of the mesh is physically addressed, and the rotor part of the mesh rotates at each time step. In this approach, the disturbances are properly transported from one interface into the other, see Fig. 2.1(d). It is a better approach, more realistic, but obviously computationally heavier to simulate than the *frozen rotor* approach.
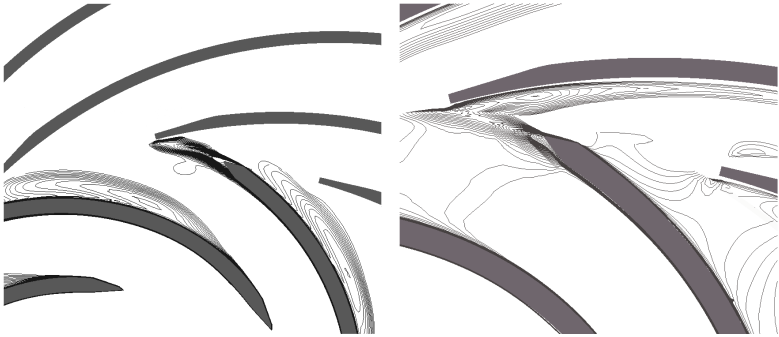
(a) Wake produced by the *mixing plane* approach

(b) Wake produced by the *frozen rotor* approach
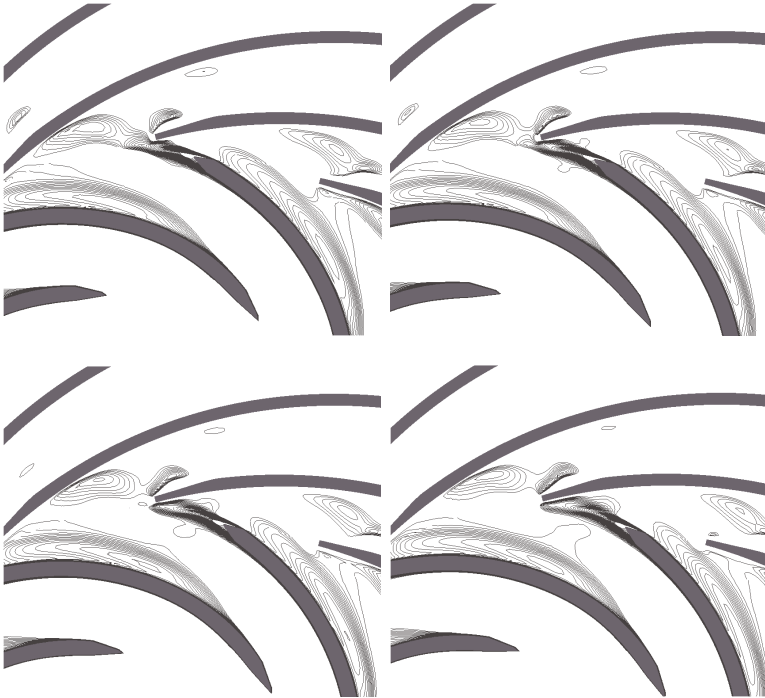
(d) Wake produced by the *sliding grid approach*

Figure 2.1: Overview of the rotor-stator interaction across the three major types of interface

2.4   Turbulence Modeling

The turbulence model used to solve the flow equations is very important for the accuracy of the results. Basic models such as the k-ε model allow a more stable computation but do not accurately predict all the turbulence. Depending on the geometry of the domain and on the flow behavior inside this domain, some turbulence models are more suitable than others. In a draft tube, Gyllenram [13] showed that a limit of the modeled scales can be used to predict the turbulent flow features with better accuracy. With this approach, more scales are resolved in time and space. Because it is time-consuming and expensive to numerically resolve all scales of motion in the flow, different approaches to turbulence modeling can be chosen. Figure 2.2 shows a qualitative classification of the main approaches to handling the turbulence.
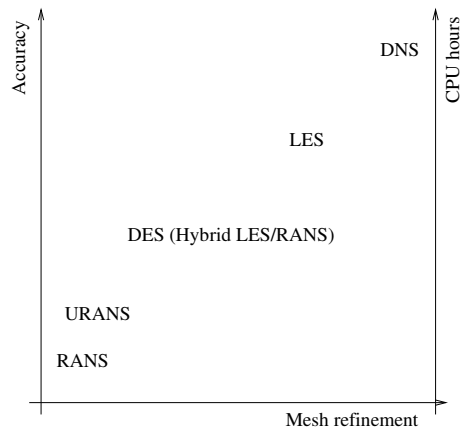
Figure 2.2:   Qualitative classification of the main approaches to solving and modeling the turbulence

The fastest and least accurate methods are the steady RANS (Reynolds Average Navier Stokes) methods. Because they are based on solving the time-averaged Navier-Stokes equations, the unsteadiness of the flow will not be solved. The turbulence model will then have to predict all the unsteady flow features. Thus the turbulence model needs to be advanced. However, steady RANS simulations do not require a long computational time, and the prediction of the overall flow is reasonably good. For unsteady RANS, part of the turbulence is resolved with the physical motion of the grid, and part is modeled. The URANS method was shown to accurately predict the unsteadiness [11]. However, it takes a longer time to compute, as another dimension (time) is added. For both approaches, two or more equations are needed to model the turbulence.

To get more detailed information about the unsteady motions of the flow, Large Eddy Simulation (LES), Hybrid LES/URANS (also called Detached Eddy Simulation) and Direct Numerical Simulation (DNS) methods are used. In those more advanced models, the small-scale turbulence is modeled and the large turbulence is resolved. However, it requires a much finer grid resolution, and a great deal of computing time. Predicting the

flow in the whole of the water turbine would require too much time. For water turbines, steady RANS and unsteady RANS methods are the two most common methods used to investigate the whole system, with two-equation eddy-viscosity turbulence models used to model the turbulence.

An extensive comparison of the turbulence models available in OpenFOAM was made by Moradnia [26]. The focus of Moradnia's study was particularly on high and low Reynolds number, two-equation eddy-viscosity turbulence models, as well as Reynolds Stress Transport turbulence models. The outcome of Moradnia's study was that four high Reynolds turbulence models were better at predicting the flow, while maintaining numerical stability. Those are the $k - \varepsilon$ [27], realizable $k - \varepsilon$ [28], RNG $k - \varepsilon$ [29] and the $k - \omega$ SST [30] turbulence models. As a follow-up, those four turbulence models are used in the present work.

Chapter 3

Scope of the Present Work

The main goal of the present work is to accurately predict the 3D unsteady incompressible flow in the U9 Kaplan water turbine model, from the upstream tank to the outlet of the draft tube. Little work has been done in the field of hydro power on unsteady simulations in such a large computational domain. Ruprecht *et al.* [31] presented early work on the unsteadiness of the flow in a Francis turbine, Labrecque *et al.* [32] studied the interactions between the different components of a Francis turbine and Li *et al.* [33] focused on the transients phenomena in a Francis turbine. To this date, most of the work focused on 3D unsteady flow has been done for Francis turbines. Even less work can be found on 3D transient calculation including the whole geometry of a Kaplan turbine. Liu *et al.* [34] is one of few such studies in Kaplan turbines.

To gain experience and knowledge for accurate prediction of the flow in the U9 model, the rotor-stator approaches, boundary conditions and numerical methods used in the present work need to be validated against detailed measurements. The present work uses three different turbomachinery test cases for validation, the ERCOFTAC Centrifugal Pump, the Timisoara Swirl Generator and the U9 Kaplan turbine model.

3.1 The ERCOFTAC Centrifugal Pump Test Case

The ERCOFTAC Centrifugal Pump (ECP) test case was presented by Combès [35] at the Turbomachinery Flow Prediction ERCOFTAC Workshop in 1999. The pump consists of a 420 mm diameter unshrouded centrifugal impeller and a 644 mm diameter radial vaned diffuser, see Fig. 3.1. Detailed velocity and pressure measurements were made in the radial gap between the impeller and the diffuser by Ubaldi *et al.* [36]. The 2D model of the ECP test case served as a validation test case for the General Grid Interface Interface in Paper I and for the *frozen rotor* and *sliding grid* rotor-stator approaches. This case study was released and shared with the community to guide new OpenFOAM users in how to get accurate results efficiently using those features. Further studies of 3D steady and unsteady numerical simulations are presented in paper IV. The unsteady sliding grid approach was concluded to be the best rotor-stator approach to use in the simulation of the Kaplan turbine model.
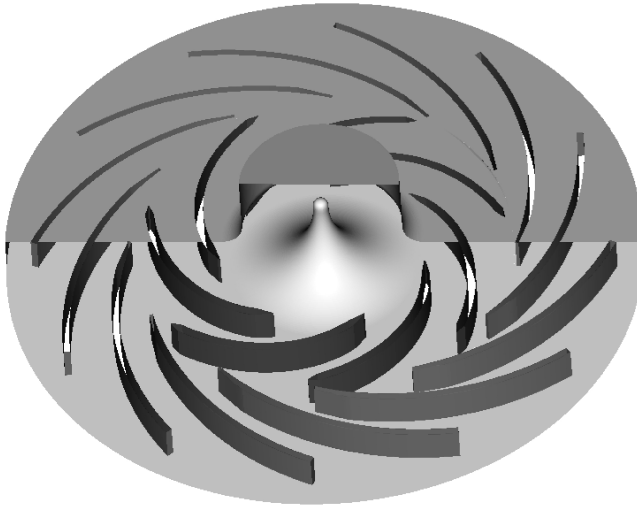
Figure 3.1:   Geometry of the ERCOFTAC Centrifugal Pump

3.2   The Timisoara Swirl Generator Test Case

The Timisoara Swirl Generator (TSG) test case [37] has a geometry with parts similar to those in a water turbine, i.e. guide vanes, runner and draft tube. The swirling flow apparatus consists of four leaned strouts, 13 guide vanes, a free runner with 10 blades and a convergent-divergent draft tube, see Fig. 3.2. The test rig was designed at Politehnica University of Timisoara, Romania, to experimentally investigate the unsteady helical vortex rope that forms at part discharge below the runner [38]. It is a very good case for investigating the impact of the boundary conditions and of the turbulence model on the prediction of the unsteady flow features. Velocity and pressure measurements were performed by Bosioc *et al.* [37] below the runner, at three different windows in the draft tube. A CFD calculation using the unsteady sliding grid approach is validated against the measurement database in Paper III. The TSG test case was presented to the OpenFOAM community as yet another case study for unsteady simulations of rotor-stator interaction. The unsteady sliding grid approach was concluded to be the best rotor-stator approach to use in the simulation of the Kaplan turbine model.

Figure 3.2:   Geometry of the Timisoara Swirl Generator

3.3 The U9 Kaplan Turbine Model

The 1:3.1 scale model of the U9 Kaplan turbine is located at Vattenfall Research and Development in Älvkarleby, Sweden. Velocity and pressure measurements were performed by Mulu *et al.* [39, 40, 41] and Jonsson *et al.* [42, 43], respectively. The U9 Kaplan turbine model is composed of 6 runner blades, 20 guide vanes and 18 stay vanes, and has a runner diameter of 0.5m. Paper II compares steady results of individual parts of the model with the experimental results. Paper V presents 3D unsteady simulations of the U9 Kaplan turbine model, from the high pressure tank to the outlet of the draft tube, see Fig. 3.3. The results demonstrate a strong impact of the bent intake pipe on the flow at the spiral casing inlet, which suggests that the commonly used plug flow spiral casing inlet condition is inappropriate. The results are validated against the velocity measurement database, showing a good similarity up to the runner. It is argued that the lack of leakage flow is one reason for the differences in the draft tube.
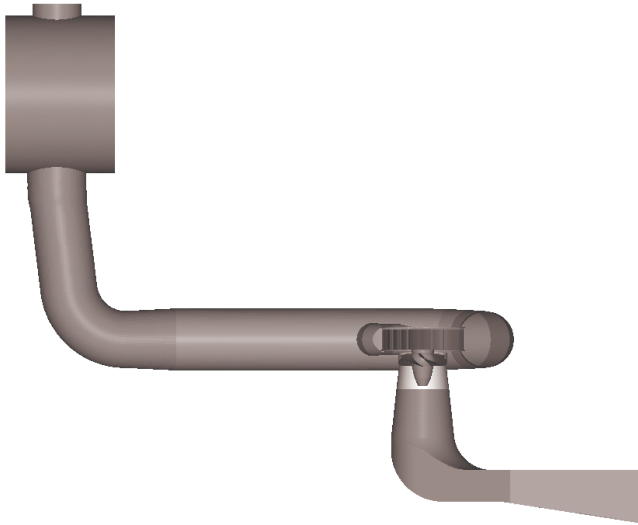
Figure 3.3: Geometry of the U9 Kaplan turbine model

Chapter 4

Conclusions and Future Work

4.1   Conclusions

The present work validates methodologies for accurate numerical predictions of the incompressible flow of water in the U9 Kaplan turbine model. At the beginning of the present work, the experimental database for the U9 Kaplan turbine model was not available. Two well-documented, and less computationally heavy test cases were thus used to validate the results, the ERCOFTAC Centrifugal Pump (ECP) and the Timisoara Swirl Generator (TSG). All cases include rotor-stator interaction and can be used to evaluate different rotor-stator interface approaches.

The present work investigate two rotor-stator interface approaches, the steady-state frozen rotor approach and the unsteady sliding grid approach. The General Grid Interface (GGI) is used to couple the rotor and stator interfaces in both cases. The results obtained with frozen rotor approach in the ECP test case show that the steady-state frozen rotor approach yields unphysical advection of the impeller wakes. Such a steady-state approach should thus be used as an initial guess for unsteady simulations with the sliding grid approach.

The unsteady sliding grid approach was then validated in both the ECP and the TSG test cases. The GGI was used to couple the rotating and stationary domains at each time step. The results for the ECP test case show good agreement with the experimental ones, and most of the unsteadiness of the flow is predicted. With the unsteady sliding grid approach, the numerical results show that the impeller wakes are advected to the exit of the diffuser. Four turbulence models are used to performed the unsteady simulations, the k-ε, realizable k-ε, RNG k-ε and k-ω SST. The results show that all turbulence model show a qualitative good agreement with the experimental results. The turbulent models yield slightly different results, but predict the flow unsteadiness to the same level of accuracy. The differences between the numerical and experimental results can be explained by the geometrical simplifications in the computational domain. The results for the TSG test case show very good agreement with the numerical ones, and the wakes are also visible below the runner. The frequency and amplitude of the predicted vortex rope are in good agreement with the experimental ones, and its axial pulsation is correctly predicted.

The knowledge gathered through those two test cases was then used to simulate the unsteady flow in the U9 Kaplan turbine model, from the high pressure tank up to the spiral casing, the runner, and down to the draft tube. The computational domain consists of approximately 15 millions cells, and the simulations are run in parallel on 32 cores. Four turbulence models are used to perform the calculations, the k-ε, realizable k-ε, RNG k-ε and k-ω SST. The numerical results are then compared to the experimental data, at the inlet of the spiral casing just after the bent inlet pipe, in the spiral casing at two different windows and in the draft tube cone below the runner. At the inlet of the spiral casing the numerical and experimental data are in good agreement and show that the disturbance created by the bent inlet pipe is transported to the inlet of the spiral casing. The strong impact of the bent inlet pipe on the flow at the inlet of the spiral casing suggests that the commonly used plug flow spiral casing inlet boundary condition is inappropriate for accurate simulation of the flow in the Kaplan turbine model. In the spiral casing, the numerical results are also in good agreement with the experimental data. The k-ω SST turbulence model seems to perform slightly better than the other turbulence models studied and show the best agreement with the measurements. Below the runner, the general behavior of the flow is captured and the calculated velocity profiles are of the same magnitude than the measured ones. However, the simulations fail to accurately predict the experimental velocity profiles. The four different turbulence models do not seem to improve the flow prediction in the draft tube. This in turn reinforces that the differences between the numerical and experimental results come from the lack of runner blade tip clearances.

The thesis shows the importance of specifying inlet boundary conditions at locations where the flow is known. Also the interaction between stationary and rotating part of the turbine is of importance. The quality of the rotor-stator coupling used in the numerical simulations determines the numerical accuracy of the rotor-stator interactions.

The present work is done using the OpenFOAM Open Source Software. The code is chosen to facilitate an OpenSource distribution of the developments, to be shared in the scientific community, and to be directly useful in industry. The OpenSource concepts also makes it possible to have full insight into the code, which is necessary for scientific studies and impossible with proprietary codes. The present work was part of an international collaboration, focused on the development of OpenFOAM for turbomachinery applications, and has significantly contributed to the validation of new implementations. The present work has contributed in sharing these test cases were shared with the OpenFOAM community, as a mean to create guidelines for future users.

4.2   Future Work

This thesis presents work that aim at fully predicting the unsteady flow in the U9 Kaplan turbine, using the OpenFOAM OpenSource software. With the help of the present work, it is now possible to achieve accurate simulations of the flow in turbomachinery applications. But to ensure the accuracy of numerical simulations and further increase the trust in the CFD methods, it is important to continue the validation work.

An important flow feature in rotating machines is the leakage flow that is created

by the runner blade tip clearances. In the present work, the geometry of the different test cases is simplified, and the tip clearances are not included. The lack of tip clearance flow is argued to be one of the reasons for the differences between the numerical and experimental results in the ECP test case, and in the U9 Kaplan turbine model. The impact of such leakage flow should improve the accuracy of the numerical results in the radial gap for the ERCOFTAC Centrifugal Pump, and in the draft tube cone for the U9 Kaplan turbine model.

The present work shows the importance that the bent inlet pipe has on the flow at the inlet of the spiral casing, in the U9 Kaplan turbine model. It creates a non-uniform flow, and two counter vortices enters the spiral casing. However, the impact of the bent inlet pipe on the global characteristics of the U9 Kaplan turbine was not investigated. Such investigations should help to understand the impact of the bent inlet pipe on the turbine. To accurately predict the recirculation that occurs after the bent, more advanced turbulence models, such as hybrid models, could be used.

The present work is a part of a project aimed at investigating the flow characteristics in the U9 Kaplan turbine model. An extensive measurement database is available for three operating loads. The present work presents numerical simulations performed at Best Efficiency Point. CFD simulations should thus be made for the two other operating load, at part and high load. The numerical results can be validated against the experimental database, for the velocity and the pressure.

Chapter 5

Summary of Papers

Paper I

The ERCOFTAC Centrifugal Pump OpenFOAM Case-Study

Paper I presents and validates the two most widely used methods for predicting rotor-stator interaction flow features, the steady-state *frozen rotor* and the unsteady *sliding grid* methods. The frozen rotor approach is a steady-state approach that uses multiple frames of reference to solve the Reynolds Average Navier Stokes equations. The Coriolis force is accounted for in the source term in the rotating region. The unsteady sliding grid approach includes the time dimension in the Unsteady Reynolds Average Navier Stokes equations and the rotating part of the mesh rotates at each time step.

The OpenFOAM CFD tool was used to simulate the 2D flow in the ERCOFTAC centrifugal pump test case. The ERCOFTAC centrifugal pump was presented by Combès [35] as a test case for the Turbomachinery Flow Prediction ERCOFTAC Workshop in 1999. Detailed velocity and pressure measurements were performed by Ubaldi *et al.* [36] in the radial gap between the impeller and diffuser vanes. To couple the interfaces in the two rotor-stator interaction methods, a new coupled boundary condition, the General Grid Interface (GGI), was implemented by Beaudoin and Jasak [20] in OpenFOAM, and Paper I presents a test case for its validation.

Paper I shows that the steady-state frozen rotor method gives a good overview of the flow but does not predict the advection of the runner wakes properly, which on the other hand is done well by the sliding grid method. Although both methods are validated in the paper, Paper I concludes that, to make accurate simulations of the unsteady flow in turbomachinery applications, the unsteady sliding grid approach should be preferred to the frozen rotor approach. To capture even more unsteadiness of the flow, the authors suggest performing 3D unsteady calculations.

Paper II

Comparison of Numerical and Experimental Results of the Flow in the U9 Kaplan Turbine Model

Paper II presents steady simulations of two individual parts of the U9 Kaplan turbine, the spiral casing and the draft tube. The simulations were made with OpenFOAM and the standard $k - \varepsilon$ turbulence model. The numerical results are validated against detailed velocity measurements realized by Mulu and Cervantes [39, 40, 43] at the inlet of, and inside, the spiral casing, and in the draft tube. The simulations were done for one working load, at the best efficiency point. The measured velocity profiles are compared with the numerical results at the inlet of the spiral casing and at two angular positions in the spiral casing. In the draft tube cone, the numerical results are compared with the experimental ones for three axial positions.

The focus in Paper II is on the boundary condition assumption. Common practice for the definition of the spiral casing inlet boundary condition is a plug flow at the inlet of the spiral casing. In Paper II, the spiral casing is extended upstream until the high pressure tank to include the effect of the sharp bend that is mounted close to the inlet of the spiral casing. In the high pressure tank, a plug flow inlet boundary condition can be set for the numerical simulation. In the draft tube, the axial and tangential velocity components measured with LDA below the runner are used as inlet boundary conditions. The radial velocity is set to zero.

The numerical results in the spiral casing are in good agreement with the measurements, but it is suggested that there is room for improvement by changing the turbulence model. In the draft tube, however, the numerical results fail to accurately predict the flow at the center of the draft tube cone, although the simulation captures the general behavior of the flow. Paper II concludes that, for the draft tube, the inlet boundary condition is not ideal, and that the radial velocity component should be included in the inlet boundary condition. Ultimately, Paper II recommends that, to capture the flow in the draft tube, the unsteady interaction between the runner and the draft tube should be included.

Paper III

Unsteady Simulations of the Flow in a Swirl Generator, Using OpenFOAM

Paper III numerically validates the results of the flow in the swirl generator test rig located in Politehnica University of Timisoara, Romania. The test rig is a simplified turbine that aims at studying the precessing vortex rope that is created after a runner when operated at partial discharge. The different components of the swirl generator are very similar to those of a water turbine. Detailed pressure and velocity measurements were made by Bosioc *et al.* [37].

The swirl generator consists of 4 leaned strouts, 13 guide vanes, a free runner with 10 blades and a convergent-divergent draft tube. The OpenFOAM CFD tool is used to compute the flow through the whole domain. The steady-state *frozen rotor* approach is used to get an accurate initial guess, and then the unsteady *sliding grid* method is used to compute the unsteady flow between the runner and the stationary parts. The different components are coupled using the General Grid Interface validated in Paper I, and the numerical results are compared with the experimental results. The turbulence is modeled using the standard $k - \varepsilon$ turbulence model.

The comparison shows that the flow predicted by OpenFOAM is in good agreement with the measured flow, and that the unsteady flow features are accurately predicted. An angular time step optimization was performed, and Paper III concluded that, to accurately predict the unsteadiness of the flow, the angular rotation can be optimized to about $1°$ per time step. The Timisoara swirl generator case study was released to the OpenFOAM community as a case study for unsteady simulation in turbomachinery applications. Paper III demonstrates and validates the accuracy of the method, despite the simple turbulence model.

Paper IV

Numerical Investigations of Unsteady Flow in a Centrifugal Pump with a Vaned Diffuser

Paper IV is a continuation of Paper I. Based on the experience and conclusions of Paper I, the 3D steady and unsteady simulations of the ERCOFTAC centrifugal pump are presented. The steady-state frozen rotor and unsteady sliding grid rotor-stator methods were used to simulate the flow through the pump. The General Grid Interface was used to couple the interfaces. The numerical results are then compared against the detailed measurement database available in the radial gap, performed by Ubaldi *et al.* [36].

First, the frozen rotor and sliding grid approaches are analyzed using a standard $k - \varepsilon$ model. The steady-state frozen rotor produces a good general overview of the flow but fails to accurately predict the wake advection in the diffuser vanes. The flow computed using the unsteady sliding grid approach yields good agreement with the measurements and accurately predicts the advection of the wakes through the diffuser vanes. Paper IV presents an analysis of four two-equations eddy-viscosity turbulence models, $k - \varepsilon$ [27], realizable $k - \varepsilon$ [28], RNG $k - \varepsilon$ [29] and $k - \omega$ SST [30]. The turbulence models yield slightly different results but predict the flow unsteadiness at the same level of accuracy. Paper IV suggests that the discrepancies between numerical and experimental results are due to the tip clearance between the impeller blades and the shroud,which was not included in the simulation.

Paper V

Towards a Full Prediction of the 3D Unsteady Flow in the U9 Kaplan Turbine Model

Paper V presents the 3D unsteady flow predictions in the U9 Kaplan turbine model, including the high pressure tank, inlet curved pipe, spiral casing, stay and guide vanes, and runner down to the draft tube. It is a summing up of all the previous experiences and uses the numerical methods validated in the previous papers. The unsteady sliding grid approach is used to compute the rotor-stator interaction. The computational domain consists of about 15 million cells, and the simulation is run on 32 cores in a cluster. The OpenFOAM CFD tool is used to compute the flow, and the numerical results are compared with detailed velocity measurements performed by Mulu [39, 40, 43].

First, the standard $k - \varepsilon$ turbulence model is used to compute the flow. At the inlet of and in the spiral casing, the numerical results show good agreement with the experiments, although the recirculation region at the bend seems to be over-predicted. The predicted flow below the runner is however less accurate and, although the general behavior of the flow is captured, large discrepancies between numerical results and measurements are observed. Below the runner cone, the computed recirculation region is largely over-predicted, and the flow separates too early at the wall. Second, Paper V presents a comparison between four two-equation eddy-viscosity turbulence models, $k - \varepsilon$ [27], realizable $k - \varepsilon$ [28], RNG $k - \varepsilon$ [29] and $k - \omega$ SST [30]. Upstream of the runner, the flow computed with the $k - \omega$ SST turbulence model seems to be slightly better predicted, while the $k - \varepsilon$ turbulence models compute almost the same flow. Below the runner, no major difference between the four turbulence model is observed. Paper V thus suggests that the inaccuracy of the computed flow does not come from the performance of the turbulence models but rather from a lack of geometrical detail in the computational domain, such as the runner blade clearances. It is argued that this secondary flow should prevent the flow from separating at the draft tube cone and reduce the recirculation area below the runner cone.

Bibliography

[1] International Energy Agency. World energy outlook, 2009. http://www.iea.org/.

[2] B. Lapillone. World enery use in 2010: Over 5% growth, 2011. http://www.enerdata.net/enerdatauk.

[3] Energi Myndigheten, 2010. http://energimyndigheten.se.

[4] D. Böhme, W. Dürrschmidt, and M. Van Mark, editors. *Renewable Energy Sources in Figures - National and International Development.* Federal Ministry for the Environment, Nature Conservation and Nuclear Safety (BMU), Public Relations Division, Germany, 2009. http://www.erneuerbare-energien.de.

[5] World Energy Council, editor. *Survey of Energy Resources.* Tech. rep., WEC, 2010.

[6] M.J. Cervantes, I. Jansson, A. Jourak, S. Glavatskikh, and J.O. Aidanpää. Porjus U9, a Full-scale Hydropower Research Facility. *24ᵗʰ IAHR Symposium on Hydraulic Machinery and Systems - Foz Do Iguassu*, 2008. ISBN: 978-85-60858-13-1.

[7] H. Keck and M. Sick. Thirty Years of Numerical Flow Simulation in Hydraulic Turbomachines. *Acta Mechanica*, 201(1-4):211–229, 2008. DOI: 10.1007/s00707-008-0060-4.

[8] H.G. Weller, G. Tabor, H. Jasak, and C. Fureby. A Tensorial Approach to Computational Continuum Mechanics using Object-Oriented Techniques. *Computers in Physics*, 12(6):620–631, 1998.

[9] O. Petit, H. Nilsson, T. Vu, O. Manole, and S. Leonsson. The Flow in the U9 Kaplan Turbine - Preliminary and Planned Simulations Using CFX and OpenFOAM. *24ᵗʰ Symposium on Hydraulic Machinery and Systems*, 2008.

[10] H. Nilsson. Evaluation of OpenFOAM for CFD of Turbulent Flow in Water Turbines. *23ᵗʰ IAHR Symposium on Hydraulic Machinery and Systems*, 2006.

[11] S. Muntean, H. Nilsson, and R.F. Susan-Resiga. 3D Numerical Analysis of the Unsteady Turbulent Swirling Flow in a Conical Diffuser Using Fluent and OpenFOAM. *3ʳᵈ IAHR International Meeting of the Workgroup on Cavitation and Dynamic Problems in Hydraulic Machinery and Systems - Brno*, C4:155–164, 2009.

[12] H. Nilsson, M. Page, M. Beaudoin, and H. Jasak. The OpenFOAM Turbomachinery Working Group, and Conclusions from the Turbomachinery Session of the Third OpenFOAM Workshop. *3rd IAHR International Meeting of the Workgroup on Cavitation and Dynamic Problems in Hydraulic Machinery and Systems - Brno*, 2009.

[13] W. Gyllenram. *Analytical and Numerical Studies of Internal Swirling Flows*. PhD thesis, Division of Fluid Dynamics, Chalmers University of Technology, 2008.

[14] G. Sottas and I.L. Ryhming. 3D Computations of Incompressible Internal Flows. *Proceedings of the GAMM Workshop*, 1993.

[15] B.R. Gebart, L.H. Gustavsson, and R.I. Karlsson. Proceedings of Turbine-99 - Workshop on Draft Tube Flow. Technical Report 2000:11, Luleå Tekniska Universitet, Strömningslära, 2000. ISSN: 1402-1536.

[16] T.F. Engström, L.H. Gustavsson, and R.I. Karlsson. 2nd IAHR/ERCOFTAC Workshop on Draft Tube Flow. *Proceedings of Turbine-99 II*, 2001.

[17] M. Cervantes, T.F. Engström, and L.H. Gustavsson. Proceedings of Turbine-99 III - 3rd IAHR/ERCOFTAC Workshop on Draft Tube Flow. Technical Report 2005:20, Luleå Tekniska Universitet, Strömningslära, 2005. ISSN: 1402-1528.

[18] M.J. Cervantes, L.H. Gustavsson, M. Page, and F. Engström. Turbine-99, a Summary. *23rd IAHR Symposium - Yokohoma*, 2006. ISBN: 4-8190-1809-4.

[19] G.D. Giocan, M.S. Iliescu, T.C. Vu, B. Nennemann, and F. Avellan. Experimental Study and Numerical Simulation of the FLINDT Draft Tube Rotating Vortex. *Journal of Fluids Engineering*, 129(2):146–158, 2004. DOI: 10.1115/1.2409332.

[20] M. Beaudoin and H. Jasak. Development of a Generalized Grid Interface for Turbomachinery Simulations with OpenFOAM. *Open Source CFD International Conference - Berlin*, 2008.

[21] O. Petit, M. Page, M. Beaudoin, and H. Nilsson. The ERCOFTAC Centrifugal Pump OpenFOAM Case-Study. *3rd IAHR International Meeting of the Workgroup on Cavitation and Dynamic Problems in Hydraulic Machinery and Systems - Brno*, 2009.

[22] B. Mulu and M. Cervantes. Effects of Inlet Boundary Conditions on Spiral Casing Simulation. *Scientific Bulletin of the "Politehnica" University of Timisoara Transactions on Mechanics*, Tom 52(66), Fascicola 6, 2007.

[23] R.P. Dring, H.D. Joslyn, L.W. Hardin, and J.H. Wagner. Turbine Rotor-Stator Interaction. *A.S.M.E Journal of Engineering for Power*, 104(4):729–742, 1982. DOI: 10.1115/1.3227339.

[24] M. Page, M. Beaudoin, and A.M. Giroux. Steady-State Capabilities for Hydroturbines with OpenFOAM. *25th Symposium on Hydraulic Machinery and Systems*, 12(1), 2010. DOI: 10.1088/1755-1315/12/1/012076.

[25] H. Jasak and M. Beaudoin. OpenFOAM Turbo Tools: from General Purpose CFD to Turbomachinery Simulations. *Proceedings of ASME-JSME-KSME Joint Fluids Engineering Conference*, 2011. Paper No. AJK2011-05015.

[26] P. Moradnia. CFD of Air Flow in Hydro Power Generators. Licentiate thesis, Division of Fluid Dynamics, Chalmers University of Technology, 2010.

[27] F.S. Lien and M.A. Leschziner. Computational Modeling of 3D Turbulent Flow in s-diffuser and Transition Ducts. 2nd *International Symposium of Engineering Turbulence Modeling and Experiments*, 2:217–228, 1993.

[28] V. Yakhot, S.A. Orszag, S. Thangam, T.B. Gatski, and C.G. Speziale. Development of Turbulence Models for Shear Flows by a Double Expansion Technique. *Physics of Fluids*, 4(7), 1992. DOI: 10.1063/1.858424.

[29] T.H. Shih, W. Liou, A. Shabbir, Z. Yang, and J. Zhu. A New $k - \varepsilon$ Eddy-Viscosity Model for High Reynolds Number Turbulent Flows. *Computers and Fluids*, 24(3):227–238, 1995. 10.1016/0045-7930(94)00032-T.

[30] F.R. Menter. Two-Equation Eddy-Viscosity Turbulence Models for Engineering Applications. *AIAA Journal*, 32(8):1598–1605, 1994. ISSN: 0001-1452.

[31] A. Ruprecht. Unsteady Flow Analysis in Hydraulic Turbomachinery. *Proceedings of the 20th IAHR Symposium on Hydraulic Machinery and Systems*, 2000.

[32] Y. Labrecque, M. Sabourin, and C. Deschênes. Numerical Simulation of a Complete Turbine and Interaction between Components. *Modeling, Testing and Monitoring for Hydro Powerplants*, 1996.

[33] J. Li, J. Yu, and Y. Wu. 3D Unsteady Turbulent Simulations of the Runaway Transients of the Francis Turbine. *Journal of Hydroelectric Engineering*, 2010. DOI: CNKI:SUN:SFXB.0.2008-06-029.

[34] S. Liu, Q. Chen, and Y. Wu. Unsteady Cavitating Turbulent Flow Simulation in a Kaplan Turbine. *Scientific Bulletin of the "Politehnica" University of Timisoara, Transactions on Mechanics*, Tom 52(66), Fascicola 6, 2007.

[35] J.F. Combes, P.F. Bert, and J.L Kueny. Numerical Investigation of the Rotor-Stator Interaction in a Centrifugal Pump Using a Finite Element Method. *A.S.M.E Fluids Engineering Division Summer Meeting*, 1997.

[36] M. Ubaldi, P. Zunino, G. Barigozzi, and A. Cattanei. An Experimental Investigation of Stator Induced Unsteadiness on Centrifugal Impeller Outflow. *Journal of Turbomachinery*, 118(1):41–54, 1996. DOI: 10.1115/1.2836604.

[37] A.I. Bosioc, C. Tanasa, S. Muntean, and R.F. Susan-Resiga. 2D LDV Measurements of Swirling Flow in a Simplified Draft Tube. *The 14th International Conference on Fluid Flow Technologies*, 2009.

[38] R.F. Susan-Resiga, S. Muntean, C. Tanasa, and A. Bosioc. Hydrodynamic Design and Analysis of a Swirling Flow Generator. *4th German-Romanian Workshop on Turbomachinery Hydrodynamics, GROWTH-4 - Germany*, 2008.

[39] B. Mulu and M. Cervantes. Experimental Investigation of a Kaplan model with LDA. *33rd IAHR Congress: Water Engineering for a Sustainable Environment*, 2009.

[40] B. Mulu and M. Cervantes. LDA Measurements in a Kaplan Spiral Casing Model. *13th International Symposium on Transport Phenomena and Dynamics of Rotating Machinery*, 2010.

[41] B. Mulu, P. Jonsson, and M. Cervantes. Experimental Investigation of a Kaplan Draft Tube - Part I: Best Efficiency Point. *Journal of Applied Energy*, 93:695–706, 2012. DOI: 10.1016/j.apenergy.2012.01.004.

[42] P. Jonsson, B. Mulu, and M. Cervantes. Experimental Investigation of a Kaplan Draft Tube - Part II: Off-Design Conditions. *Journal of Applied Energy*, 94(2):71–83, 2012. DOI: 10.1016/j.apenergy.2012.01.032.

[43] P. Jonsson and M. Cervantes. Time Resolved Pressure Measurements on a Kaplan Turbine Model. *33rd IAHR Congress: Water Engineering for a Sustainable Environment*, 2009.

[44] H. Jasak. Dynamic Mesh Handling in OpenFOAM. *47th AIAA Aerospace Sciences Meeting Including the New Horizons Forum and Aerospace Exposition*, 2008.

[45] H.K. Versteeg and Malalasekera W., editors. *An Introduction to Computational Fluid Dynamics: the Finite Volume Method*. Pearson Education Ltd, 2007. ISBN: 13:978-0-13-127498-3.

[46] O. Petit, A.I. Bosioc, H. Nilsson, S. Muntean, and R. Susan-Resiga. Unsteady Simulations of the Flow in a Swirl Generator, Using OpenFOAM. *International Journal of Fluid Machinery and Systems*, 4(1):199–208, 2008. DOI: 10.5293/IJFMS.2011.4.1.199.

Appendix A

Governing Equations

This appendix describes the governing equations for turbulent flow. Section A.1 presents the continuity and momentum equation used to describe the flow. Section A.2 presents the different turbulence models used in the present work.

A.1 Continuity and Momentum Equations

The equations that describe a fluid in motion are derived from the conservation of mass, momentum and energy. The governing equations were first described by the French mathematician Claude Louis Navier (1785-1836) and the English mathematician Sir George Gabriel Stokes (1819-1903).
From mass conservation, the continuity equation reads

$$\frac{\partial \rho}{\partial t} + \frac{\partial \rho u_i}{\partial x_i} = 0 \tag{A.1}$$

Using the assumption that water is incompressible, i.e. the density is space and time independent, the continuity equation can thus be simplified to

$$\frac{\partial u_i}{\partial x_i} = 0 \tag{A.2}$$

From the momentum equation stated by the Newton's second law, the Navier-Stokes equations are derived as

$$\frac{\partial u_i}{\partial t} + u_j \frac{\partial u_i}{\partial x_j} = -\frac{1}{\rho}\frac{\partial p}{\partial x_i} + \frac{\partial}{\partial x_j}\left(\nu\left(\frac{\partial u_i}{\partial x_j} + \frac{\partial u_j}{\partial x_i}\right)\right) \tag{A.3}$$

Using the incompressibility assumption and continuity equation Eq. A.2, the Navier-Stokes equations can be simplified to

$$\frac{\partial u_i}{\partial t} + u_j \frac{\partial u_i}{\partial x_j} = -\frac{1}{\rho}\frac{\partial p}{\partial x_i} + \nu\frac{\partial^2 u_i}{\partial x_j^2} \tag{A.4}$$

The left hand side represents the inertia of the fluid; the first term from the left represents the unsteadiness, and the second the convection. On the right hand side, the first term from the left represents the pressure gradient and the second is the viscosity term.

To treat turbulent flow, The Reynolds decomposition is used and the instantaneous variables are decomposed in time-averaged and fluctuating quantities as

$$
\begin{aligned}
u_i &= U_i + u_i' \\
p &= P + p'
\end{aligned}
\tag{A.5}
$$

Inserting Eq. A.5 into the Navier Stokes equations Eq. A.4, and time-averaging it yields the Unsteady Reynolds Averaged Navier-Stokes equations (URANS) for incompressible flow, i.e.

$$
\begin{aligned}
\frac{\partial U_i}{\partial x_i} &= 0 \\
\frac{\partial U_i}{\partial t} + \frac{\partial}{\partial x_j}(U_i U_j) &= -\frac{1}{\rho}\frac{\partial P}{\partial x_i} + \frac{\partial}{\partial x_j}\left(\nu\frac{\partial U_i}{\partial x_j} - \overline{u_i' u_j'}\right)
\end{aligned}
\tag{A.6}
$$

By time-averaging the Navier-Stokes equations, a new term appears, called the turbulent stress tensor (or Reynolds stress tensor)

$$
\tau_{ij} = \rho\overline{u_i' u_j'}
\tag{A.7}
$$

The Reynolds stress tensor represents the correlation between the fluctuating velocities. It is unknown and makes the system of equations unsolvable, as the number of unknowns is indeed larger than the number of equations. In order to solve the equations, the Reynolds stress tensor must be modeled.

A.2   Turbulence Modeling

Many different approaches have been developed over the years to model the Reynolds stress tensor. Accuracy and computational costs vary greatly depending on the model chosen. The most common models are two-equation models. In the present work, four of the two-equation models were chosen, the $k - \varepsilon$, RNG $k - \varepsilon$, realizable $k - \varepsilon$ and $k - \omega$ SST turbulence models. Two-equation turbulence models use the Boussinesq assumption to model the Reynolds stress tensor. The Boussinesq assumption relates the Reynolds stress tensor to the velocity gradients and turbulent viscosity as

$$
\overline{u_i' u_j'} = -\nu_t\left(\frac{\partial U_i}{\partial x_j} + \frac{\partial U_j}{\partial x_i}\right) + \frac{2}{3}\delta_{ijk} = -2\nu_t S_{ij} + \frac{2}{3}\delta_{ijk}
\tag{A.8}
$$

The last term is added to make the equation valid when it is contracted. This is a drastic simplification, but the 6 unknown turbulent stresses are now replaced with only one new unknown, the turbulent viscosity, ν_t.

A.2.1 The $k - \varepsilon$ Turbulence Model

Two quantities are usually used in an eddy-viscosity model to express the turbulent viscosity. In the $k - \varepsilon$ turbulence model, the turbulent kinetic energy, k $[m^2/s^2]$, and dissipation rate, ε $[m^2/s^3]$, are used [27]. The turbulent viscosity is then computed as

$$\nu_t = C_\mu \frac{k^2}{\varepsilon} \tag{A.9}$$

The equation for the turbulent kinetic energy, k, is derived from the Navier-Stokes equations. It is the sum of all normal Reynolds stresses, i.e.

$$k = \frac{1}{2}\left(\overline{u_1'^2} + \overline{u_2'^2} + \overline{u_3'^2}\right) \equiv \frac{1}{2}\overline{u_i'u_i'} \tag{A.10}$$

Taking the trace (i=j) and dividing by 2, the modeled equation for the turbulent kinetic energy yields

$$\frac{\partial k}{\partial t} + \frac{\partial U_j k}{\partial x_j} = \frac{\partial}{\partial x_j}\left(\left(\nu + \frac{\nu_t}{\sigma_k}\right)\frac{\partial k}{\partial x_j}\right) + P_k - \varepsilon \tag{A.11}$$

The Boussinesq assumption comes in the production term

$$P_k = -\frac{1}{\rho}\overline{u_i'u_j'}\frac{\partial \overline{v_i'}}{\partial x_j} = 2\nu_t S_{ij} S_{ij}$$
$$S_{ij} = \frac{1}{2}\left(\frac{\partial U_i}{\partial x_j} + \frac{\partial U_j}{\partial x_i}\right) \tag{A.12}$$

A similar expression can be derived for the dissipation term, ε, i.e.

$$\frac{\partial \varepsilon}{\partial t} + \frac{\partial \varepsilon U_j}{\partial x_j} = \frac{\partial}{\partial x_j}\left(\left(\nu + \frac{\nu_t}{\sigma_\varepsilon}\right)\frac{\partial \varepsilon}{\partial x_j}\right) + C_{\varepsilon 1}\frac{\varepsilon}{k}P_k - C_{\varepsilon 2}\frac{\varepsilon^2}{k} \tag{A.13}$$

The closure coefficients are $C_{\varepsilon 1} = 1.44$, $C_{\varepsilon 2} = 1.92$, $C_\mu = 0.09$, $\sigma_k = 1.0$ and $\sigma_\varepsilon = 1.3$.

A.2.2 The Realizable $k - \varepsilon$ Turbulence Model

The two-equation eddy-viscosity realizable $k - \varepsilon$ model was developed by Shih *et al.* [29]. This model was developed from the $k - \varepsilon$ turbulence model. The equation for the turbulent kinetic energy, k, is the same as for the standard $k - \varepsilon$ turbulence model, see Eq. A.11, but a new condition is added for the dissipation transport equation. All normal stresses should stay positive, $\overline{u_i'^2} \geq 0$ for all i. It is called the realizability condition. The new equation for the dissipation is written as

$$\frac{\partial \varepsilon}{\partial t} + \frac{\partial \varepsilon U_j}{\partial x_j} = \frac{\partial}{\partial x_j}\left[\left(\nu + \frac{\nu_t}{\sigma_\varepsilon}\right)\frac{\partial \varepsilon}{\partial x_j}\right] + C_{\varepsilon 1}S\varepsilon - C_{\varepsilon 2}\frac{\varepsilon^2}{k + \sqrt{\nu\varepsilon}} \tag{A.14}$$

where

$$C_{\varepsilon 1} = \max\left[0.43, \frac{\eta}{\eta + 5}\right]$$

$$\eta = S\frac{k}{\varepsilon}$$

$$S = \sqrt{2S_{ij}S_{ij}}$$

(A.15)

The Reynolds stress tensor is modeled in the same way as in the standard $k - \varepsilon$, but the realizability constraint is added

$$\nu_t = C_\mu \frac{k^2}{\varepsilon}$$

(A.16)

$$C_\mu = \frac{1}{A_0 + A_s \frac{kU^*}{\varepsilon}}$$

$$U^* \equiv \sqrt{S_{ij}S_{ij} + \tilde{\Omega}_{ij}\tilde{\Omega}_{ij}}$$

$$\tilde{\Omega}_{ij} = \Omega_{ij} - 2\varepsilon_{ijk}\omega_k$$

$$\Omega_{ij} = \overline{\Omega_{ij}} - \varepsilon_{ijk}\omega_k$$

(A.17)

$\overline{\Omega_{ij}}$ is the mean rate-of-rotation tensor viewed in a rotating reference frame with the angular velocity ω_k. The closure coefficients are $A_0 = 4.04$, $A_s = \sqrt{6}\cos\phi$, $C_{\varepsilon 2} = 1.9$, $\sigma_k = 1.0$, and $\sigma_\varepsilon = 1.2$.

A.2.3 The RNG $k - \varepsilon$ Turbulence Model

The two-equation eddy-viscosity RNG $k - \varepsilon$ turbulence model is a variant of the standard $k - \varepsilon$ turbulence model. It was developed by Yakhot *et al.* [28] and is based on the "Re-Normalization Groups method". The Navier-Stokes equations are renormalized to account for the effects of smaller scales of motion. The kinetic energy transport equation in this model is similar to the one for the standard $k - \varepsilon$ turbulence model, see Eq. A.11. The equation for the dissipation reads

$$\frac{\partial \varepsilon}{\partial t} + \frac{\partial \varepsilon U_i}{\partial x_i} = \frac{\partial}{\partial x_j}\left[\left(\nu + \frac{\nu_t}{\sigma_\varepsilon}\right)\frac{\partial \varepsilon}{\partial x_j}\right] + C_{\varepsilon 1}\frac{\varepsilon}{k}P_k - C_{\varepsilon 2}^*\frac{\varepsilon^2}{k}$$

(A.18)

where

$$C_{\varepsilon 2}^* = C_{\varepsilon 2} + \frac{C_\mu \eta^3 (1 - \eta/\eta_0)}{1 + \beta\eta^3}$$

$$\eta = S\frac{k}{\varepsilon}$$

$$S = \sqrt{2S_{ij}S_{ij}}$$

(A.19)

The Reynolds stress tensor is modeled in the same way as in the standard $k - \varepsilon$, i.e.

$$\nu_t = C_\mu \frac{k^2}{\varepsilon}$$

(A.20)

The closure coefficients are $C_\mu = 0.0845$, $\sigma_k = 0.7194$, $\sigma_\varepsilon = 0.7194$, $C_{\varepsilon 1} = 1.42$, $C_{\varepsilon 2} = 1.68$, $\eta_0 = 4.38$ and $\beta = 0.012$.

A.2.4   The $k - \omega$ SST Turbulence Model

In this two-equation eddy-viscosity turbulence model, the turbulent kinetic energy, k $[m^2/s^2]$, and the specific dissipation rate, ω $[s^{-1}]$, are modeled [30]. The transport equations for the kinetic energy and specific dissipation read

$$
\begin{aligned}
\frac{\partial k}{\partial t} + U_j \frac{\partial k}{\partial x_j} &= P_k - \beta^* k\omega + \frac{\partial}{\partial x_j}\left[(\nu + \sigma_k \nu_t)\frac{\partial k}{\partial x_j}\right] \\
\frac{\partial \omega}{\partial t} + U_j \frac{\partial \omega}{\partial x_j} &= \alpha S^2 - \beta\omega^2 + \frac{\partial}{\partial x_j}\left[(\nu + \sigma_\omega \nu_t)\frac{\partial \omega}{\partial x_j}\right] + 2(1 - F_1)\sigma_{\omega 2}\frac{1}{\omega}\frac{\partial k}{\partial x_i}\frac{\partial \omega}{\partial x_i}
\end{aligned}
\tag{A.21}
$$

The coefficients of the new model (generically called ϕ) are a linear combination of the corresponding coefficients of the $k - \omega$ and $k - \varepsilon$ turbulence models, i.e.

$$
\phi = \phi_1 F_1 + \phi_2(1 - F_1) \tag{A.22}
$$

The closure coefficients are defined as

$$
\begin{aligned}
F_2 &= \tanh\left[\left[\max\left(\frac{2\sqrt{k}}{\beta^* \omega y}, \frac{500\nu}{y^2\omega}\right)\right]^2\right] \\
P_k &= \min\left(\tau_{ij}\frac{\partial U_i}{\partial x_j}, 10\beta^* k\omega\right) \\
F_1 &= \tanh\left\{\left\{\min\left[\max\left(\frac{\sqrt{k}}{\beta^* \omega y}, \frac{500\nu}{y^2\omega}\right), \frac{4\sigma_{\omega 2}k}{CD_{k\omega}y^2}\right]\right\}^4\right\} \\
CD_{k\omega} &= \max\left(2\rho\sigma_{\omega 2}\frac{1}{\omega}\frac{\partial k}{\partial x_i}\frac{\partial \omega}{\partial x_i}, 10^{-10}\right) \\
\phi &= \phi_1 F_1 + \phi_2(1 - F_1) \\
\alpha_1 &= \frac{5}{9}, \; \alpha_2 = 0.44 \\
\beta_1 &= \frac{3}{40}, \; \beta_2 = 0.0828 \\
\beta^* &= \frac{9}{100} \\
\sigma_{k1} &= 0.85, \; \sigma_{k2} = 1 \\
\sigma_{\omega 1} &= 0.5, \; \sigma_{\omega 2} = 0.856
\end{aligned}
\tag{A.23}
$$

Where y is the distance to the nearest wall and ν is the kinematic viscosity. The Reynolds stress tensor is defined as

$$
\nu_t = \frac{a_1 k}{\max(a_1 \omega, SF_2)} \tag{A.24}
$$

The model behaves like a $k - \omega$ turbulence model close to the wall, where $F_1 = 1$, and like the standard $k - \varepsilon$ turbulence model in the free-stream region. The $k - \omega$ turbulence model performs better for boundary layers under adverse pressure gradients than the $k - \varepsilon$ [30]. It may as well be applied throughout the boundary layer, including the viscous-dominated region, without further modification. This model can thus be used as a low-Reynolds number or high-Reynolds number turbulence model. The blending between the two models happens through function F_1.

Appendix B

Numerical Methods

The present work used the OpenFOAM OpenSource CFD tool to compute the incompressible flow in turbomachinery applications. Some of the numerical methods validated in this thesis, such as the General Grid Interface (GGI) [20], were developed by OpenFOAM users, and shared via an OpenFOAM community-driven extension. The present work uses the OpenFOAM-1.5-dev extension released in 2009. Although more recent extensions are now available, OpenFOAM-1.5-dev was the only OpenFOAM version used during the whole period of the work to provide continuity in the numerical results. This appendix discuss some of the numerical methods available in OpenFOAM-1.5-dev, and validated extensively throughout the present work. Section B.1 presents the two approaches used in the present work to predict the rotor-stator interactions and Sec. B.2 describes the GGI coupling interface used to couple the different parts of the mesh.

B.1   Rotor-Stator Interface

Great care needs to be taken in the modelization of the interface between rotating and stationary parts in turbomachinery applications. Different approaches are available in CFD and the choice of the approach depends upon the wanted quality and detail of the rotor-stator interaction. Two rotor-stator interfaces available in OpenFOAM are analyzed in the present work, the frozen rotor and sliding grid interfaces.

B.1.1   Frozen Rotor Approach

In the frozen rotor formulation the rotating and stationary parts are considered to be at a fixed position relative to each other. The coupling between the rotor and stator domains are still resolved 360°, but fixed in time. It is based on the Multiple Frame of Reference (MFR) approach. In a rotating frame of reference, where the relative velocity is computed, the momentum equations must be modified with the Coriolis and centrifugal terms.

The present work uses the MRFSimpleFOAM OpenFOAM solver for the frozen rotor simulations. It is a steady-state solver for incompressible turbulent flow and uses the SIMPLE algorithm for pressure-velocity coupling. The GGI is used to couple the

rotor and stator interfaces, thus allowing non-comformal meshes. Eq. B.1 shows the formulation of the the Reynolds Averaged Navier-Stokes equations implemented in the MRFSimpleFOAM solver.

$$\nabla \cdot (\vec{u}_R \otimes \vec{u}_I) + \vec{\Omega} \times \vec{u}_I = -\nabla(p/\rho) + \nu \nabla \cdot \nabla(\vec{u}_I)$$
$$\nabla \cdot \vec{u}_I = 0 \qquad \text{(B.1)}$$

$\vec{u}_R$ is the velocity relative to the reference frame and $\vec{\Omega}$ is the rotation vector of the reference frame.

B.1.2 Sliding Grid Approach

The sliding grid approach is a transient method that rotates the rotating part of the mesh with respect to the stationary part at each time step. There are different ways to couple the two interfaces. In OpenFOAM, the coupling between the rotating and non-rotating parts of the mesh cane be accomplished by either topological changes, or the General Grid Interface (GGI) [44]. The sliding grid interface approach is the most accurate rotor-stator approach for simulating flows in multiple moving reference frames, but also the most computationally demanding.

The OpenFOAM solver used for the sliding grid approach in this work is named transientSimpleDyMFoam. It is a solver for unsteady incompressible RANS simulations and uses the SIMPLE algorithm for pressure-velocity coupling. The present work uses the GGI to address the physical motion of the mesh. At each time step, the rotating part of the mesh is physically rotated, and the GGI is updated.

B.2 The General Grid Interface

Implicit couplings are present in OpenFOAM in order to join multiple mesh regions into a single contiguous domain. But most of them are built to join conformal mesh regions, where the patches nodes on each side of the interface are matching one to one. The GGI, developed by M. Beaudoin and H. Jasak [20] is a coupling interface used to join multiple non-conformal regions where the patches nodes on each side of the interface do not match.

A GGI is commonly used in turbomachinery, where the flow is simulated through a succession of various complex geometries. The requirement to fit all meshes with conformal matching interface is often very hard to reach. Using the GGI, non-conformal meshes can be designed separately, and joined together using one of many GGI alternatives. The basic GGI is using weighted interpolation to evaluate and transmit flow values across a pair of conformal or non-conformal coupled patches. It is similar to the static sliding interface, although much simpler in the sense that no re-meshing is required for the neighboring cells of the interface. The GGI weighting factors are basically the percentage of surface intersection between two overlapping faces.

Appendix C

Unpublished Results

This appendix presents unpublished results. Section C.1 presents numerical results in the ERCOFTAC Centrifugal Pump and Sec. C.2 presents preliminary results in the U9 Kaplan turbine featured with runner blades tip clearance.

C.1   The ERCOFTAC Centrifugal Pump

This section is a complement of Paper IV. It presents the numerical results obtained with the realizable k-ε, RNG k-ε and k-ω SST turbulence models and compares those results with the experimental data in the radial gap. The results were not presented in Paper IV due to lack of space, and because the turbulence models perform similarly. The ERCOFTAC Centrifugal pump is however a publicly available OpenFOAM test case, and the results might be useful to anyone who wants to attempt similar investigations.

C.1.1   Test Case and Operating Conditions

The ERCOFTAC centrifugal pump test rig was built by Ubaldi *et al.* [36] and consists of a 420 mm diameter unshrouded centrifugal impeller and a 644 mm diameter radial vaned diffuser. Details on the geometry, and coordinates of the impeller blade and diffuser vane profiles are given in Ubaldi *et al.* [36]. The impeller has 7 untwisted constant thickness backswept blades, and the diffuser has 12 vanes. There is a 6% vaneless radial gap between the impeller and diffuser. The tip clearance can be varied, but is set at a value of 0.4 mm, corresponding to 1% of the blade span. The tip clearance is however not included in the present simulations.

The measuring techniques used were hot wire anemometry and fast response pressure transducers. The hot wire probe was used to measure the unsteady three-dimensional flow in the vaneless gap at a radial distance of 4 mm from the blade trailing edge and 8 mm from the vane leading edge. The unsteady static pressure was measured at the front cover facing the unshrouded impeller passages. The experiments were conducted at a constant rotational speed of 2000 rpm, at the nominal operating condition described in Table C.1.

The model operates in an open air circuit directly discharged into the atmosphere from the radial diffuser. The inlet air temperature was 298 K and the air density 1.2 kg/m^3.

Impeller	
$D_1 = 240$ mm	Inlet blade diameter
$D_2 = 420$ mm	Outlet diameter
$b = 40$ mm	Blade span
$z_i = 7$	Number of blades
Diffuser	
$D_3 = 444$ mm	Inlet vane diameter
$D_4 = 664$ mm	Outlet vane diameter
$b = 40$ mm	Blade span
$z_d = 12$	Number of vanes
Operating conditions	
$n = 2000$ rpm	Rotational speed
$U_2 = 43.98$ m/s	Impeller tip speed
$\varphi_c = 0.0048$	Flow rate coefficient
$\Psi_c = 0.65$	Total pressure rise coefficient
$Re = 6.5 * 10^5$	Reynolds number

Table C.1: Geometric data and operating conditions (for more details, see Paper IV)

C.1.2   Computational Domain and Numerical Setup

The meshes for the impeller and diffuser regions were generated separately, see Fig. C.1. Both of the mesh regions are block-structured and were generated using the ICEM-CFD software. O-grids were used around the blades and the diffuser vanes, and H-grids were used in the blade passages. Angular geometrical periodicity was used to mesh the different blades. The impeller tip clearance is not included in the present simulations. The mesh has a total of 2 074 078 nodes. The angles of the cells are between 30° and 140° degrees, with 92% between 70° and 100°. The y^+ values at the walls yield an average value of 50.
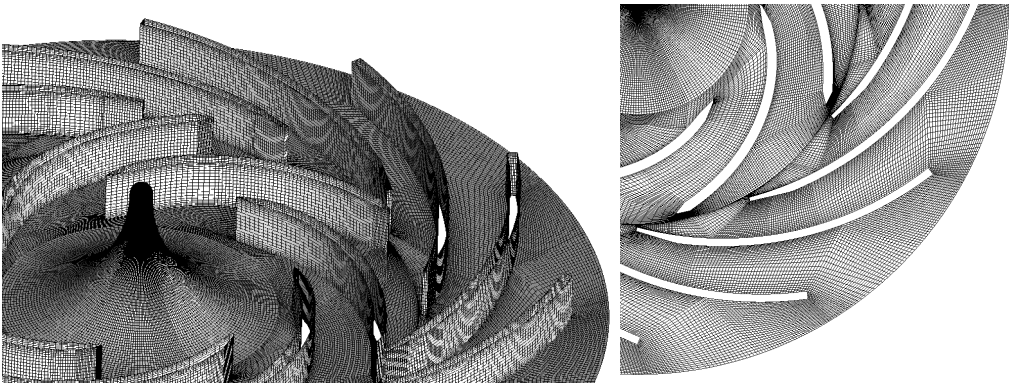

Figure C.1: Computational mesh

The unsteady, 3D, incompressible continuity equation and Reynolds-averaged Navier-Stokes equations are solved. The eddy-viscosity assumption is used to model the turbulence Reynolds stress tensor, and the standard log-law wall function is used at the walls. A second-order linear-upwind scheme [45] is used to discretize the convection terms, and the second-order backward scheme is used to discretize the time derivative. The number of iterations in the transient SIMPLE algorithm at each time step is set to 10. This number of iterations is enough to reduce the residuals by three orders of magnitude. The final residuals are below 10^{-6} except for the pressure, which has a final residual of 10^{-5}. The inlet velocity is set to a constant purely axial component, and the inlet turbulence intensity is assumed to be 5%, with a viscosity ratio of 10. At the outlet, all variables are given a zero gradient boundary condition, except for the pressure which is set to 0. The time step for the unsteady simulations was fixed to $7e^{-5}$ s, which gives a maximum Courant number of 6. The calculations were carried out on a cluster, using 8 nodes equipped with 4 cores each. Using these parameters, one impeller rotation in the unsteady simulation takes 48 hours to compute.

The *sliding grid* approach was used to transfer the rotor-stator interactions. This transient method rotates the impeller part of the mesh with respect to the stator part at each time step. The local fluxes are transferred using the GGI interface, which is updated at every time step. The interaction between the impeller and diffuser is thus fully resolved. The chosen time step corresponds to a rotation of the impeller by about 0.84°. From previous studies, this angular time step is enough to allow the transient solver to resolve the unsteadiness of the wakes [46].

C.1.3 Results and Discussion

The unsteady results using three turbulence models, realizable $k - \varepsilon$, RNG $k - \varepsilon$ and $k - \omega$ SST are presented, and compared to the experimental results in the radial gap. The same results for the $k - \varepsilon$ turbulence model are available in Paper IV.

All the kinematic quantities are normalized with the rotor tip speed, U_2. The circumferential rotor relative coordinate, y_i, and the axial coordinate, z, are made non-dimensional by means of the rotor circumferential pitch, $G_i = 2\pi r/z_i$, and the blade span at the rotor outlet, b, respectively. The velocity comparisons are made at mid-span in the radial gap, at a radius of $1.02 * R_2$. The time, t, is normalized by the rotor blade passing period T_i. Triangle and square symbols in the plots describe the positions of the impeller blades and diffuser vanes, respectively. The results are observed in the relative frame, so that the impeller blades (triangles) have a fixed position in time, while the diffuser vanes (square) moves from left to right.

Figures C.2, C.6 and C.10 show the pressure coefficient in the radial gap for the simulations performed with realizable k-ε, RNG k-ε and k-ω SST, respectively. The three turbulence models perform similarly, predicting the pressure drop in the wakes behind the impeller, but fail in predicting the pressure fluctuations in the diffuser vanes passage.

The radial and tangential velocity profiles in the radial gap are shown for the realizable $k - \varepsilon$, RNG $k - \varepsilon$ and k-ω SST turbulence models in Figs. C.3, C.7 and C.11, respectively. It can be seen that the three turbulence models behave similarly, and predict an horizontal

wake. The measurements realized by Ubaldi *et al.* [36], which are presented in Paper IV, suggest however that the wakes are not horizontal, but rather slightly inclined. The differences between the numerical and experimental results may be explained by the lack of tip clearance secondary flow in the numerical model, as suggested by Ubaldi *et al.* .

Figures C.4, C.8, and C.12 represent the instantaneous distributions of the ensemble-averaged radial velocity in the radial gap at mid-span when using the realizable $k - \varepsilon$, RNG $k - \varepsilon$ and k-ω SST turbulence models, respectively. Likewise, Figs. C.5, C.9, and C.13 represent the instantaneous distributions of the ensemble-averaged tangential velocity in the radial gap at mid-span when using the realizable $k - \varepsilon$, RNG $k - \varepsilon$ and k-ω SST turbulence models, respectively. All the turbulence models predict the flow distribution well. However, the calculations over-predict the maximum of the wake for the tangential velocity, and a slight phase shift is still visible at the maximum of the wakes. Ubaldi *et al.* [36] explain this phase-shift as a consequence of the leakage flow between the impeller blades and the shroud. It is interesting to notice that the calculation using the realizable $k - \varepsilon$ turbulence model predicts very accurately the maximum and minimum peak values of the wakes for the radial velocity, although the wakes are thinner than the ones of the experimental results. The tangential velocity in the impeller wakes is however largely over-predicted when using the realizable $k - \varepsilon$ turbulence model.

Overall, the $k - \varepsilon$, realizable $k - \varepsilon$, RNG $k - \varepsilon$ and k-ω SST turbulence models analyzed in the present work behave similarly and the results do not differ significantly. To improve the quality of the numerical predictions, low Reynolds and hybrid turbulence model could be used to resolve the boundary layer more accurately. Additional terms in the turbulence equations for the rotation of the impeller mesh, and for streamline curvature, could also be investigated. The tip clearance between the impeller blades and the shroud should as well be included in the computational domain, and its impact should be investigated.
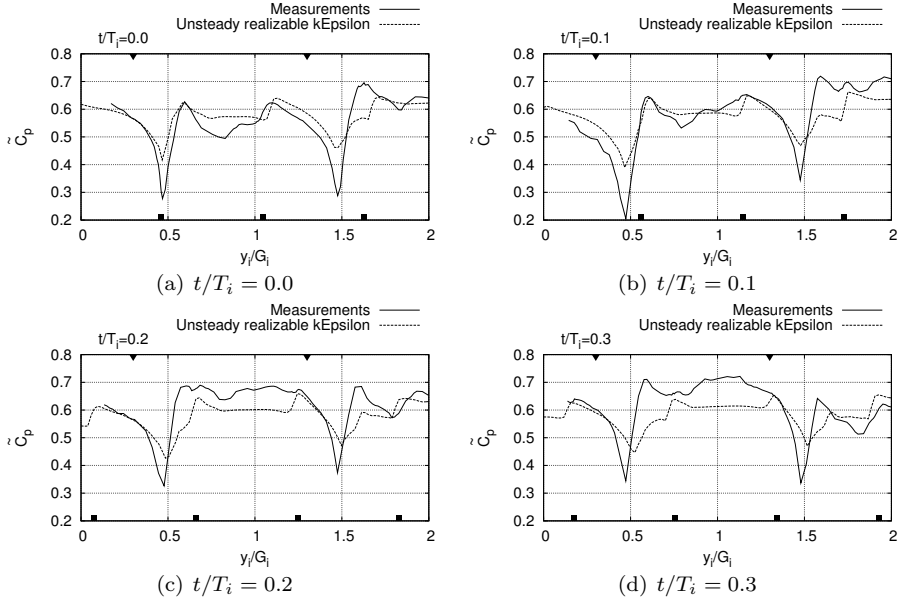
(a) $t/T_i = 0.0$

(b) $t/T_i = 0.1$

(c) $t/T_i = 0.2$

(d) $t/T_i = 0.3$

Figure C.2: Static pressure coefficient $\tilde{C}p$ in the radial gap ($R/R_2 = 1.02$) at mid-span for the unsteady simulation using the realizable $k - \varepsilon$ turbulence model
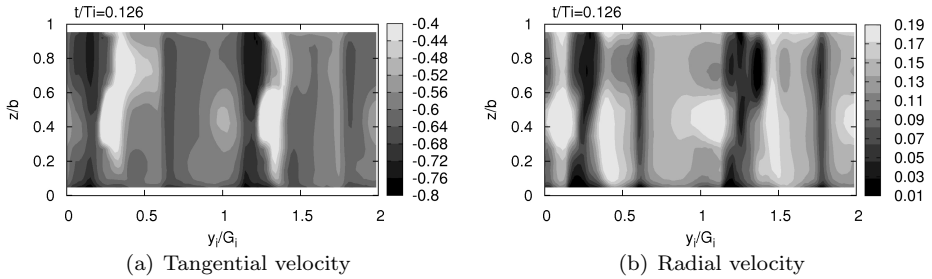

(a) Tangential velocity

(b) Radial velocity

Figure C.3: Tangential and radial velocities in the radial gap ($R/R_2 = 1.02$) for the unsteady simulation using the realizable $k - \varepsilon$ turbulence model
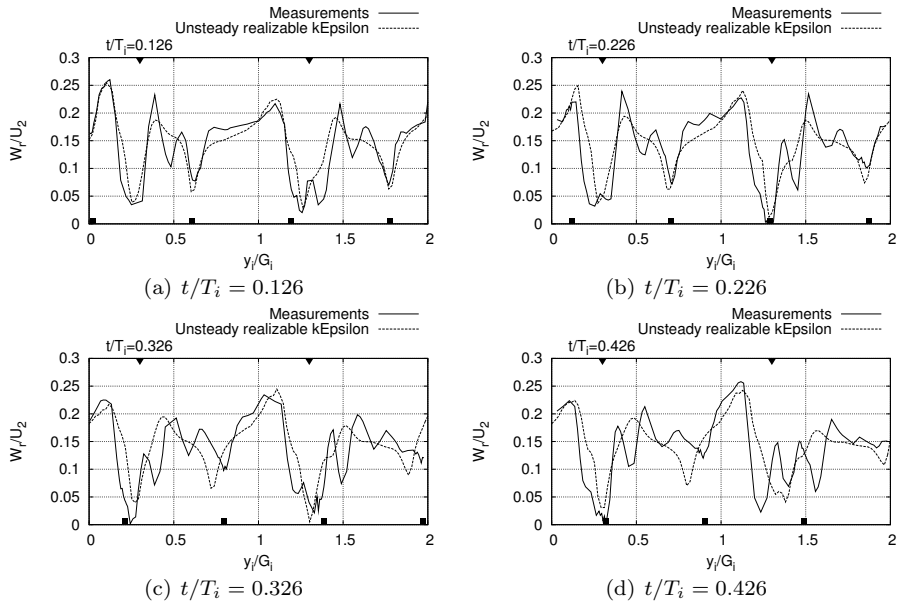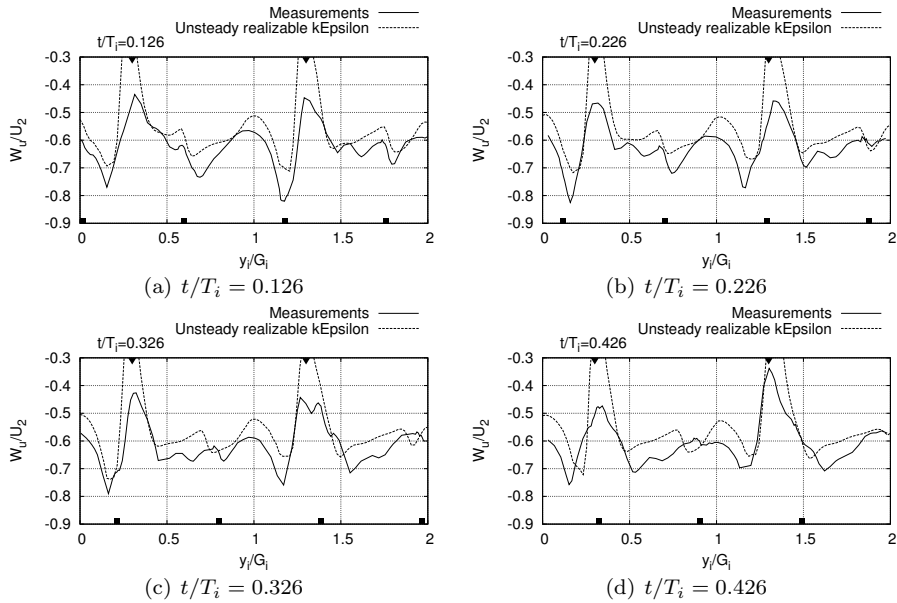
Figure C.4: Radial velocity in the radial gap ($R/R_2 = 1.02$) at mid-span for the unsteady simulation using the realizable $k - \varepsilon$ turbulence model

Figure C.5: Tangential velocity in the radial gap ($R/R_2 = 1.02$) at mid-span for the unsteady simulation using the realizable $k - \varepsilon$ turbulence model
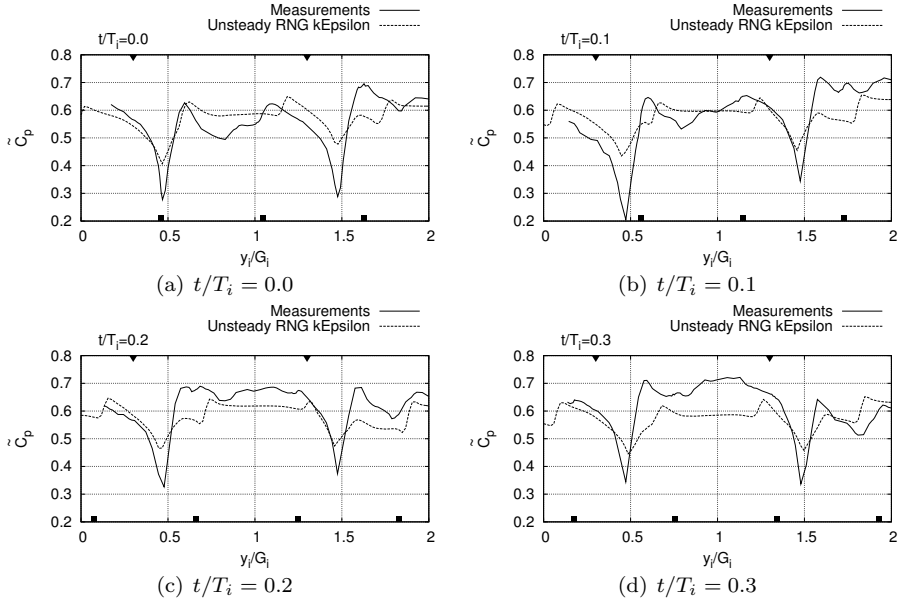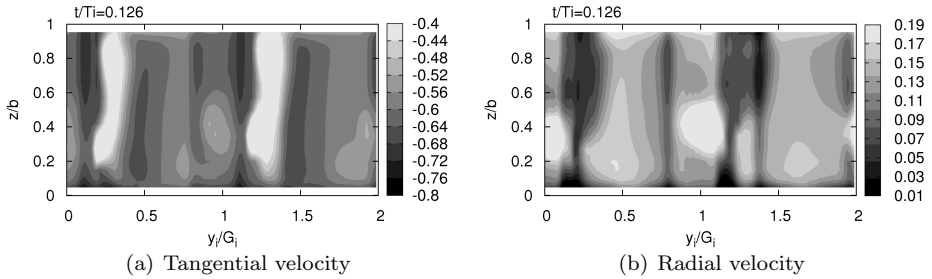
Figure C.6: Static pressure coefficient $\tilde{C}p$ in the radial gap ($R/R_2 = 1.02$) at mid-span for the unsteady simulation using the RNG $k - \varepsilon$ turbulence model

Figure C.7: Tangential and radial velocities in the radial gap ($R/R_2 = 1.02$) for the unsteady simulation using the RNG $k - \varepsilon$ turbulence model
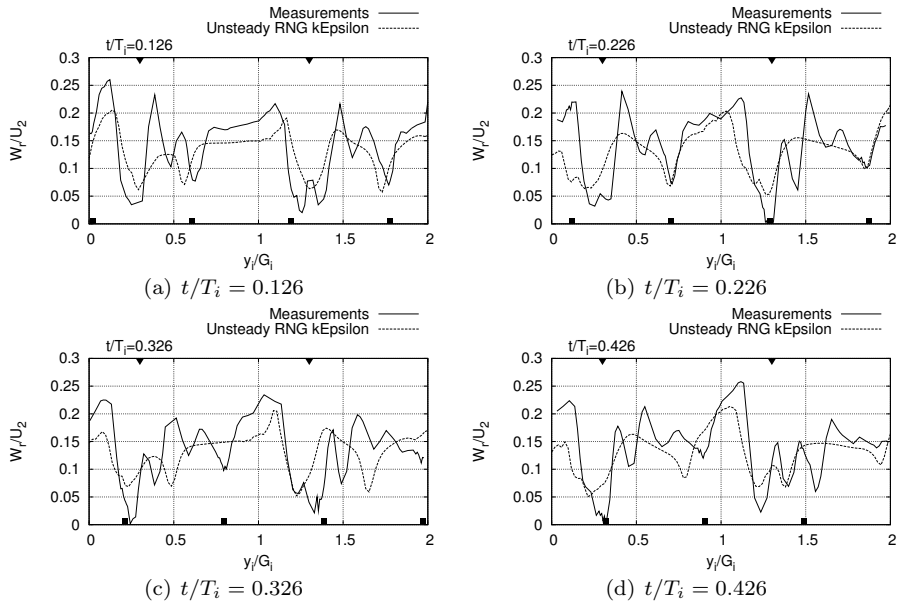
Figure C.8: Radial velocity in the radial gap ($R/R_2 = 1.02$) at mid-span for the unsteady simulation using the RNG $k - \varepsilon$ turbulence model
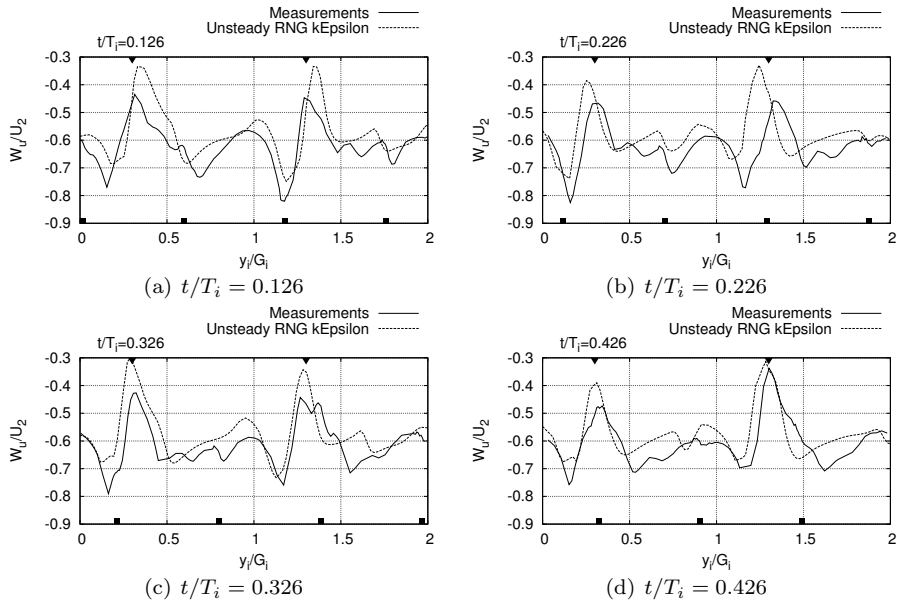

Figure C.9: Tangential velocity in the radial gap ($R/R_2 = 1.02$) at mid-span for the unsteady simulation using the RNG $k - \varepsilon$ turbulence model
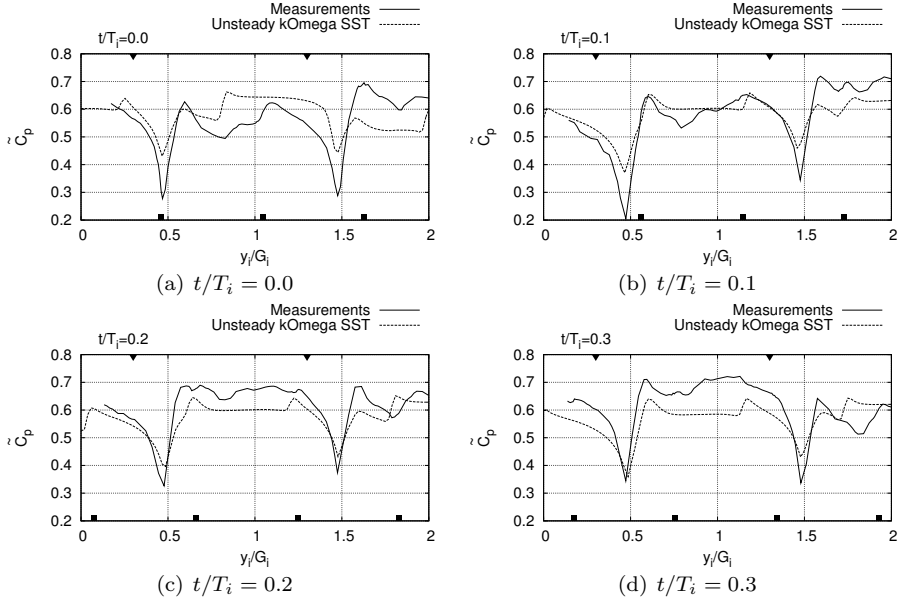
48

(a) $t/T_i = 0.0$

(b) $t/T_i = 0.1$

(c) $t/T_i = 0.2$

(d) $t/T_i = 0.3$

Figure C.10: Static pressure coefficient $\tilde{C}p$ in the radial gap ($R/R_2 = 1.02$) at mid-span for the unsteady simulation using the k-ω SST turbulence model

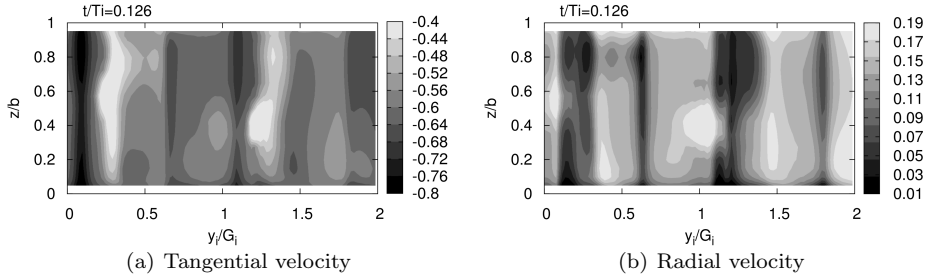(a) Tangential velocity

(b) Radial velocity

Figure C.11: Tangential and radial velocities in the radial gap ($R/R_2 = 1.02$) for the unsteady simulation using the k-ω SST turbulence model
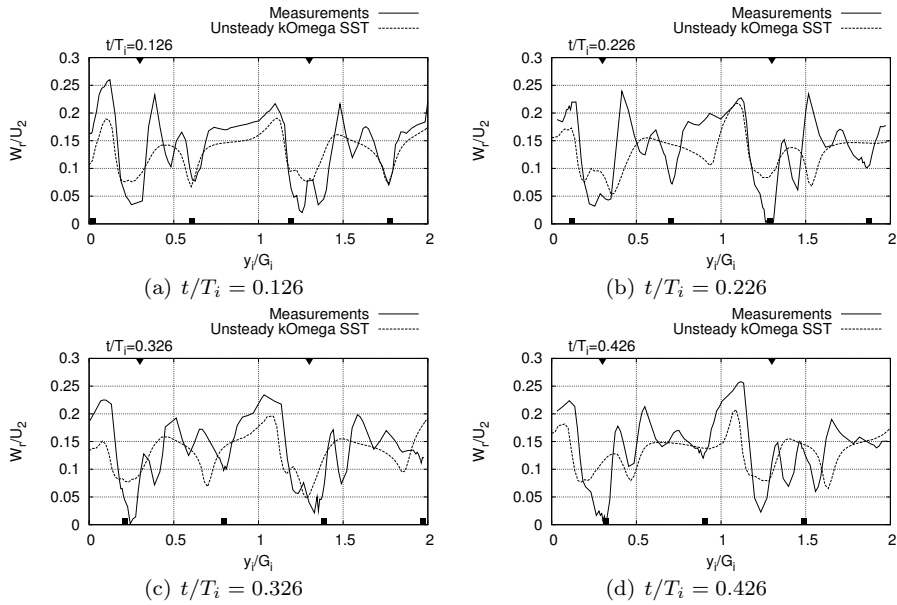
49

Figure C.12: Radial velocity in the radial gap ($R/R_2 = 1.02$) at mid-span for the unsteady simulation, using the k-ω SST turbulence model
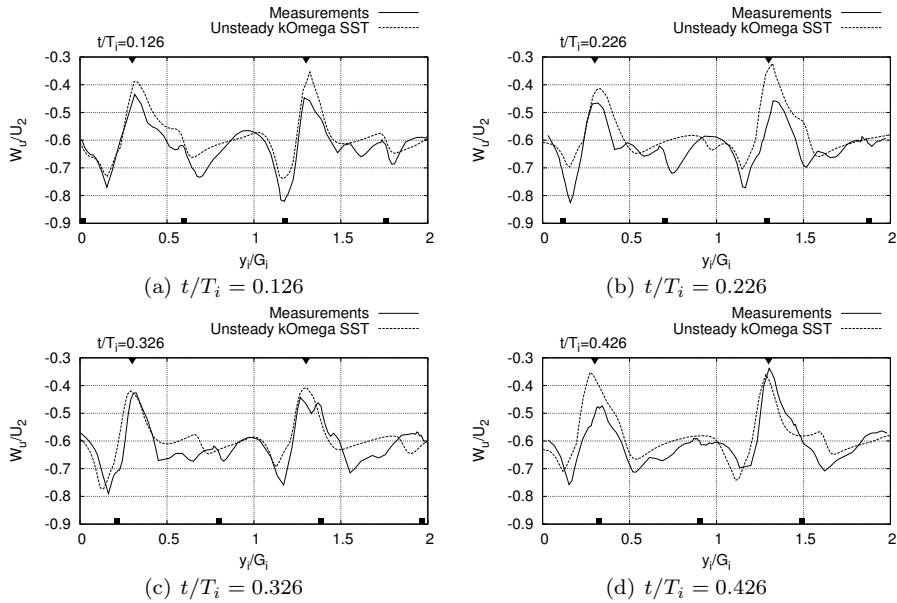
Figure C.13: Tangential velocity in the radial gap ($R/R_2 = 1.02$) at mid-span for the unsteady simulation, using the k-ω SST turbulence model

C.2   The U9 Kaplan Turbine

This section is a follow-up on Paper V, in which the runner blade clearances were not included. It was argued in Paper V that the lack of clearances was the main reason to the differences observed between the numerical and experimental results.

The following sections present preliminary results of the unsteady flow in the U9 Kaplan turbine, from the inlet of the stay vanes until the end of the draft tube. The runner blade hub and tip clearances are included in the computational domain. The numerical velocity profiles are compared to the experimental data in the draft tube cone. Such simulations are computationally heavy, and it takes a long time for the flow to pass the initial transient phase. The following results are thus preliminary, as the flow has yet to fully develop.

C.2.1   Test Rig, Test Conditions and Experimental Database

The U9 Kaplan turbine model, located at Vattenfall Research and Development in Älvkarleby, Sweden, is shown in Fig. C.14(a). The measurements were carried out at three different loads, at best operating point of the turbine and at two off-design operating points (to the left and right of the propeller curve). Table C.2 summurizes the working guide vane angle and the volume flow rate for the three working conditions. The operational net head $H = 7.5$ m, the runner blade angle $\beta = 0.8$ and a runner speed of n=696.3 rpm were used throughout the entire period of measurements.

Operating point	Left	BEP	Right
Guide vane angle (°)	20	26	32
Volume flow rate (m^3/s)	0.62	0.71	0.76

Table C.2: Test conditions parameters

Detailed measurements were made by Mulu *et al.* [39, 40, 41] and Jonsson *et al.* [42]. The velocity measurements were made using a two-component LDA (Laser Doppler Anemometry) technique, at the inlet of the spiral casing, in the spiral casing and in the draft tube cone. In the draft tube cone, windows were mounted at four different angular positions, a: 0°, b: 90°, c: 180° and d: 270° see Fig.C.14(b). The LDA velocity measurements were performed at sections I, II and III for the four different angular positions. The results presented in the following sections focus on one working load of the turbine, at best efficiency point.

C.2.2   Computational Domain, and Numerical Setup

The computational domain is shown in Fig. C.15. It includes the distributor, the Kaplan runner, and the draft tube. The computational mesh is block-structured, and was generated using the ICEM-CFD software, see Fig. C.16. The mesh has a total of about 11 million hexahedral cells. The different parts were meshed separately, and were coupled using the General Grid Interface (GGI), implemented in OpenFOAM by Beaudoin and
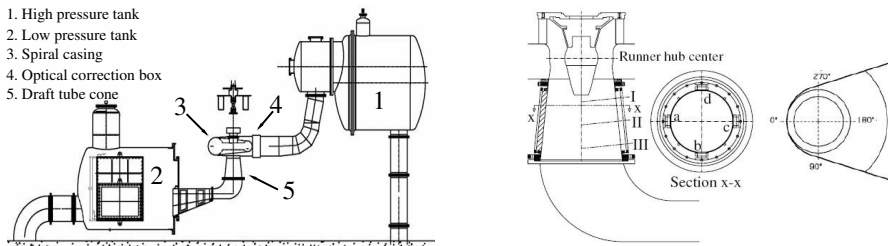
(a) Test rig for the U9 Kaplan turbine model (b) LDA window locations in the draft tube cone where a is at 0°, b at 90°, c at 180° and d at 270°. The velocity measurements were performed at sections I, II and III.

Figure C.14: Test rig of the U9 Kaplan model (a), and LDA window locations (b)

Jasak [20]. The runner blade passage was meshed using O-grids around the blades and H-grids between the blades. It was created for one blade and copied to the other five blades. The blade is cut close to the hub at the leading and trailing edges to allow it to rotate, see Fig. C.17. The runner blade tip is cut with a sphere yielding a tip clearance of 0.4 mm.
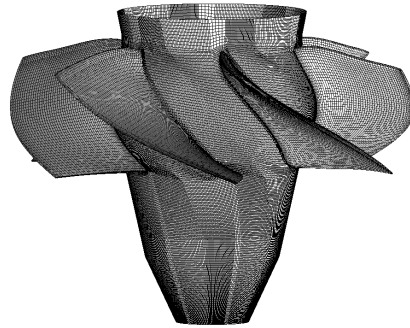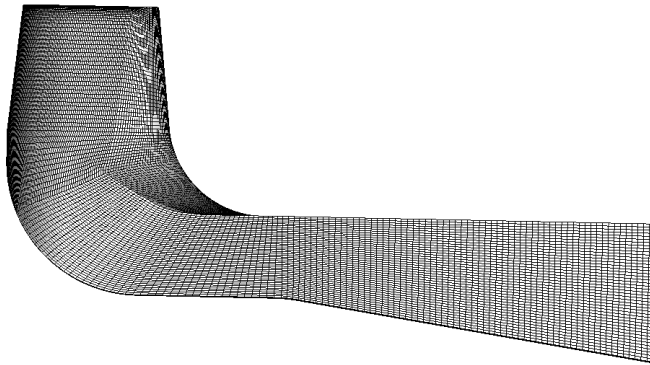

Figure C.15: Computational domain

The unsteady, 3D, incompressible continuity equation and Reynolds-averaged Navier-Stokes equations are solved. The domains are coupled between the rotor and stator using the sliding grid approach. This transient approach rotates the runner part of the mesh with respect to the stationary parts at each time step. The local fluxes between the rotating and stationary parts of the domain are determined by a GGI that updates every time step. The rotor-stator interaction is thus fully resolved. The eddy-viscosity assumption is used to model the Reynolds stress tensor. The high-Reynolds k-ε turbulence
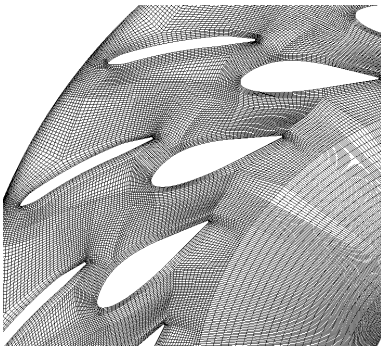
(a) Stay and guide vanes

(b) Runner

(c) Draft tube

Figure C.16: Close-up on different parts of the computational mesh

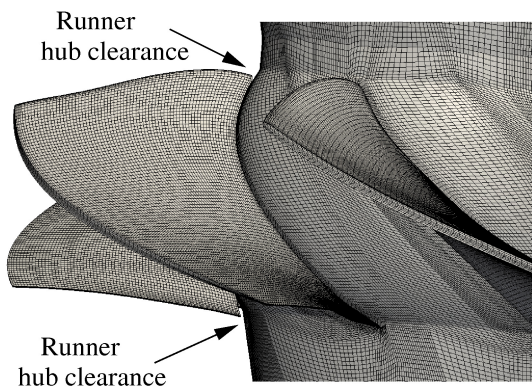Runner
hub clearance

Runner
hub clearance

Figure C.17: Close-up of the modified runner geometry

model is chosen to model the turbulent viscosity. The results from the full U9 Kaplan turbine model simulation, presented in Paper V, is used to specify the angular-resolved velocity, turbulence kinetic energy and turbulence dissipation distributions at the inlet of the distributor. Figure C.18 shows the axial, tangential and radial velocity profiles for the inlet boundary condition. At the outlet, all variables are given a zero gradient boundary condition, except for the pressure which is set to zero. All the walls use a wall-function boundary condition, appropriate for the obtained y^+ values (50-70). The time-step was fixed to $2.4\mathrm{e}^{-4}$ s which gives a maximum Courant number of 10. This corresponds to a rotation of the runner of about 1° per time step. From previous studies, this angular time step is enough to allow the transient solver to resolve the unsteadiness of the wakes [46]. A second-order linear-upwind scheme wass used to discretize the convection terms. The second-order backward scheme was used to discretize the time derivative. The simulation is carried out on a cluster, using 8 nodes equipped with 8 cores each.
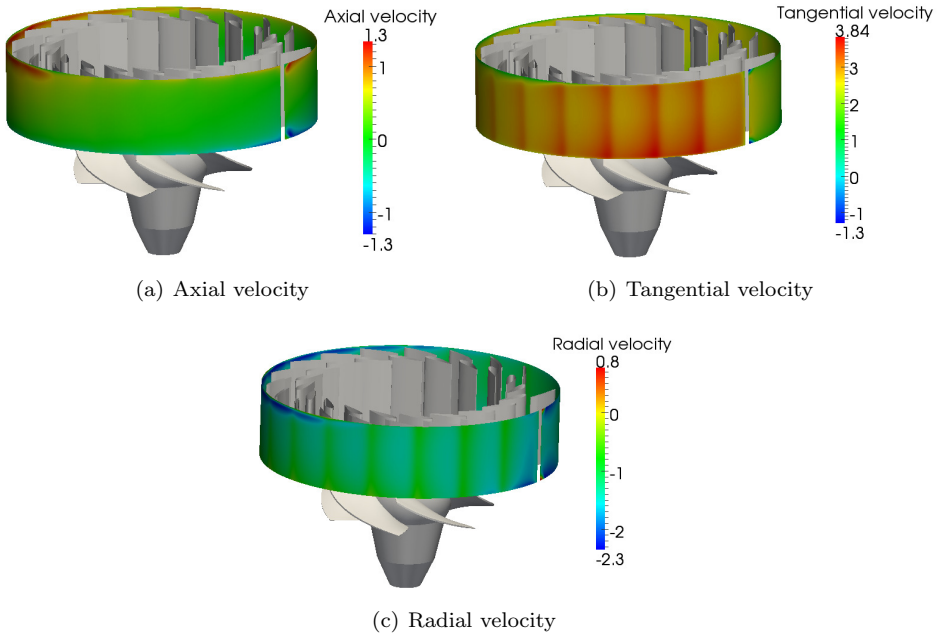

(a) Axial velocity

(b) Tangential velocity

(c) Radial velocity

Figure C.18: Axial, tangential and radial velocity profiles at the inlet of the computational domain

C.2.3 Preliminary Results and Discussion

The unsteady numerical results are here presented and compared against the velocity measurements in the draft tube cone. All the kinematic quantities are normalized with the velocity obtained from the flow rate and the radius of the runner, R=0.25 m. The radii were made dimensionless with the runner radius. The positive directions for the axial and tangential velocities are defined vertically downward through the draft tube cone and clockwise, seen from the top of the runner, respectively.

Figure C.19 presents an overview of the axial velocity in the draft tube, for the unsteady simulation presented in Paper V, and the present simulation. At both the hub and shroud a wider region of reduced axial velocity is observed without the runner clearances. The white line shows the region where axial velocity is zero, indicating where recirculation occurs. The runner blade hub and tip clearances thus significantly reduce the boundary layer thicknesses and the recirculation regions. The secondary flow delays the separation at the walls and reduces the vortex radius below the runner cone.

(a) Without runner blade clearances, simulation from Paper V

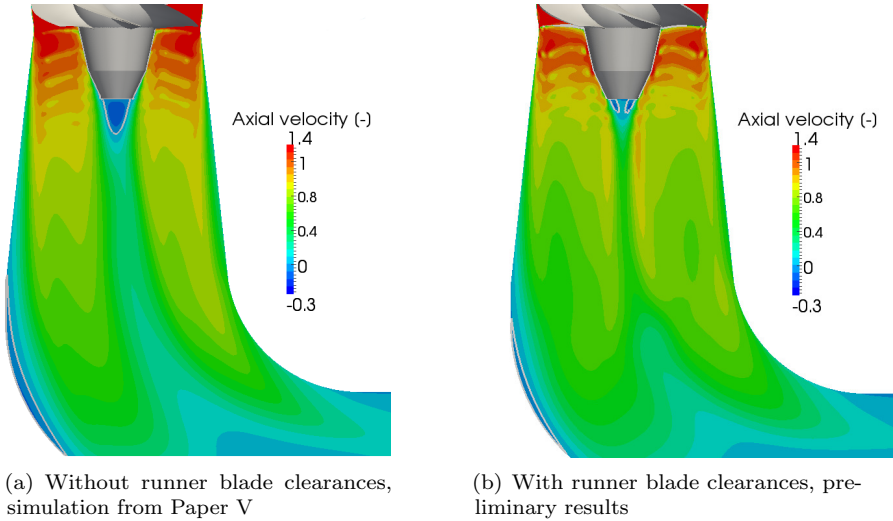(b) With runner blade clearances, preliminary results

Figure C.19: Normalized axial velocity contour plots at mid-plane for the simulations without (a) and with (b) runner blade clearances, using the $k - \varepsilon$ turbulence model

Figure C.20 shows the measured and computed axial and tangential velocity profiles, at sections I, II and III, for the simulations without and with the runner clearances. Both the experimental and numerical velocity profiles have a negligible variation between positions a, b, c and d. Thus, for clarity, the velocity profiles are only presented for window a.

For the simulation without the runner blade clearances, there are significant differences between the measured and computed velocity profiles. In the experimental results, a vortex is created below the runner cone, generating a region where high velocities and large velocity gradients can be found. This is not well-predicted by the simulation. The computed velocities at $r^* \approx 0.2$ do not show the same increment as the experimental ones.

Also, the shroud boundary layer is much wider in the numerical results than that of the experimental results.

When the clearance flows are taken into account, the simulation predicts more accurately the behaviour of the flow. Below the runner, the separation zone is greatly reduced, and is of the same order of magnitude as the measured one. The axial velocity is rather well predicted, but although some improvements can be shown on the tangential velocity, it is still not accurate enough. It should be noted that the flow is still not fully developed, and that the velocity profiles will continue to evolve. At section III, the tangential velocity is not in good agreement with the measurements, and a counter swirl appears. Section III is further downstream and therefore less developed than the velocity profiles at section I and II. However, this behavior was observed as well at section I and II at earlier stage of the simulations, see Fig. C.21. This behavior appears to be linked with the transient phase, and this counter swirl disappears when the flow fully develops.

From the preliminary results shown in this section, the secondary flow induced by the runner blades clearances seem to help in predicting the flow more accurately. The flow is forced close to the wall , and the separation at the draft tube elbow is greatly reduced. The runner blade clearances is thus a very important feature, and should be included in future simulations. The quality of the inlet boundary condition in this simulation should as well be analysed. A constant mass flow rate with a flow direction is a more common inlet boundary condition for such a simulation and has proven to give reasonably good results. However, in reality, the flow at the inlet of the distributor is not uniform. Simulations performed with the two inlet boundary conditions should be compared to analyze the impact this simplification has on the flow.
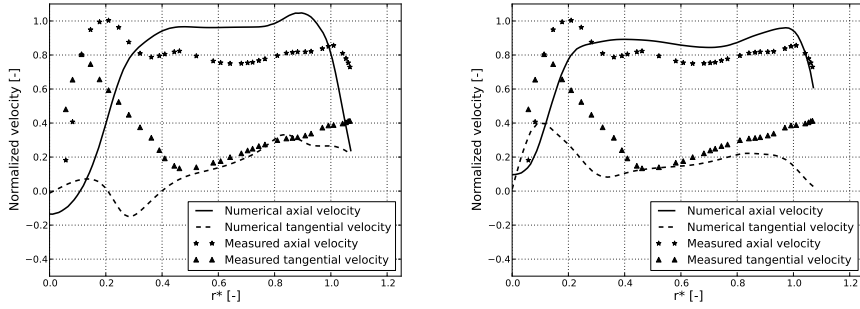
(a) Section I
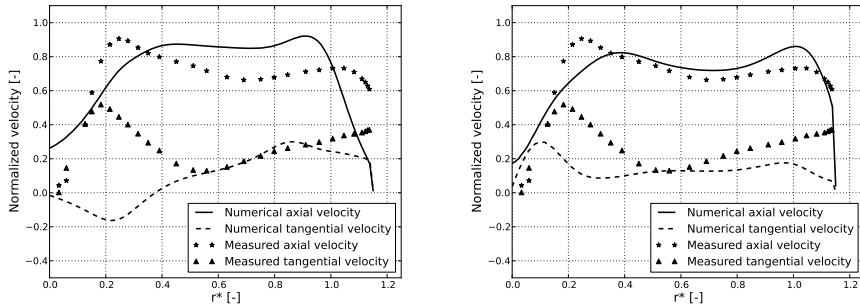
(b) Section II
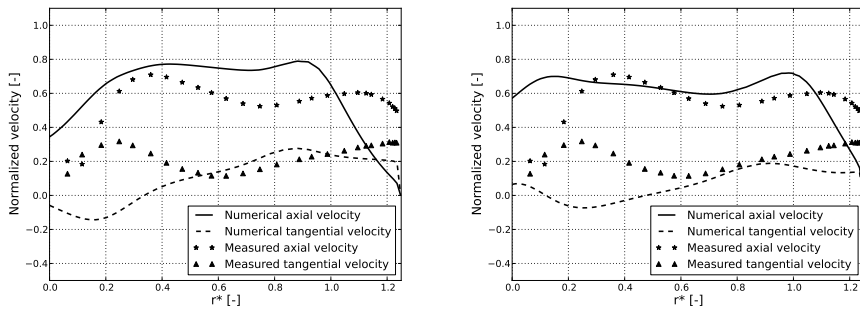
(c) Section III

Figure C.20: Normalized tangential and axial velocity profiles at section I (a), II (b) and III (c) for the simulation without (left) and with (right) runner blades clearances
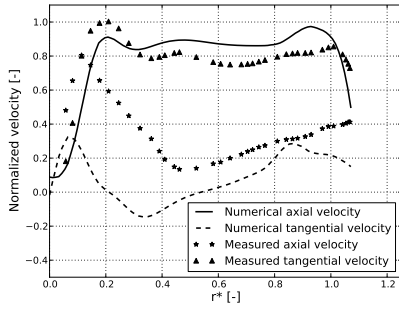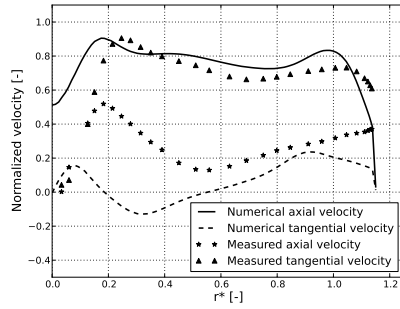
(a) Section I　　　　　　　　　　(b) Section II

Figure C.21: Normalized tangential and axial velocity profiles at section I (a) and II (b) during the initial transient phase. The flow is not fully developed, and a counter swirl appears below the runner. This swirl disappears then when the flow develops.

Appendix D

Appended Papers I–V

Paper I

The ERCOFTAC Centrifugal Pump OpenFOAM Case-Study

By

O. Petit, M. Page, M. Beaudoin and H. Nilsson

The ERCOFTAC centrifugal pump OpenFOAM case-study

Olivier PETIT

Chalmers University of Technology, Göteborg, Sweden

Maryse PAGE

Hydro-Québec, Institut de recherche, Varennes, Canada

Martin BEAUDOIN

Hydro-Québec, Institut de recherche, Varennes, Canada

Håkan NILSSON

Chalmers University of Technology, Göteborg, Sweden

ABSTRACT

This work investigates the rotor-stator interaction features of OpenFOAM-1.5-dev, such as frozen rotor and sliding grid. The case studied is the ERCOFTAC *Test Case U3: Centrifugal Pump with a Vaned Diffuser*, a testcase from the ERCOFTAC Turbomachinery Special Interest Group. The case was presented by Combès at the *ERCOFTAC Seminar and Workshop on Turbomachinery Flow Prediction VII*, in Aussois, 1999. It is a valid test case for evaluation of rotor-stator interaction features, as detailed experimental data is available.

The investigation shows that OpenFOAM gives results that are comparable to the experimental data, in particular for the sliding grid case. The results are less accurate in the frozen rotor simulation due to the improper treatment of the impeller wakes that is part of the frozen rotor formulation.

The ERCOFTAC centrifugal pump OpenFOAM case-study was developed as a contribution to the OpenFOAM Turbomachinery Working Group, and was presented and discussed at the Fourth OpenFOAM Workshop in Montréal, 2009. The complete set-up of the case-study is available from the OpenFOAM-extend project at SourceForge, and instructions and comments are available from the OpenFOAM Wiki.

KEYWORDS

CFD, OpenFOAM, Turbomachinery, Frozen rotor, Sliding grid, GGI, ERCOFTAC centrifugal pump

1 INTRODUCTION

OpenFOAM is an Open Source library written in C++ [1]. It is a well-structured code, mostly used to implement CFD solvers, although it is also used in other applications. OpenFOAM is based on the finite volume method, but there are also implementations of the finite area and finite element methods. The code accepts fully unstructured meshes and polyhedral cells. Many advanced features can be found in OpenFOAM, such as moving meshes and conjugate heat transfer. With regards to basic features, such as turbulence models and discretization schemes, OpenFOAM is a serious and high quality CFD tool that is constantly evolving.

The community-driven OpenFOAM Turbomachinery Working Group [2] develops and validates OpenFOAM for turbomachinery applications. The ERCOFTAC centrifugal pump was chosen as a validation test case for this investigation of the rotor-stator interaction features in OpenFOAM. The results of the initial studies of this case were presented at the Fourth OpenFOAM Workshop in June 2009, in Montréal, Québec. All the files are available at the OpenFOAM-extend project at SourceForge, for anyone who would like to learn OpenFOAM, or become familiar with the turbomachinery features in OpenFOAM. Some of the important features, such as the GGI (General Grid Interface), multiple frames of reference, and moving meshes are described in the present paper. The GGI forms the base for many useful features for turbomachinery.

2 METHOD

In this work, the flow through a centrifugal pump is investigated. The incompressible Reynolds-Averaged Navier-Stokes equations are solved, using the finite volume method and a standard k-ε turbulence model closure with wall-functions. The convection discretization uses a second-order linearUpwind scheme. Two different rotor-stator approaches are used:

- The *frozen rotor* approach is a steady-state formulation where the rotor and stator are fixed with respect to each other, and different reference frames are used in the rotating and stationary parts. This is also referred to as Multiple Reference Frames (MRF), and it allows taking into account the effect of the rotation of the impeller, although no transient rotor-stator interaction is included. It is nevertheless a fast preliminary method, for use as initial conditions for sliding grid simulations.
- The *sliding grid* approach is a transient method where the rotor mesh actually rotates with respect to the stator mesh. The interaction between the rotor and stator are thus fully resolved. This requires a sliding grid interface between the rotor and stator domains. In OpenFOAM there are two alternatives for sliding interfaces, GGI and topology changes.

Details on the two approaches can be found in section 4.

3 THE ERCOFTAC CENTRIFUGAL PUMP CASE-STUDY

The ERCOFTAC centrifugal pump is a simplified model of a centrifugal turbomachine. The original test case was presented by Combès [3] at a Turbomachinery Flow Prediction ERCOFTAC Workshop in 1999.

3.1 Geometry

The simplified model of the centrifugal pump has 7 impeller blades, 12 diffuser vanes and 6% vaneless radial gap as shown in Fig. 1. The geometric data and operating conditions are shown in Tab. 1. The test rig was built by M.Ubaldi et al.[4]. The purpose was to study the flow unsteadiness generated by rotor-stator interaction in a turbomachine.
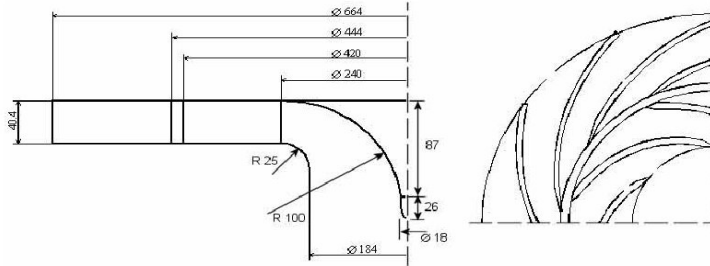

Fig. 1: Impeller and vaned diffuser geometry (Image taken from Ubaldi et al. [4]).

Impeller		Diffuser		Operating conditions	
Leading edge diameter	$D_1 = 240mm$	Leading edge diameter	$D_3 = 444mm$	Rotational speed	$n = 2000rpm$
Trailing edge diameter	$D_2 = 420mm$	Trailing edge diameter	$D_4 = 664mm$	Impeller tip speed	$U_2 = 43.98m/s$
Number of blades	$z_i = 7$	Number of vanes	$z_d = 12$	Flow rate coefficient	$\varphi = \dfrac{4Q}{U_2 \pi D_2^2} = 0.048$
Blade span	$z = 40.4mm$	Outlet diameter	$D_5 = 750mm$	Total pressure rise coefficient	$\psi = \dfrac{2(p_{out} - p_{in})}{8\rho U_2^2} = 0.65$
				Reynolds number	$Re = \dfrac{U_2 l}{v} = 6.5 * 10^5$
				Air density	$\rho = 1.2 kg/m^3$

Tab. 1: Geometric data and operating conditions [4].

3.2 Measurements

The experimental data was provided by Ubaldi et al. [4]. The model operates in an open circuit with air directly discharged into the atmosphere from the radial diffuser. The pump operates at the nominal operating condition, at a constant rotational speed of 2000 rpm. (Reynolds number: 6.5×10^5, incompressible flow regime). Phase locked ensemble averaged velocity components have been measured with hot wire probes at the impeller outlet. The data includes the distribution of the ensemble averaged static pressure at the impeller front end, taken by means of miniature fast response transducers mounted at the stationary casing of the impeller. LDV measurements were also performed in the impeller and in the diffuser.
The measurements made by Ubaldi were made using a hot-wire probe at a radial distance 4 mm from the blade trailing edge ($D_m/D_2 = 1.02$). The results from the simulations were extracted in a similar way, as shown in Fig. 2.
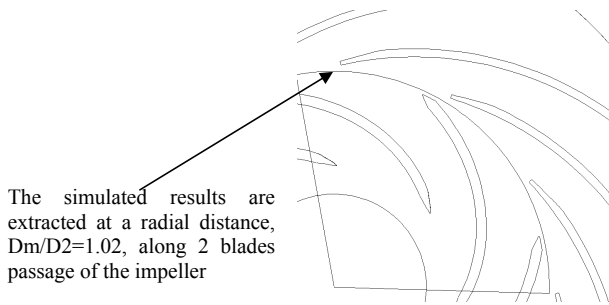
The simulated results are extracted at a radial distance, Dm/D2=1.02, along 2 blades passage of the impeller

Fig. 2: Position of the hot-wire probe, and of the sampling of the simulated data.

3.3 Case-study set-up and cases

The ERCOFTAC centrifugal pump was used as a case study for the Fourth OpenFOAM Workshop, held in Montréal, Québec, in June 1-4 2009. It can be found in the turbomachinery Special Interest Group web page at the OpenFOAM Wiki (http://openfoamwiki.net/index.php/Sig_Turbomachinery), and in the OpenFOAM-extend SourceForge project (http://sourceforge.net/projects/openfoam-extend/). It includes block-structured meshes, scripts that automatically set up the cases, and automatic post-processing of the results and comparison with the measurements. There are also written descriptions of the OpenFOAM features that are used for the case-study.

In the present work, a 2D representation of the geometry is used. Previous simulations have been done by Bert, Combès and Kueny [5], who showed that relevant information could be recovered from 2D simulations although the real flow has 3D features. The 2D mesh was made using ICEM-HEXA, and the rotor and the impeller were meshed separately. The mesh is block-structured, and consists of about 94 000 cells, with an average Y+ value of 35. The boundary conditions are shown in Tab. 2.

Calculated data for the 2D cases		Boundary conditions	
Inlet Diameter	D_0=200 mm	At the inlet	$V_{radial} = U_0$ $\frac{\mu_T}{\mu} = 10$ (viscosity ratio) $k = \frac{3}{2}U_0^2 I^2 = 0.48735 m^2/s^2$ (I=5%) $\varepsilon = \frac{C_\mu \rho k^2}{\mu_T} = \frac{C_\mu \rho k^2}{\mu(\mu_T/\mu)} = \frac{C_\mu k^2}{v(\mu_T/\mu)}$
Z thickness (OpenFOAM requires one cell thickness in 2D)	Z = 1mm		
Flow rate	$Q = \frac{\varphi U_2 \pi D_2^2}{4} = 0.292 m^3/s$		
Inlet radial speed	$U_0 = \frac{Q}{A_0} = \frac{Q}{2\pi r_0 z} = 11.4 m/s$	At the outlet	Average static pressure 0

Tab. 2: Computational parameters for the 2D cases.

The ERCOFTAC centrifugal pump (ECP) cases that are currently available are listed here:

- ➤ Steady state frozen rotor cases, using MRF (Multiple Reference Frames)

  - ◦ *ECPGgi2D*: The frozen rotor approach, and the GGI between the impeller and the diffuser.

  - ◦ *ECPStitchMesh2D*: The frozen rotor approach, where the rotor and stator meshes have been stitched together at the interface, forming a single mesh with hanging nodes at the interface.

- ➤ Unsteady sliding grid cases

  - ◦ *ECPMixerGgiFvMesh2D*: The sliding grid approach, where the GGI is applied between the impeller and the diffuser at each time step.

  - ◦ *ECPMixerFvMesh2D*: The sliding grid approach, where the rotor and stator meshes are stitched together at the interface at each time step, forming a single mesh with hanging nodes at the interface at each time step.

3.4 Results

3.4.1 Steady-state simulation – frozen rotor

The simulation was stopped after 5000 iterations, since all the residuals were below 10^{-5}. The frozen rotor approach gives something that resembles a snapshot of the real flow in the pump, but the advection of the impeller wakes in the diffuser region will by definition not be physical (see Fig. 3).
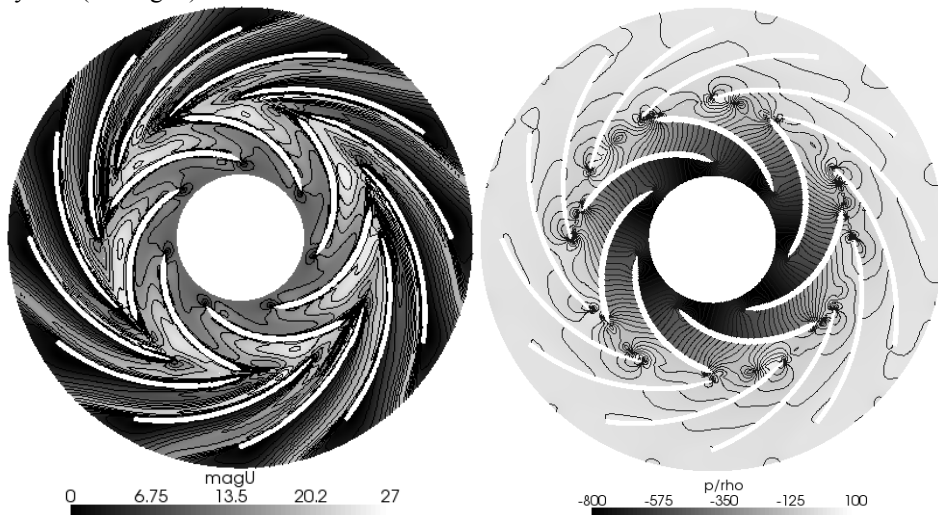

Fig. 3: Velocity magnitude and static pressure for the pump, for the frozen rotor simulation.

The computed velocities show some similarity with the experimental data, as shown in Fig. 4, however, the results do not agree perfectly with the experimental ones. Most of these differences are likely due to the frozen rotor formulation rather than the OpenFOAM implementation. A comparison with preliminary results from a commercial CFD code [6] shows that OpenFOAM gives similar results as commercial CFD codes for frozen rotor simulations.

The GGI and the stitched cases give exactly the same results as can be seen in Fig. 4, and it can thus be concluded that the interface coupling works as it should.
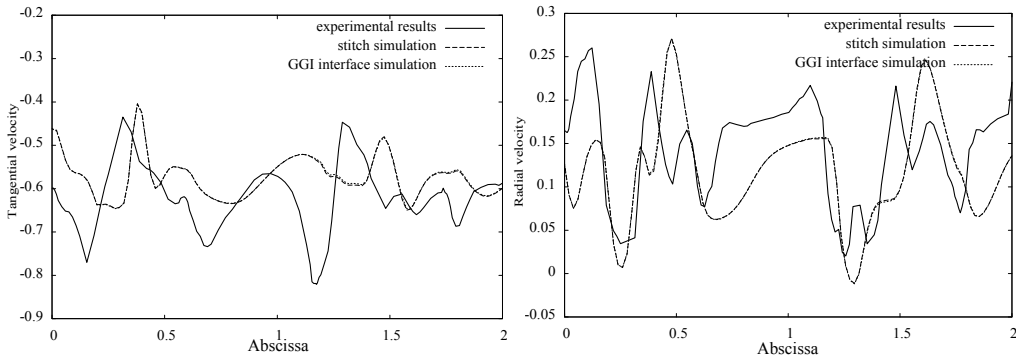

Fig. 4: Distributions of the tangential and radial velocities, for the two frozen rotor simulations compared to the experimental data. The two simulation results are identical.

3.4.2 Unsteady simulation, using the sliding grid approach

Both computations (*ECPMixerGgiFvMesh2D* and *ECPMixerFvMesh2D*) give the same results. Therefore, only the GGI approach will be discussed here.

With the unsteady simulation, the wakes are more visible, and they are advected properly between the diffuser blades, as shown in Fig. 5. There is a better, although not perfect, agreement between the simulations and the experimental data, compare to the frozen rotor simulation, see Fig. 6. However, the tangential velocity is slightly over-predicted.
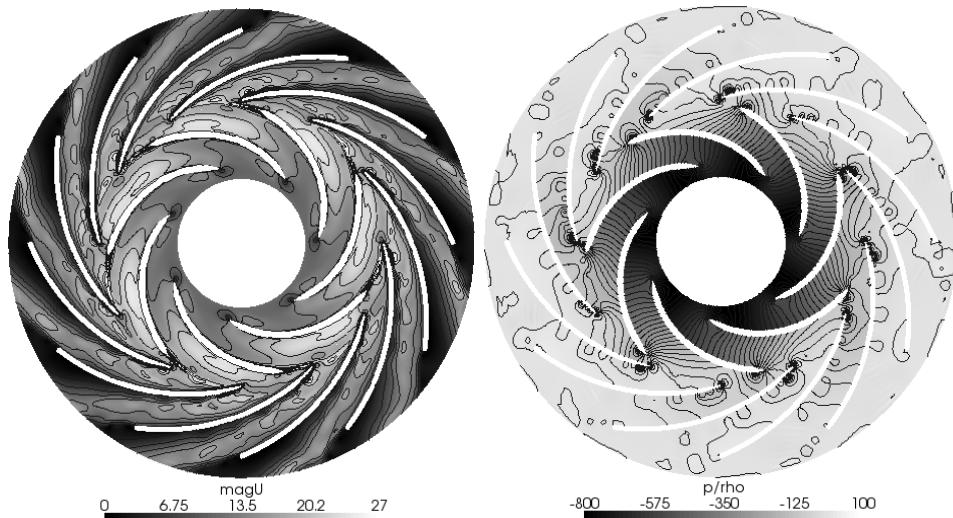

Fig. 5: Velocity magnitude and static pressure for the ERCOFTAC centrifugal pump, for the unsteady simulation
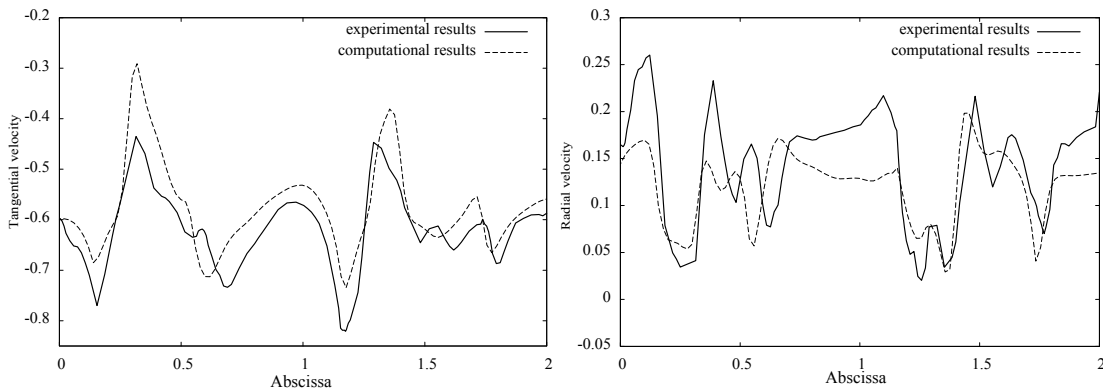
6

Fig. 6: Distributions of tangential and relative velocity for the unsteady simulation, compared to the experimental data.

4 IMPLEMENTATION DETAILS

4.1 Steady-state solver for Multiple Reference Frames

The solver used for the frozen rotor simulations, based on the Multiple Reference Frame (MRF) approach is named MRFSimpleFoam. It is a steady state solver for incompressible turbulent flow, using the SIMPLE algorithm for pressure-velocity coupling. The MRF approach implies that there is no relative mesh motion of the rotating and stationary parts. In a rotating reference frame, where the relative velocity is computed, the momentum equations must be modified with Coriolis and centrifugal terms. In the MRF approach, the momentum equations uses a mix of inertial and relative velocities, and only one extra term appears in the equations. Tab. 3 summarizes the formulation of the Reynolds Averaged Navier-Stokes equations in the inertial and the rotating frames, and the third alternative is what is implemented in MRFSimpleFoam.

Frame	Convected velocity	Steady incompressible Navier-Stokes equations
Inertial	Absolute velocity	$\nabla \cdot (\vec{u}_I \otimes \vec{u}_I) = -\nabla(p/\rho) + \nu\nabla \cdot \nabla(\vec{u}_I)$ $\nabla \cdot \vec{u}_I = 0$
Rotating	Relative velocity	$\nabla \cdot (\vec{u}_R \otimes \vec{u}_R) + 2\vec{\Omega} \times \vec{u}_R + \vec{\Omega} \times \vec{\Omega} \times \vec{r} = -\nabla(p/\rho) + \nu\nabla \cdot \nabla(\vec{u}_R)$ $\nabla \cdot \vec{u}_R = 0$
Rotating	Absolute velocity	$\nabla \cdot (\vec{u}_R \otimes \vec{u}_I) + \vec{\Omega} \times \vec{u}_I = -\nabla(p/\rho) + \nu\nabla \cdot \nabla(\vec{u}_I)$ $\nabla \cdot \vec{u}_I = 0$

Tab. 3: Summary of the Navier-Stokes equations for steady flow in multiple reference frames.

4.1.1 Frozen rotor

In the frozen rotor formulation, the rotating and stationary parts are considered to be at a fixed position relative to each other. The coupling between the rotor and stator domains are still resolved 360°, but fixed in time. Since the rotor and the stator parts have been meshed separately, a connection must be made between these meshes. Two methods can be used for that in OpenFOAM. The first one is based on the topological changes technology (see section 4.3). The second method is the GGI (see section 4.4).

4.1.2 Mixing plane

Another solution to model the interface between the rotating and stationary parts is the mixing plane. At the interface the flow properties are circumferentially averaged. This will of course remove all transient rotor-stator interactions, but it still gives fairly representative results. A mixing-plane simulation only requires one rotor blade and one stator blade per stage, which significantly accelerates the solution procedure.

The mixing plane is under implementation in OpenFOAM at the moment, but there should be an implementation available in the coming year.

4.2 Unsteady solver for sliding grid

The solver used for the sliding grid simulations in this work is named turbDyMFoam. This is a solver for incompressible RANS simulations using the PISO algorithm for pressure-velocity coupling. The solver also uses libraries for mesh motion and deformation of polyhedral meshes [7], of which one of them handles partly rotating meshes. In the simulations the physical motion of the mesh is directly addressed. The coupling between the rotating and non-rotating parts of the mesh can be accomplished by either topological changes (see section 4.3) or GGI (see section 4.4).

4.3 Topological changes

Two parts of a mesh with coinciding faces can be attached to each other by connecting the faces of both parts. If the resulting mesh would not be conformal, OpenFOAM allows polyhedral cells, and may thus cut the faces to make the mesh conformal with hanging nodes. The sliding interface with topological changes in OpenFOAM uses this functionality at each time step, and deals with the topological changes associated to it. The topological modifier attach-detach is then used, and the rotating part of the mesh is detached from the static part. The rotation then occurs, and the mesh is attached again, as explained in Fig. 7. The black points show the vertices of a 2D cell, and it is shown that a non-conformal connection gives control volumes with hanging nodes.
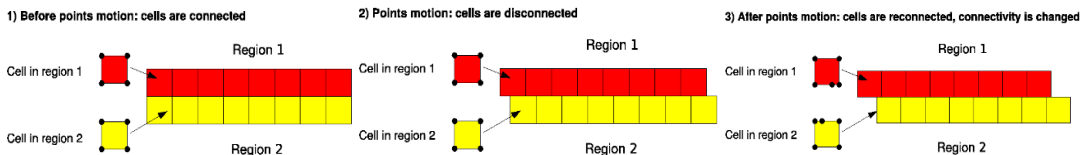

Fig. 7: Operation of a sliding interface, pictures from [7].

This operation can be quite time-consuming, as it needs to re-organize the topology and the internal numbering of faces and cells at each time step. However, the method is fully conservative.

4.4 General Grid Interface (GGI)

The GGI can be used to speed up the operation of the coupling between the rotor and stator domains. With the GGI, the modus operandi is quite similar as for the topological change method. The neighbours still need to be evaluated, but the attach-detach topological modifier doesn't need to be called anymore. This is a gain of time at each time step that is very noticeable on the whole simulation.

Implicit couplings are present in OpenFOAM in order to join multiple mesh regions into a single contiguous domain. But most of them are built to join conformal mesh regions, where

the patches nodes on each side of the interface are matching one to one. The GGI, developed by M. Beaudoin and H. Jasak [8] is a coupling interface used to join multiple non-conformal regions where the patches nodes on each side of the interface do not match.

A GGI is commonly used in turbomachinery, where the flow is simulated through a succession of various complex geometries. The requirement to fit all meshes with conformal matching interface is often very hard to reach. Using the GGI, non-conformal meshes can be designed separately, and joined together using one of many GGI alternatives.

The basic GGI is using weighted interpolation to evaluate and transmit flow values across a pair of conformal or non-conformal coupled patches. It is similar to the static sliding interface, although much simpler in the sense that no re-meshing is required for the neighbouring cells of the interface. The GGI weighting factors are basically the percentage of surface intersection between two overlapping faces.

The GGI implementation is using the Sutherland-Hodgman algorithm to compute the master and shadow face intersection surface area [9]. This algorithm is simple, fast and robust; being re-entrant, it allows for a very compact source code implementation. The Sutherland-Hodgman algorithm is also generic enough to handle any convex n-sided polygons.

5 Conclusions

The rotor-stator interaction features of OpenFOAM have been investigated and compared with experimental data of the ERCOFTAC centrifugal pump with a vaned diffuser. Both steady state simulations using Multiple Reference Frames and unsteady simulations using a transient solver with sliding mesh were performed. Good agreements were found with the experiments, but improvements can be made. The unsteady simulation showed a good behavior of the wakes being advected through the diffuser. It can be concluded that all the functionality is available in OpenFOAM for accurate rotor-stator analysis.

In order to improve the numerical results the same simulations will be performed in 3D, and alternative boundary conditions will be investigated. The coming mixing plane implementation will also be evaluated in the same case, and a tutorial on how to use the mixing plane will be released to the OpenFOAM community.

6 ACKNOWLEDGEMENTS

7 REFERENCES

[1] Weller H.G, Tabor G, Jasak H, Fureby C., *"A tensorial approach to computational continuum mechanics using object-oriented techniques"*, Computers in Physics, Vol.12, No.6, 1998.

[2] Nilsson H., Page M., Beaudoin M., Gschaider B. and Jasak H., *"The OpenFOAM Turbomachinery Working Group, and Conclusions from the Turbomachinery Session of the Third OpenFOAM Workshop"*, 24th IAHR Symposium on Hydraulic Machinery and Systems, October 27-31, 2008, Foz Do Iguassu, Brazil.

[3] Combès, J.F., *"Test Case U3: Centrifugal Pump with a Vaned Diffuser"*, ERCOFTAC Seminar and Workshop on Turbomachinery Flow Prediction VII, Aussois, jan 4-7, 1999.

[4] Ubaldi M., Zunino P., Barigozzi G. and Cattanei A., *"An Experimental Investigation of Stator Induced Unsteadiness on Centrifugal Impeller Outflow",* Journal of Turbomachinery, vol.118, 41-54, 1996.

[5] Combès, J.F., Bert, P.F. and Kueny, J.L., *"Numerical Investigation of the Rotor-Stator Interaction in a Centrifugal Pump Using a Finite Element Method"*, Proceedings of the 1997 ASME Fluids Engineering Division Summer Meeting, FEDSM97-3454, 1997.

[6] Page, M., Théroux, E. and Trépanier, J.-Y., *"Unsteady rotor-stator analysis of a Francis turbine"*, 22nd IAHR Symposium on Hydraulic Machinery and Systems, June 29 – July 2, 2004, Stockholm, Sweden.

[7] Jasak, H., *"Dynamic Mesh Handling in OpenFOAM"*, 47th AIAA Aerospace Sciences Meeting Including the New Horizons Forum and Aerospace Exposition, 5-8 January, Orlando, Florida, 2008 (AIAA 2009-341).

[8] Beaudoin M. and Jasak H., *"Development of a Generalized Grid Interface for Turbomachinery simulations with OpenFOAM"*, Open Source CFD International Conference 2008.

[9] Sutherland I.E. and Hodgman G.W., *"Reentrant polygon clipping*", Communication of the ACM, vol.17, Number 1, 32-42, 1974.

Paper II

Comparison of Numerical and Experimental Results of the Flow in the U9 Kaplan Turbine Model

By

O. Petit, B. Mulu, H. Nilsson and M. Cervantes

25th IAHR Symposium on Hydraulic Machinery and Systems - Timisoara (2010)

Comparison of numerical and experimental results of the flow in the U9 Kaplan turbine model

O Petit[1], B Mulu[2], H Nilsson[1] and M Cervantes[2]

[1]Division of Fluid Mechanics, Chalmers University of Technology, Hörsalsvägen 7A, SE-41296 Göteborg, Sweden
[2]Division of Fluid Mechanics, Luleå University of Technology, SE-971 87 Luleå, Sweden

E-mail: olivierp@chalmers.se

Abstract. The present work compares simulations made using the OpenFOAM CFD code with experimental measurements of the flow in the U9 Kaplan turbine model. Comparisons of the velocity profiles in the spiral casing and in the draft tube are presented. The U9 Kaplan turbine prototype located in Porjus and its model, located in Älvkarleby, Sweden, have curved inlet pipes that lead the flow to the spiral casing. Nowadays, this curved pipe and its effect on the flow in the turbine is not taken into account when numerical simulations are performed at design stage. To study the impact of the inlet pipe curvature on the flow in the turbine, and to get a better overview of the flow of the whole system, measurements were made on the 1:3.1 model of the U9 turbine. Previously published measurements were taken at the inlet of the spiral casing and just before the guide vanes, using the laser Doppler anemometry (LDA) technique. In the draft tube, a number of velocity profiles were measured using the LDA techniques. The present work extends the experimental investigation with a horizontal section at the inlet of the draft tube. The experimental results are used to specify the inlet boundary condition for the numerical simulations in the draft tube, and to validate the computational results in both the spiral casing and the draft tube. The numerical simulations were realized using the standard k-ε model and a block-structured hexahedral wall function mesh.

1. Introduction

Harvesting energy from the flow of water has been done for centuries, and it presents many advantages that makes it widely attractive. Hydro power generates nowadays more than 17 % of the total electricity needs in the world. One of the advantages of a hydro power plant compared to other types of plants is its longevity. Many of the existing dams have been operative for the last century, and it seems that they will continue to do so for many more decades. The power plant is of course closely monitored and its health is regularly checked, but if well-built, a dam can last for a long time. However, due to diverse issues, such as cavitation or vibration, parts of the turbine-generator units need to be replaced every two decades or three. During this elapsed time, technology evolves, and so does the turbine design. It is the case for the Porjus hydraulic power plant located in the north of Sweden. First activated in 1915, one of its units called U9 was replaced during the last decade. The main focus of the new U9 Kaplan turbine is to allow research on a real scale turbine, rather than production [1]. Few detailed measurements are made in water turbines. During design phase, overall quantities such as efficiency are usually measured, rather than detailed pressure and velocity profiles. The U9 prototype facilitates such detailed investigations. It is somewhat smaller than the previous unit, and a curved pipe was inserted into the old penstock when assembling the new prototype.

The use of computational fluid dynamics (CFD) in the design and refurbishment process is becoming increasingly popular due to its flexibility, its detailed flow description and cost-effectiveness compared to the model testing usually used in the development of turbines. However, to get a good description of the flow in such large systems, the appropriate simulation parameters need to be set. Hence many models in CFD are calibrated and validated through simpler geometries and flow patterns. Analytical results, as well as experimental databases are often used to compare and validate simulations. The aim of the U9 project is to create a database of pressure and velocity patterns that can be use to validate CFD simulations, and to investigate the

impact of the curved pipe on the flow in the U9 turbine [10]. The measurements are performed on a 1:3.1 scale Kaplan turbine model. The database is constituted of three different operative conditions: peak efficiency and two off-design points.

Accurate CFD results provide a good understanding of the flow in the turbine, and due to technological improvements, increase of RAM memory and CPU's speed for example, the whole water turbine can now be computed. However, studying such a system requires to do simulations on many computers, in parallel. This can become costly when commercial softwares are used. The alternative that was chosen in this work is OpenFOAM, which is an OpenSource CFD tool written in C++. Previous comparisons [2], [3], and [4] show that it is a competitive and high quality tool that gives similar results as commercial softwares.

This work presents comparisons between experimental and numerical results, in the U9 spiral casing and draft tube. In this work, the comparisons are limited to one working point, the best efficiency point (BEP), and limited to the velocity profiles.

2. Test rig and experimental setup

The measurements were performed at Vattenfall Research and Developmen test facility (VRD) [11]. Detailed velocity measurements were performed and reported by Mulu and Cervantes [5, 6], and pressure measurements by Jonsson and Cervantes [7]. The purpose of those measurements was to investigate the effect of the curved inlet pipe on the flow, and to generate a database for future numerical simulations, at the spiral casing inlet and in the spiral casing before the wicket gates.

2.1. Measurements in the U9 spiral casing

The test rig used to do the measurements is located at the Vattenfall Research and Development (VRD) model test facility in Älvkarleby, Sweden. It is a closed loop system where the absolute pressure in the downstream tank can be regulated to control the presence of cavitations. It is a 1:3.1 scale model of the U9 prototype. The best efficiency point corresponds to a guide vane angle of 26 degrees, and a discharge of 0.71 m^3/s. An overview of the test rig is given in Fig.1 where the curved inlet pipe can be observed.

The inlet of the U9 model spiral casing is a circular pipe with an inner radius of 316 mm. A plexiglas pipe 290 mm long was mounted between the inlet of the spiral casing, see Fig. 1. To avoid refraction caused by the surface curvature of the inlet pipe, a square optical box, filled with index matching liquid was placed around the pipe [5]. LDA measurements were performed from both sides of the pipe, along five horizontal and one vertical axis, as shown in Fig. 1.
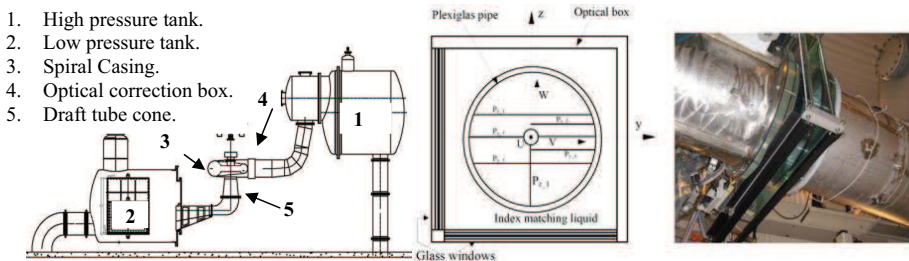
1. High pressure tank.
2. Low pressure tank.
3. Spiral Casing.
4. Optical correction box.
5. Draft tube cone.

Fig. 1: Test rig of the U9 Kaplan turbine model (left), inlet section of the spiral casing and locations of the measured velocity profiles in the circular section (centre, right).

In the spiral casing, two windows were installed at the bottom, at the angular positions -56.25 degrees, (SI) and -236.25 degrees (SII) to perform LDA measurements, as shown in Fig. 2. The windows were placed at the centre of the casing. The LDA measurements were easier to perform than at the inlet, as the windows are planar, and thus do not cause any refraction problem, and do not need any correction.
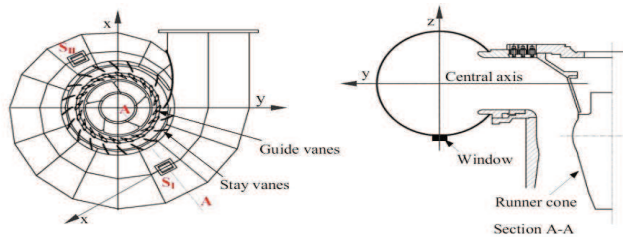
Fig. 2: Location of the windows in the spiral casing (left) and of the measurement axis z (right).

2.2. Measurements in the U9 draft tube

The draft tube velocity measurements were performed in the cone. To create a detailed database, four windows were mounted, with angular positions (AP) of 0, 90, 180 and 270 degrees, as shown in Fig. 3. Two types of measurements were performed. To create a inlet boundary condition for the numerical simulations, the axial and tangential velocity profiles were measured along section P at window a (0°), and d (270°). The velocity profiles are orthogonal to the draft tube cone axis, see Fig. 3. An average of both profiles was used as inlet boundary conditions for the draft tube simulations. To provide with a detailed database and validate the simulations, velocity measurements were also performed at sections I, II and III for the four different angular positions. For these measurements, the axis of the probe is orthogonal to the window and has an angle of 96.1° with the draft tube cone axis. Therefore, the tangential velocity is effectively measured while part of the axial and radial velocity is obtained for the other component. However, the snal cone angle (α=6.1°) combined with a probably negligible radial velocity (U_{radial}) allow to assume the measured velocity ($U_{measured}$) as axial velocity (U_{axial}). The error is estimated to be below 1%.

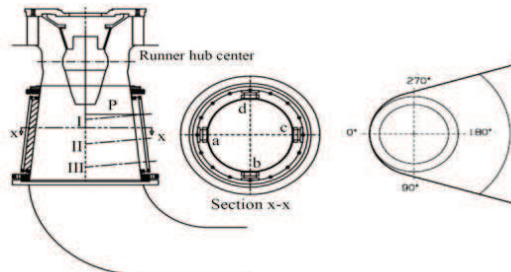$$U_{measured} = U_{axial} \cos(\alpha) + U_{radial} \sin(\alpha) \approx U_{axial}$$

Fig. 3: Window locations at the draft tube cone: a is at 0°, b at 90 °, c at 180°, and d at 270°. P represents the velocity section measured for the inlet boundary condition for numerical simulations, and sections I, II and III for the validation.

2.3. Operating conditions

The measurements have been carried out at three different loads, at best operating point of the turbine and at two off-design operating points (to the left and right of the propeller curve). The operational net head H=7.5 m, the runner blade angle β=0.8°, and a runner speed N=696.3 rpm were used throughout the entire period of measurements. The working guide vane angle and the volume flow rate of the three working conditions are summarized in Table. 1. The results presented in this paper are at the best efficiency point.

Operating point	Left	BEP	Right
Guide vane angle (α) in degree	20	26	32
Volume flow rate Q (m³/s)	0.62	0.71	0.76

Table. 1: Operational condition parameters.

3. Computational domain and OpenFOAM setup

3.1. Spiral casing computational domain and setup

The spiral casing computational domain starts with the high-pressure tank and includes the curved inlet pipe, the spiral casing as well as the wicket gate, see Fig. 4. The domain was realized in ICEM Hexa, and is divided in four different parts: part of the inlet tank, the inlet curved pipe, the spiral casing, and the wicket gate. Only the inlet tank is included in the computational domain, as a honeycomb is installed at the inlet of this tank, so that the velocity at the inlet is considered constant. Those four different parts are coupled in OpenFOAM using the General Grid Interface (GGI) developed by Beaudoin and Jasak [8]. The mesh is fully hexahedral, and consists of 5 million cells. The steady-state incompressible Reynolds-Averaged Navier-Stokes equations are solved, using the finite volume method and the standard k-ε model closure. At the walls the log-law treatment is applied and the average y+ values range between 50-100. The boundary condition at the inlet is a plug flow with the nominal discharge 0.71 m^3/s. The turbulent kinetic energy is calculated so that the turbulent intensity is 10%, and the turbulence dissipation is chosen so that v_T/v=10. At the outlet, a mean pressure of 0 is set. A second-order upwind scheme is set for the convection, while the first-order upwind scheme is used for the turbulence parameters.

3.2. U9 draft tube computational domain and setup

The draft tube mesh is fully hexahedral, and consists of 1.1 million cells. The draft tube computational domain is shown in Fig. 5. The same numerical set-up as in the spiral casing is used. The inlet boundary condition for velocity and turbulence is given by the measurements at section P, see Fig. 3 and Fig. 6.
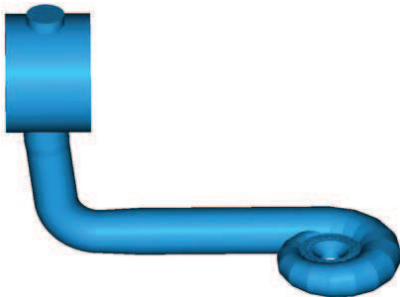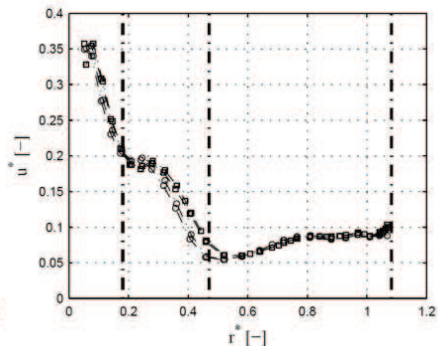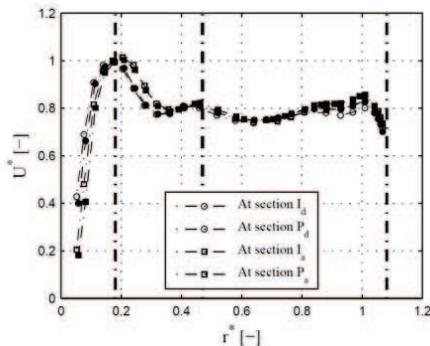

Fig. 4: Computational domain of the U9 spiral casing.

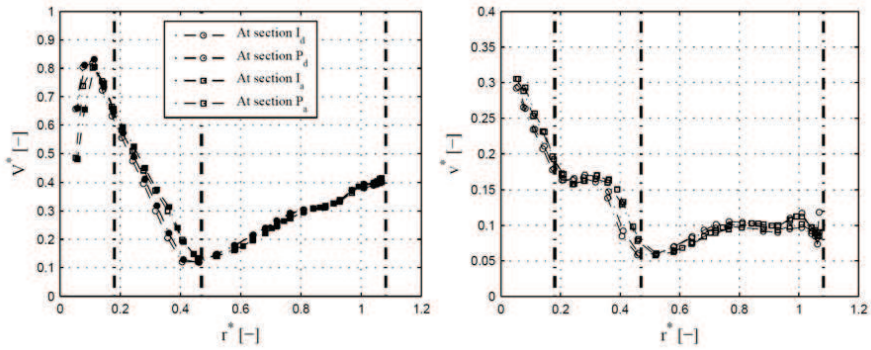**Fig. 5**: Computational domain of the U9 draft tube.

Fig. 6: Measured axial (U*) and tangential (V*) velocity profiles at sections P and I. The profiles on the right hand side represent the corresponding measured RMS for the axial (u*) and tangential (v*) velocities.

4. Results

An overview of the flow in the spiral casing and draft tube is shown in Figs. 7, 8, 9, and 10. The importance of including the curved pipe in the computational domain is shown in Fig.7, and the recirculation is still visible at the inlet of the spiral casing, in Fig. 8. The accuracy of the recirculation prediction in the numerical results is strongly dependent on the choice of the turbulence model that is made, as well as the choice of boundary condition at the wall. Detached-eddy Simulation (DES) should predict the length of the detached boundary layer, and hence the recirculation, much better than the k-ε model. That will be done in future work.

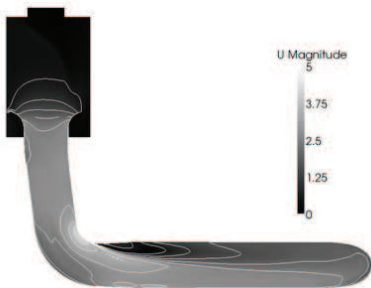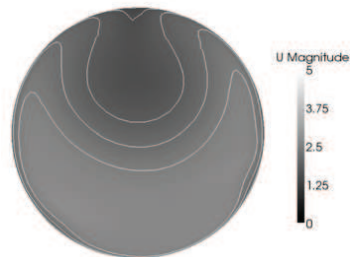**Fig. 7**: Velocity magnitude in the inlet pipe.

Fig. 8: Velocity magnitude at the spiral casing inlet measurement section.
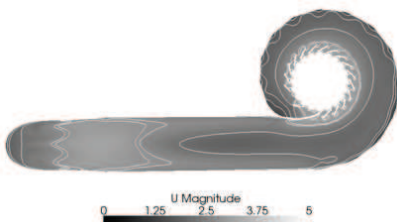

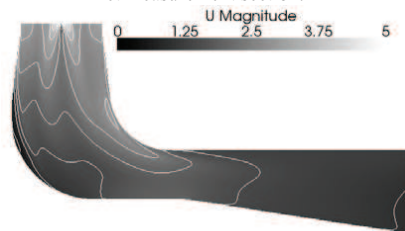**Fig. 9**: Velocity magnitude in the spiral casing.

Fig.10: Velocity magnitude in the draft tube.

4.1. Results in the spiral casing

At the inlet of the spiral casing, the experimental axial velocity profiles at Py_1, Py_5 and Pz, specified in Fig. 1, are compared with the numerical results in Fig.11. The analysed data are presented in dimensionless form using, R_{inlet}=0.316m, and v_{inlet}=$Q/\pi \cdot R^2_{inlet}$, Q=0.71 m^3.s^{-1}. The flow predicted by OpenFOAM shows a similar behaviour as the measured flow. The axial velocity at Py_1 is lower than that at profile Py_5. The M-shape character in the velocity distribution is due to the pair of counterrotating Dean vortices, which is known in a circular bend flow [12]. Since the axial velocity distribution is not uniform in the plane due to lower velocity close to the upper wall, fluid particles with higher velocity are forced to move to the outer side, and those with lower velocity to the centre. This is due to the curvature which causes a positive gradient of the centrifugal force from the centre to the outer wall. This force and the presence of a boundary layer at the wall due to the fluid adhesion to the wall combined are responsible for this kind of flow behaviour [12].

The difference between the prediction of OpenFOAM and the measured flow can be explained by the fact that the simulations use a basic k-ε model that does not fully predict the flow in the recirculation region after the bend, shown in Fig. 7. At profile P_z, which is at the center line of the pipe, the numerical results show good agreement with the experimental values.
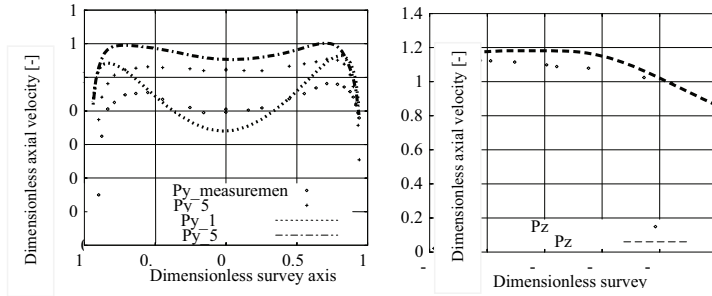
Fig.11: Axial velocity profiles at profile Py_1 and Py_5 (left), and Pz (right).

The comparison inside the spiral casing is done at the two positions (SI and SII) described in Fig. 2. Axial and tangential velocity profiles are shown in
Fig**.** 12. The reference point is located at the lower wall of the spiral casing.
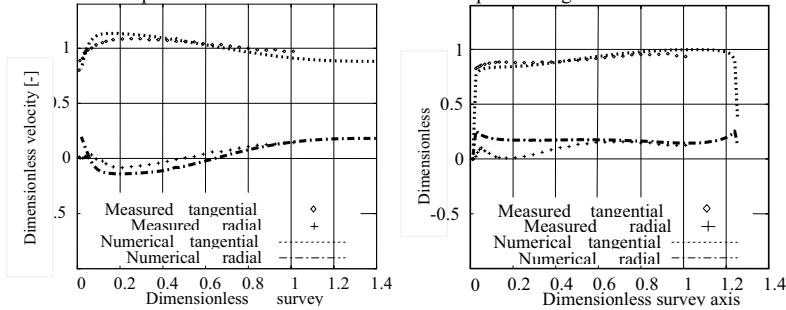
Fig.12: Dimensionless radial and tangential velocity at SI (left) and SII (right), inside the spiral casing.

In this comparison, the radial velocity is defined as positive toward the centre. The radial velocity measured at location SI shows the presence of a secondary flow yielding negative radial velocities. This secondary flow is not observed at location SII. The numerical prediction of the flow inside the spiral casing is accurate, though it tends to yield a slighlty different radial velocity distribution than the experimental measurements at Section I, which may be a consequence of the flow prediction in the bend.

4.2. Results in the draft tube

In the draft tube, comparisons of the numerically predicted flow and the measurements are made in two different windows, a and c (see Fig. 3). The results are presented in Fig.13. The reference point for this comparison is at the centreline of the draft tube, and the survey axis is normalized by the radius of the runner, R_{Runner}=0.25m. Close to the inlet of the draft tube, the predicted flow is similar to the measured flow. However, the difference at the centre of the draft tube is already visible. The numerical simulation does not predict the flow features very well in the draft tube, and the more downstream it goes, the less accurate the results become. The reason to this unaccuracy is the inlet boundary condition. The velocity profile set at the inlet of the draft tube is an average value of the flow measured at window a and d at section SI. That means that we set a symmetric swirling flow at the inlet. In reality, the swirl flow is asymmetric as wakes are coming down from the runner. Furthermore, close to the centre (0-13 mm), the axial and tangential velocities were approximated since no experimental data were available, see Fig. 6. It is further questionable to specify a steady axi-symmetric inlet boundary condition in a region of high unsteadiness and non-axi-symmetry. Finally, it was shown at the Turbine-99 workshop [9] that ignoring the radial velocity profile at the draft tube inlet when setting the boundary condition leads to a wrong prediction of the flow in the draft tube. In the present work, the inlet boundary condition is much below than for the Turbine-99 test case. The radial velocity measurements were not available, and thus neglected. Close to the wall, however, the flow is rather well predicted, both for the elbow window (window c) and for the window a. This is promising, and a more precise inlet boundary condition should result in an accurate prediction of the flow. However, for accurate results, the runner must be included in the simulation. That will be done in future work.
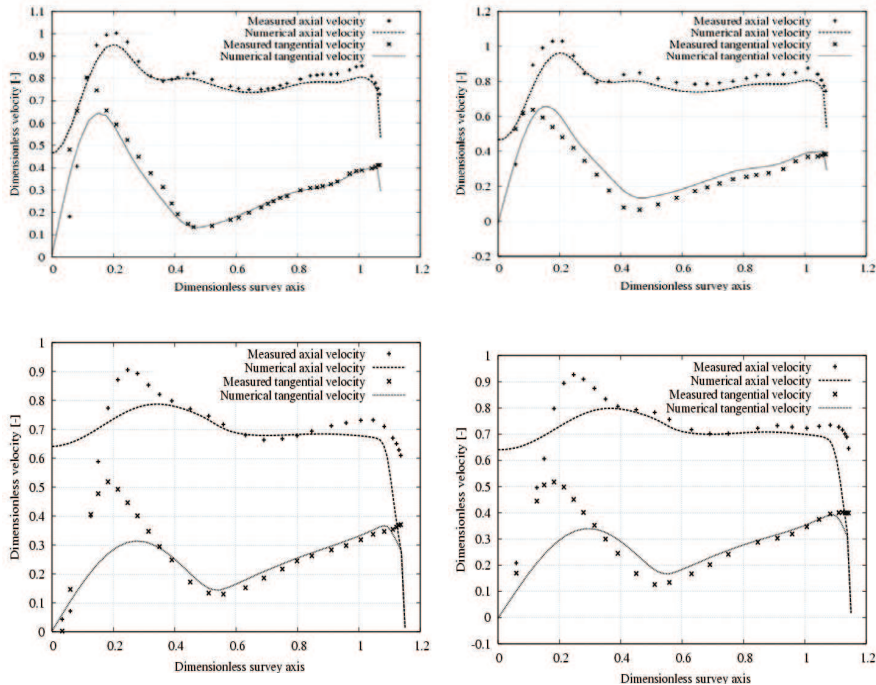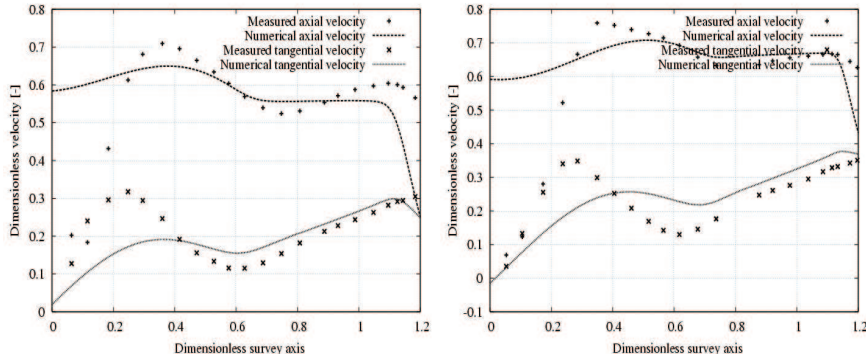
Fig.13: Velocity profiles for sections Ia (top left), Ic (top right), IIa (middle left), IIc (middle right), IIIa (down left), and IIIc (down right).

Conclusion

Comparisons between numerical simulations and experimental results in the U9 spiral casing and draft tube have been presented. The results show the importance of setting appropriate boundary conditions when numerically trying to predict the flow in water turbines.

In the spiral casing, the comparison shows the effect a curved pipe has on the spiral casing inlet flow. In the draft-tube, the importance of defining an appropriate inlet boundary condition is the key to succesfully predict the flow features of the draft tube. However, to predict the flow as accurately as possible, it is important to couple the runner with the draft tube, and to compute unsteady simulation.

The numerical simulations predict the overall flow features in the spiral casing and in the draft tube rather well. The predicted flow is similar to the measured flow, and this work sets the base for future investigations. Future work in the U9 project is the investigation of more accurate turbulence models in the spiral casing, in order to accurately predict the turbulent flow features. In the draft tube, an estimation of the radial velocity should get a better flow prediction. Ultimately, unsteady simulations of the U9 Kaplan turbine coupled with the draft tube using a sliding grid should predict a very accurate flow.

Acknowledgement

References

[1]   Cervantes M J, Jansson I, Jourak A, Glavatskikh G and Aidanpää J O 2008 Porjus U9, A Full-Scale Hydropower Research Facility *Proc. of the 24th IAHR Symp. on Hydraulic Machinery and Systems* (Foz Do Iguassu, Brazil)

[2]   Petit O, Nilsson H, Vu T, Manole O and Leonsson S 2008 The Flow in the U9 Kaplan Turbine - Preliminary and Planned Simulations Using CFX and OpenFOAM *Proc. of the 24th IAHR Symp. on Hydraulic Machinery and Systems* (Foz de Iguassu, Brazil)

[3]   Nilsson H and Page M 2005 OpenFOAM simulation of the flow in the Hölleforsen draft tube model *Proc. of the 3rd IAHR/ERCOFTAC Workshop on draft tube flows* (Porjus, Sweden)

[4]   Muntean S, Nilsson H and Susan-Resiga R 2009 3D Numerical Analysis of the Unsteady Turbulent Swirling Flow in a Conical Diffuser Using Fluent and OpenFOAM *3rd IAHR Int. Meetings of the Workshop on Cavitation and Dynamic Problems in Hydraulic Machinery and Systems* (Brno, Czech Republic) p C4

[5]   Mulu B 2009 *Experimental and Numerical Investigation of Axial Turbine Models* (Licenciate Thesis Luleå

University of technology, Sweden)

[6]   Mulu B and Cervantes M 2009 Experimental Investigation of a Kaplan Model with LDA *33rd IAHR Congress Water Engineering for a Sustainable Environment*

[7]   Jonsson P and Cervantes M *Time Resolved Pressure Measurements on a Kaplan Model*

[8]   Beaudoin M and Jasak H 2008 Development of a Generalized Grid Interface for Turbomachinery simulations with OpenFOAM *OpenSource CFD International Conference* (Berlin, Germany)

[9]   Cervantes M, Gustavsson L, Page M and Engström F 2006 Turbine-99, a summary *23rd IAHR Symp.* (Yokohama, Japan)

[10] Mulu B and Cervantes M 2007 Effects of Inlet Boundary Conditions on Spiral Casing Simulations Proc. of the 2nd IAHR Int. Meeting of the Workgroup on Cavitation and Dynamic Problems in Hydraulic Machinery and Systems, (Timisoara, Romania) (*Scientific Bulletin of the "Politehnica" University of Timisoara Transactions on Mechanics, Tom 52(66), Fascicola 6*)

[11] Marcinkiewics J and Svensson S 1994 Modification of the Spiral Casing Geometry in the Neighbourhood of the Guide Vanes and its influence on the Efficiency of a Kaplan Turbine *Proc. of the 17th IAHR Meetings on hydraulic machinery and cavitation* Vol. 1 pp 429-434

[12] Boiron O, Deplano V and Pelissier R 2007 Experimental and Numerical Studies on the Starting Effect on the Secondary Flow in a Bend *J. Fluid Mech.* **574** 109-209

Paper III

Unsteady Simulations of the Flow in a Swirl Generator, Using OpenFOAM

By

O. Petit, A.I. Bosioc, H. Nilsson, S. Muntean and R.F.Susan-Resiga

Original Paper (Invited)

Unsteady Simulations of the Flow in a Swirl Generator, Using OpenFOAM

Olivier Petit[1], Alin I. Bosioc[2], Håkan Nilsson[1], Sebastian Muntean[3], Romeo F.Susan-Resiga[2]

[1]Division of Fluid Mechanics, Chalmers University of Technology
Hörsalsvägen 7A, SE-41296 Göteborg, Sweden
olivierp@chalmers.se, hani@chalmers.se
[2]Department of Hydraulic Machinery, "Politehnica" University of Timisoara
Bv. Mihai Viteazu 1, RO 300222, Timisoara, Romania
alin@mh.mec.upt.ro, resiga@mh.mec.upt.ro
[3] Centre of Advanced Research in Engineering Sciences, Romanian Academy – Timişoara Branch
Bv. Mihai Viteazu 24, RO-300223, Timişoara, Romania seby@acad-tim.tm.edu.ro

Abstract

This work presents numerical results, using OpenFOAM, of the flow in the swirl flow generator test rig developed at Politehnica University of Timisoara, Romania. The work shows results computed by solving the unsteady Reynolds Averaged Navier Stokes equations. The unsteady method couples the rotating and stationary parts using a sliding grid interface based on a GGI formulation. Turbulence is modeled using the standard k-ε model, and block structured wall function ICEM-Hexa meshes are used. The numerical results are validated against experimental LDV results, and against design velocity profiles. The investigation shows that OpenFOAM gives results that are comparable to the experimental and design profiles. The unsteady pressure fluctuations at four different positions in the draft tube is recorded. A Fourier analysis of the numerical results is compared whit that of the experimental values. The amplitude and frequency predicted by the numerical simulation are comparable to those given by the experimental results, though slightly over estimated.

Keywords: Swirl generator, OpenFOAM, CFD, Validation, Runner, Draft tube, Rotor-Stator Interaction.

1. Introduction

Nowadays, due to the variable demand of the energy market and new intermittent energy sources, a new parameter is often important for water power: flexibility. Water turbines now operate over an extended range of regimes that can be quite far from the best efficiency point. The runner is designed so that the swirl generated by the guide vanes is more or less neutralized by the runner at the best efficiency point. However, at part load operation (away from the efficiency point), a strong swirling flow exits the runner. This is called a vortex rope. This phenomenon leads to large periodic pressure fluctuations that increase the risk of fatigue.

The importance of predicting such phenomena has lead to many studies. One of those is the Flow Investigation in Draft Tubes (FLINDT) research project [1]. The main objective of the FLINDT project was to investigate such phenomena and to provide an extensive database for a range of different operating points. Such experimental projects are usually complex and measurements are performed on reduced scale models. The team at the Politehnica University of Timisoara (UPT), National Centre for Engineering Systems with Complex Fluids (NCESCF) has developed such a simplified swirl generator to further study the precessing vortex rope [2]. The swirl generator was designed to give a swirl profile similar to that in the FLINDT project. The test rig was developed and manufactured in order to provide a good visualization of the phenomenon, as well as to investigate the velocity field of the swirling flow [3, 4]. The stay vanes and runner blades were designed using the inverse design methodology [15] in order to create a precessing vortex rope [5]. One of the purposes of this test rig is to investigate the viability of reducing pressure fluctuation of a precessing vortex rope by axial jet control in the discharge cone. This novel technique was introduced by Susan-Resiga et al. [6] to control the draft tube instability at partial discharge. Measurements on the test rig showed that a 10% jet discharge gives a maximum pressure recovery and creates no pressure fluctuations [7, 17]. This conclusion was asserted by 3D unsteady numerical investigation using Fluent of the swirling flow using jet control [8]. It is nonetheless not acceptable to bypass the runner with such a large fraction of the turbine

discharge. However, Susan-Resiga et al. [9, 16] have also developed a flow feedback approach for supplying the jet without any additional energy.

The simple geometry of the test rig, as well as the quality of the measurements performed by Bosioc et al. [10] makes this a very good case study for turbomachinery applications in OpenFOAM. OpenFOAM is an object oriented OpenSource library written in C++. With regards to basic features, such as turbulence models and discretization schemes, OpenFOAM is a competitive and high quality tool that is constantly evolving. Preliminary simulations were realized on the conical diffuser of the test rig [11], which showed that OpenFOAM gives as accurate results as commercial software.

The community driven OpenFOAM Turbomachinery Working Group [12] develops and validates OpenFOAM for turbomachinery applications. The swirling flow generator was chosen as a case study for the 5th OpenFOAM workshop held in Gothenburg, Sweden, and comparison between numerical results and measurements were presented. The goal of the Turbomachinery Working Group is to release this case study so that anyone who would like to learn OpenFOAM, or become more familiar with turbomachinery features in OpenFOAM, can learn how to set up, compute and analyse such problems.

2. Experimental setup

A cross-section of the test rig is presented in Fig.1. The original test case was presented by Bosioc et al. [10] and was developed at Politehnica University of Timisoara. The swirling flow apparatus consists of four leaned strouts, 13 guide vanes, a free runner with 10 blades and a convergent divergent draft tube [3-5]. The guide vanes create a tangential velocity component, while keeping practically a constant pressure. The purpose of the free runner is to re-distribute the total pressure by inducing an excess in the axial velocity near the shroud and a corresponding deficit near the hub, like a Francis turbine operation at 70% partial discharge. The runner blades act like a turbine near the hub, and a pump near the shroud. Thus the runner spins freely, without any total torque. The design value for the rotation of the runner is 870 rpm, but stroboscope measurement on the test rig gives a slightly higher rotation, 920 rpm.
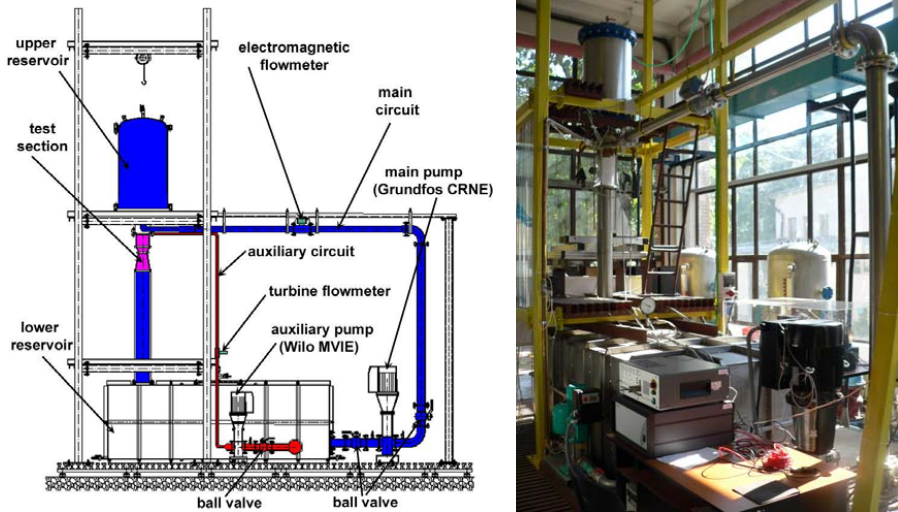

Fig. 1 Closed loop test rig for experimental investigations of swirling flow installed at Politehnica University of Timisoara.

The test rig consists in a main circuit, used to supply the swirling flow section, and an auxiliary circuit that is used when tests are performed using axial jet control (see Fig.1). The main centrifugal pump that provides the flow has a variable speed delivering up to 35 l/s. The swirling flow test section is made of plexiglass, so that visual observation is possible and to facilitate optical measurements. The measurements were performed at Politehnica University of Timisoara and were first presented by Bosioc et al. [10].

2.1 Velocity measurements

The experimental data was measured with the help of two-component Laser-Doppler Velocimetry (LDV). 10 μm aluminum particles were used to reflect the laser beam. The velocity measurements were realized in three different optical windows, the first located in the convergent part of the simplified draft tube, and the other two located in the axi-symmetric diffuser (see Fig. 2). The reference for the survey axis is set at the wall, as shown by the arrows in Fig. 1. On survey axis 0, 31 points were measured, while survey axis 1 contains 113 points, and survey axis 2 contains 141 points. The flow rate was kept at 80% of the maximum power of the pump, that is 30 l/s. The rotational speed of the free runner was 920 rpm. In order to get a time-averaged velocity profile, each point was sampled for a period of 25 seconds (5000 samples). A dimensionless form was used in the analysis of the velocity profiles, normalizing the abscissa by R_{Throat}=0.05m, and the velocity profiles by

$$v_{Throat} = \frac{Q}{\pi R_{Throat}^2}, \ Q=30 \ \text{l/s}.$$

For clarity, in the following discussion, the first survey axis is called **W0,** the second survey axis is called **W1** and the third one **W2**.
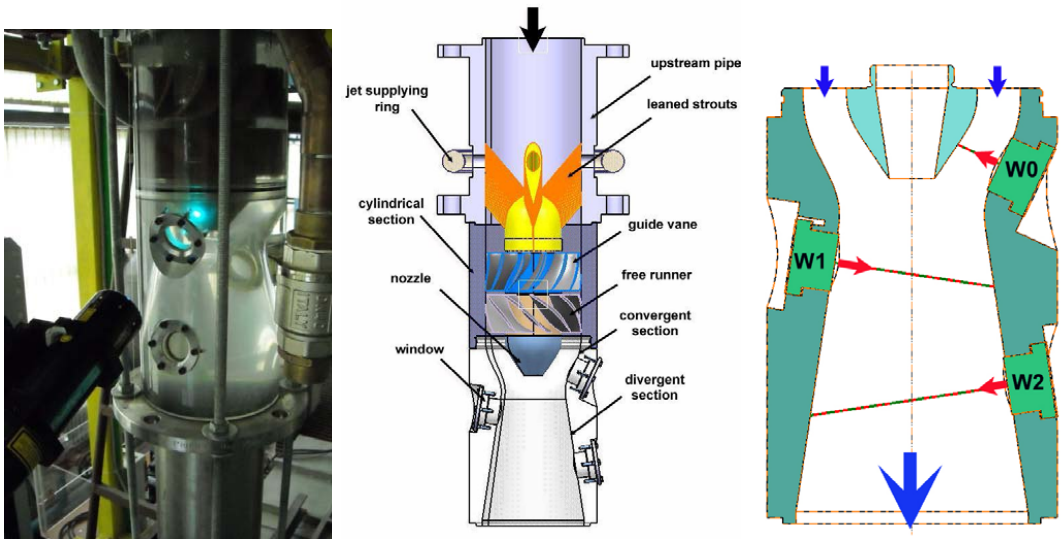
Fig. 2 Test section for LDV measurements of swirling flow: test section photography (left), cross section of the swirling apparatus in order to measure velocity profiles (centre), survey axes for all three windows (W0, W1 and W2) (right).

2.2 Unsteady pressure measurements

The unsteady static pressure is measured at four positions (MG0, MG1, MG2 and MG3) with the help of Cole-Parmer unsteady pressure transducers. The capacitive pressure transducers have an accuracy of 0.13% within a range of ±1 bar relative pressure. When the water is at rest, all pressure transducers are aligned with respect to the static head. For the investigations reported in this paper we are interested in the pressure fluctuations, in order to assess the amplitude and the frequency for the vortex rope from the conical diffuser. Eight of the latter are flush mounted on the cone wall at four levers (see Fig. 3). The sections are located at 0, 50, 100 and 150 mm downstream to the throat. In order to obtain reliable pressure data we measure 100 sets for each discharge value. Each set is acquired using a Lab View program, and corresponds to an acquisition time of 32 seconds at a sampling rate of 256 samples/second, resulting in 8192 samples of unsteady pressure.
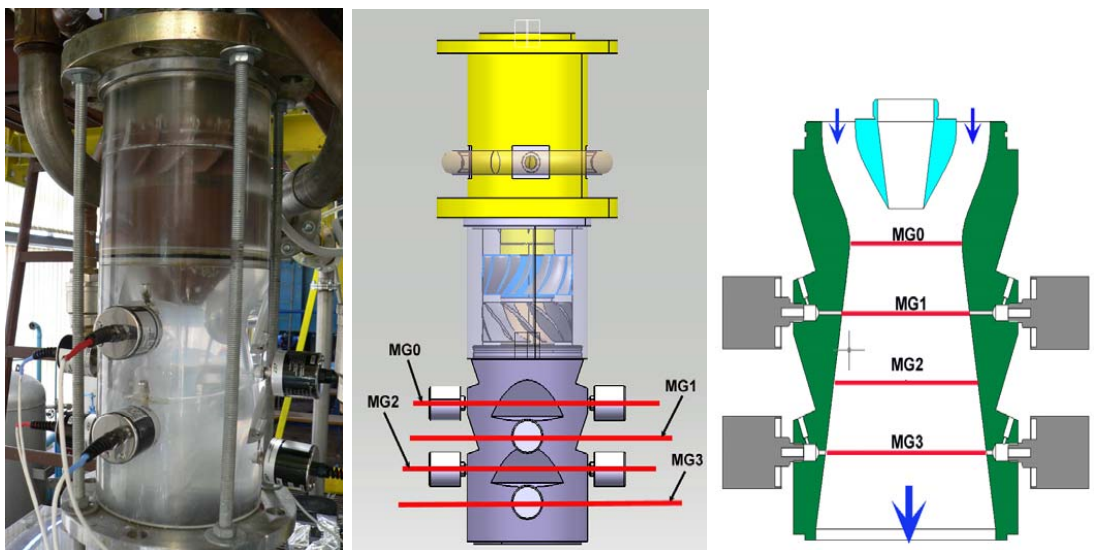
Fig. 3 Test rig section for unsteady experimental investigations of swirling flow: test section photography (left), unsteady pressure measured on four levels (MG0, MG1, MG2 and MG3) (middle and right).

3. Computational domains and OpenFOAM numerical set-up

The computational domain consists of the whole test rig shown in Figs. 2 and 3. The mesh was generated in ICEM-Hexa, and consists of four different parts (see Fig. 4): the leaned strouts, the guide vanes, the free runner and the draft tube. The four different parts are coupled in OpenFOAM using the General Grid Interface (GGI), developed by Beaudoin and Jasak [13]. The

mesh is fully hexahedral, and consists of 2.8 million cells. At the walls, the log-law treatment is applied, and the average y+ values range between 50-200.

Fig. 4 Half of meridional cross-section of the swirling flow apparatus (above)
and associated computational domains and grids (below).

Two different computational techniques were used to predict the flow in the swirling flow test rig:

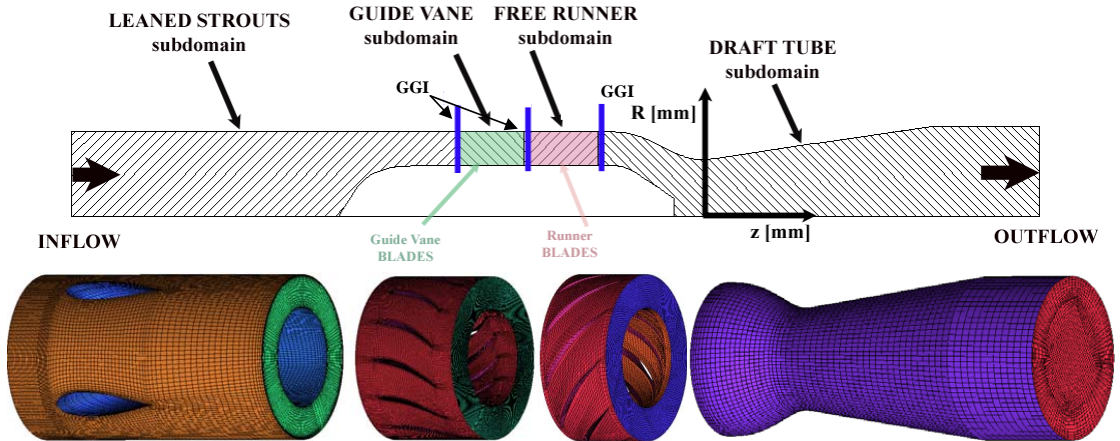- The first method is a steady-state method, solving the steady Reynolds Averaged Navier Stokes equations. Because of the rotor-stator interaction in this case study, a frozen rotor solver is used. It is a steady state formulation where the rotor and stator are fixed with respect to each other, and different reference frames are used in the rotating and stationary parts. Though this method does not predict the flow features behind the runner accurately, it is a fast preliminary method and the general behavior of the flow is predicted. This method is here only used to create an initial solution for the transient method.

- The sliding grid approach is a transient method where the runner mesh actually rotates with respect to the stator mesh. The URANS equations are solved and most of the unsteady flow features are predicted. However, due to the extra dimension added to the resolution (time), the simulation is time and computer resources consuming. The interaction between the rotor and stator is realized with the help of a sliding General Grid Interface [13]. The boundary condition at the inlet is a plug-flow with the nominal discharge 30 l/s. The turbulence kinetic energy is set to 0.1, and the dissipation to 90, so that the turbulence intensity is of the order of 10% and the viscosity ratio $v_T/v=10$. The velocity and turbulence equations use the homogeneous Neumann boundary condition at the outlet. The pressure equation uses a homogeneous Neumann boundary condition at all boundaries, and at the outlet the mean pressure is set to zero. The convection terms are discretized using a second-order linear-upwind scheme, and the time terms are discretized using a second-order backward scheme. The rotation speed of the runner is given by the experimentally measured rotation speed, 920 rpm. The time step used to compute this case is $2.35 \ 10^{-4}$ s, yielding a maximum Courant number of 5, and a mean Courant number of 0.2. This time step gives an angle of rotation equal to 1.3° per time step.

It was shown in previous studies [14] that the prediction of the flow features by the steady-state method is not accurate enough. Thus the initial condition of the unsteady simulation is generated by the steady simulation, but the present work is focusing only on the unsteady results. A comparison of those results with experimental and design velocity profiles is shown, as well as a Fourier analysis of the pressure fluctuations.

4. Comparison of numerical results against experimental and design data

4.1 Design and computed velocity profiles

The comparison between the design velocity profiles [5] and the OpenFOAM results is realized at Section 1 (S1) and Section 2 (S2) shown in Fig. 5. Section 1 is downstream the guide vanes, and section 2 is downstream the free runner. The dimensionless velocity profiles are plotted in Fig.6 and 7 against the radius of the different sections, divided by R_{throat}. The results computed by OpenFOAM, are time averaged. The two design velocity profiles at sections S1 and S2 were designed to give a specific swirling flow downstream in the draft tube. At section S1, the swirl created by the guide vanes should have a free-vortex configuration, with quasi-constant axial velocity. The numerical results obtained with OpenFOAM are in relatively good agreement with the design profile, see Fig. 6. The axial velocity is in very good agreement in both sections, which shows that the volume flow used in the OpenFOAM simulation is the same as that of the inviscid design theory. However, the numerical simulation over-estimates the tangential velocity at section S2, located below the runner. The design value of the rotation speed of the free runner was 870 rpm. Nevertheless, after the construction of the test rig, the experimentally measured rotation speed of the runner turned to be equal to 920 rpm, slightly higher than the intended design value. The rotation speed in numerical simulation is 920 rpm. This is why the tangential velocity obtained in the simulation is higher than the tangential velocity for the inviscid design. Complementary studies with the help of OpenFOAM [18] has shown that if the rotation speed of the free runner is lowered to the value given by the inviscid design, the tangential velocity obtained with OpenFOAM corresponds to that of the inviscid theory.
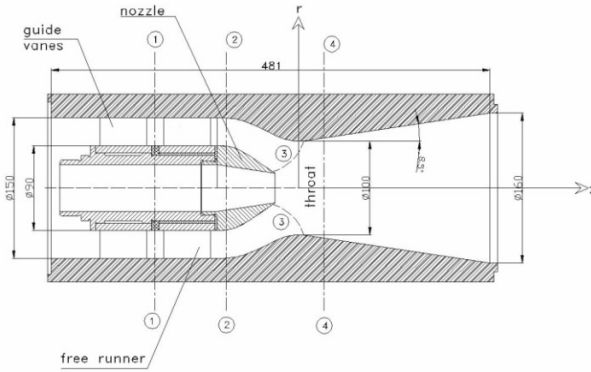
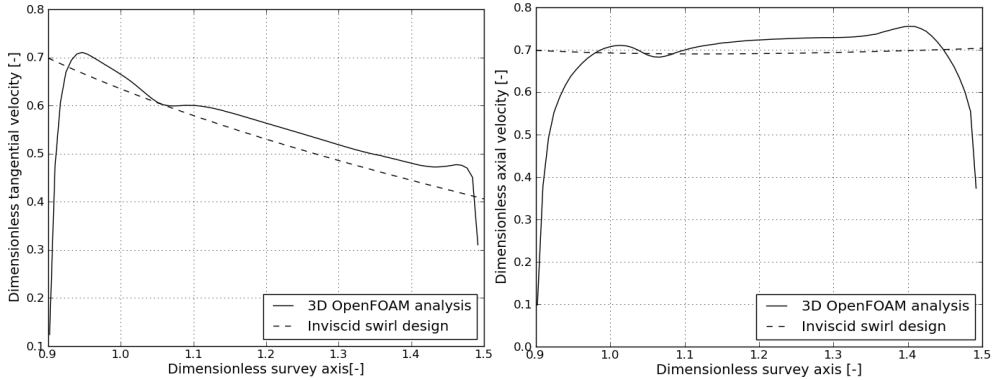**Fig. 5** Cross-section of the swirling flow apparatus and the four survey axes.

Fig. 6 Tangential (left) and axial (right) velocity profiles at section S1, displaced between guide vanes and free runner (Fig. 5).
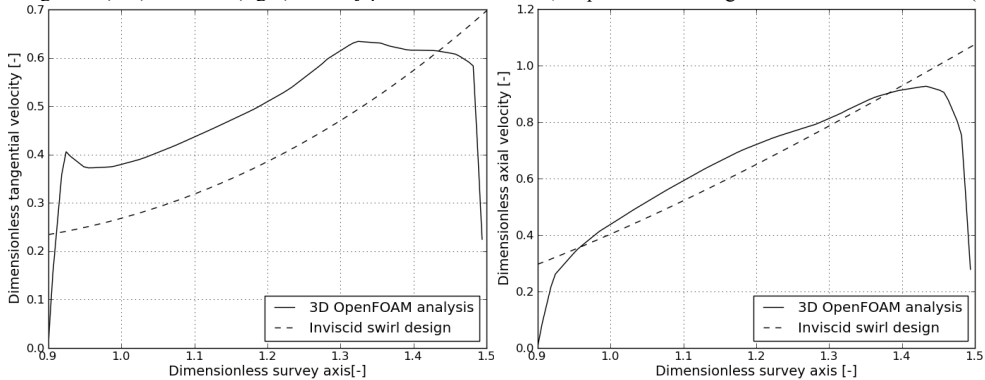

Fig. 7 Tangential (left) and axial (right) velocity profiles at S2, displaced just downstream to the free runner (Fig. 5).

4.2 Experimental and computed velocity profiles in test the section

The comparisons between the velocity profiles numerically predicted with OpenFOAM, and the experimental data are shown in Fig. 8. The computed velocity profiles are time averaged. At section W0, the velocity computed by OpenFOAM shows very good agreement with that of the experiment. However, the computed tangential velocity is a bit under-predicted. The slight underestimation of the tangential has an impact on the meridional velocity at sections W1 and W2. Since the tangential velocity is not as large as it should be, more flow is pushed close to the walls, and less in the centre line. It can be seen that the stagnation region predicted by the measurements is becoming a recirculation region for the computed flow, with a small negative meridional velocity.

As shown in Fig. 8, the wakes of the 10 runner blades can still be seen at window W0, and the region of the precessing vortex rope, with a zero or negative tangential velocity can be seen at window W1 and W2. The unsteady simulation predicts the periodic fluctuations in the draft tube rather well, and a visualization of the computed vortex rope is shown in Fig. 9. Due to the time resolution of the sliding grid model, the visualization of the vortex rope oscillation can be done. Fig. 9 also shows the same vortex rope visualized in the experiments.
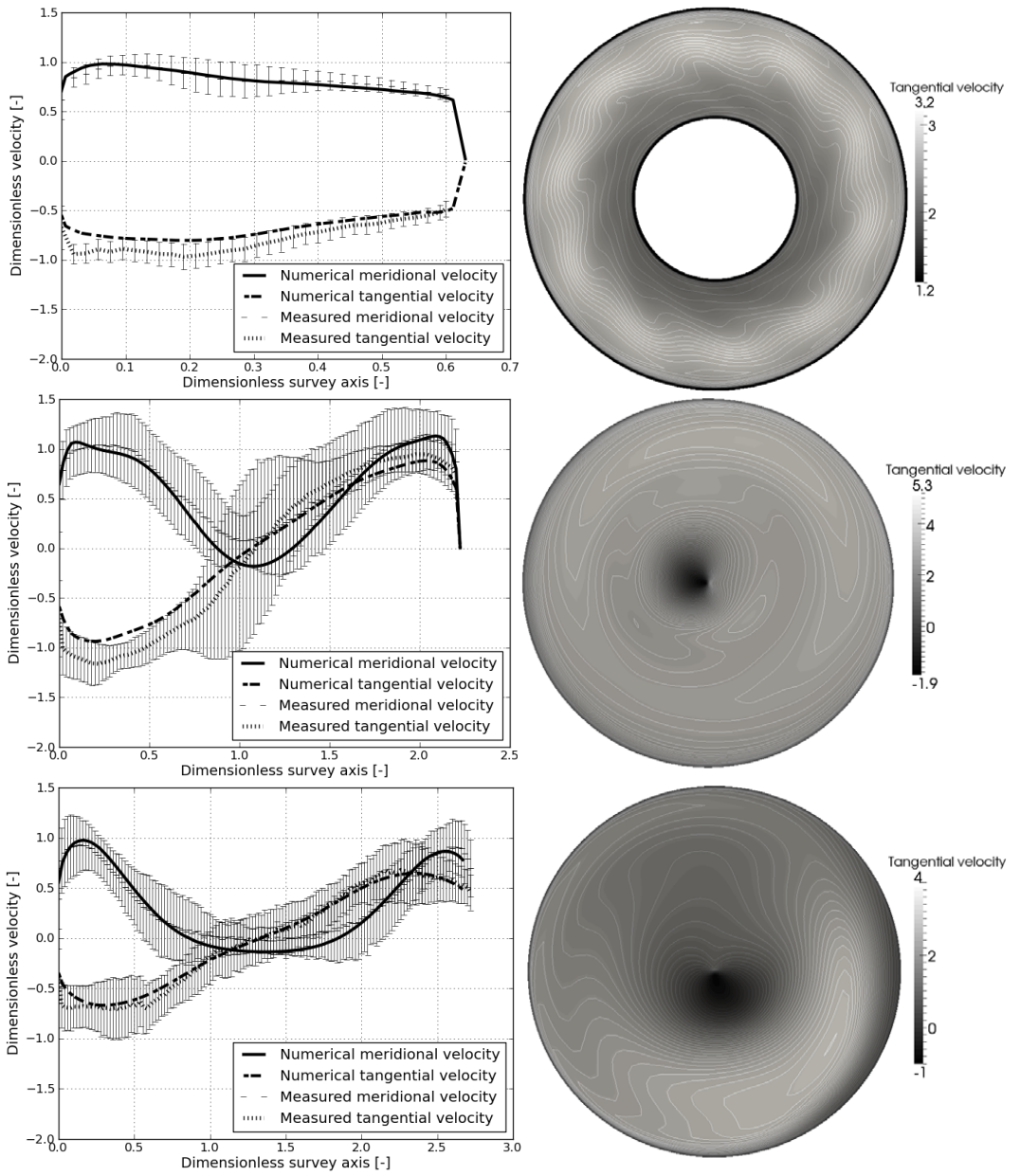
Fig. 8 Time-averaged velocity profiles (left), and instantaneous tangential velocity (right) at W0, W1, W2 (top to bottom).
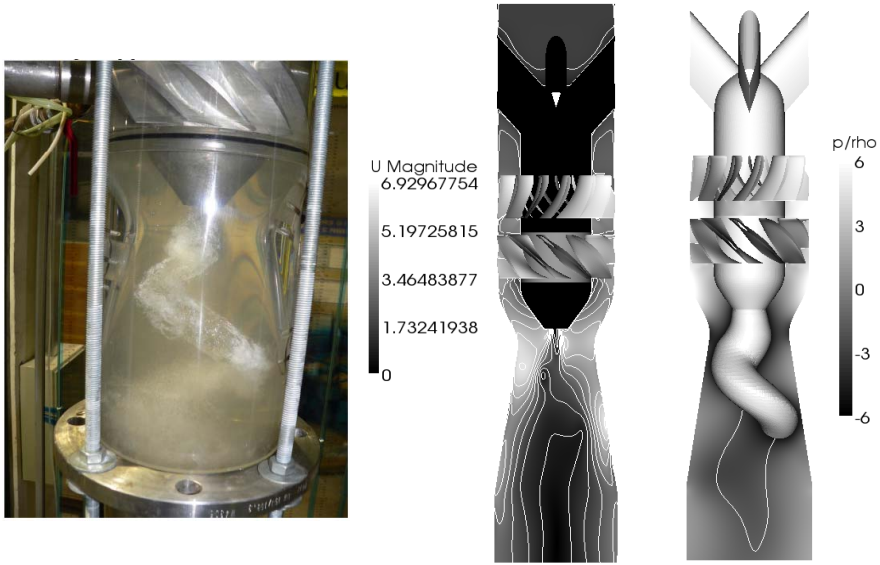
Fig. 9 The precessing vortex rope visualized in the experimental test section (left), and snap-shots of the velocity (centre) and pressure field (right) predicted by the numerical simulations in OpenFOAM. For the pressure snap-shot, the iso-surface visualizes a surface of constant pressure, while the iso-line shows where the axial velocity is zero.

4.3 Fourier analysis of the pressure fluctuations

The recorded pressure fluctuations at the four different draft-tube locations, MG0-MG3 (see Fig. 3), are examined using a Fourier analysis. Let f be a real periodic valued function of time with period T. Suppose we sample f at N equally spaced time interval of length Δ seconds starting at time t_0. That is we have $s_i = f(t_0 + i\Delta)$, $i = 0,1,...,N-1$. In particular, it assumes that $f(t_0) = f(t_0 + N\Delta)$. Hence, the period is assumed to be $T = N\Delta$. The interpolating trigonometric polynomial g(t) which approximates the function $f(t)$ can be written as

$$g(t) = A_0 + \sum_{n=1}^{(N-1)/2} A_n \cos[\omega_n(t-t_0)] - \sum_{n=1}^{(N-1)/2} B_n \sin[\omega_n(t-t_0)]$$

with

$$A_0 = \frac{c_0}{N} = \frac{1}{N}\sum_{n=0}^{N-1} s_n , \quad A_n = \frac{2c_{2n}}{N}, \quad B_n = \frac{2c_{2n+1}}{N}, \text{ and } \quad \omega_n = \frac{2\pi(n+1)}{N\Delta} = \frac{2\pi(n+1)}{T}$$

A_0 is the average value of the samples, while A_n and B_n are respectively the cosine and sine modes amplitudes for the angular frequency ω_n.

The FFTRF subroutine from International Math and Statistics Libraries (IMSL) is used to compute the discrete Fourier transform and the reconstruction signal. The numerical unsteady pressure recorded in all monitors (MG0-MG3) as well as the reconstruction signals are plotted, and the corresponding frequency spectra are plotted in Fig. 10.

As shown in Fig. 10, the simulation performed in OpenFOAM over-estimates the amplitude of the vortex rope at all the four different probes positions. At MG1, MG2 and MG3, the numerical prediction of vortex rope amplitude is largely over-estimated, relative to the experimental data. This means that the vortex rope is well developed and more compact for a longer distance in the numerical computation than in the experimental investigation. This conclusion asserts the previous comparisons between numerical and experimental investigations of the vortex rope [11]. The numerical computation using the k-ε turbulence model over-estimates the amplitude of the vortex rope, predict a more compact vortex rope than the experimental investigation, and fails to predict accurately the dispersion of the vortex rope.

However, what is more unexpected is the shift in the frequency of the vortex rope between the experimental value and the numerical one. The frequency of the vortex rope predicted by the simulation is about 18.5 Hz, while it was measured around 15.5 Hz with the pressure transducers (Fig. 10). The computed results show as well a harmonic around 15.3 Hz, which corresponds to the frequency of the runner rotating.

Though numerical results overestimates the amplitude of the vortex rope, it is very interesting to notice that the numerical simulation succeeds in successfully computing an oscillation in the axial direction of the vortex rope. This oscillation can be seen in Fig. 10 on the right, at all the different positions, and the frequency of this oscillation is around 3 Hz (see Fig. 10, left). This oscillation of the vortex rope can be seen as well in the latest experimental investigation [16].
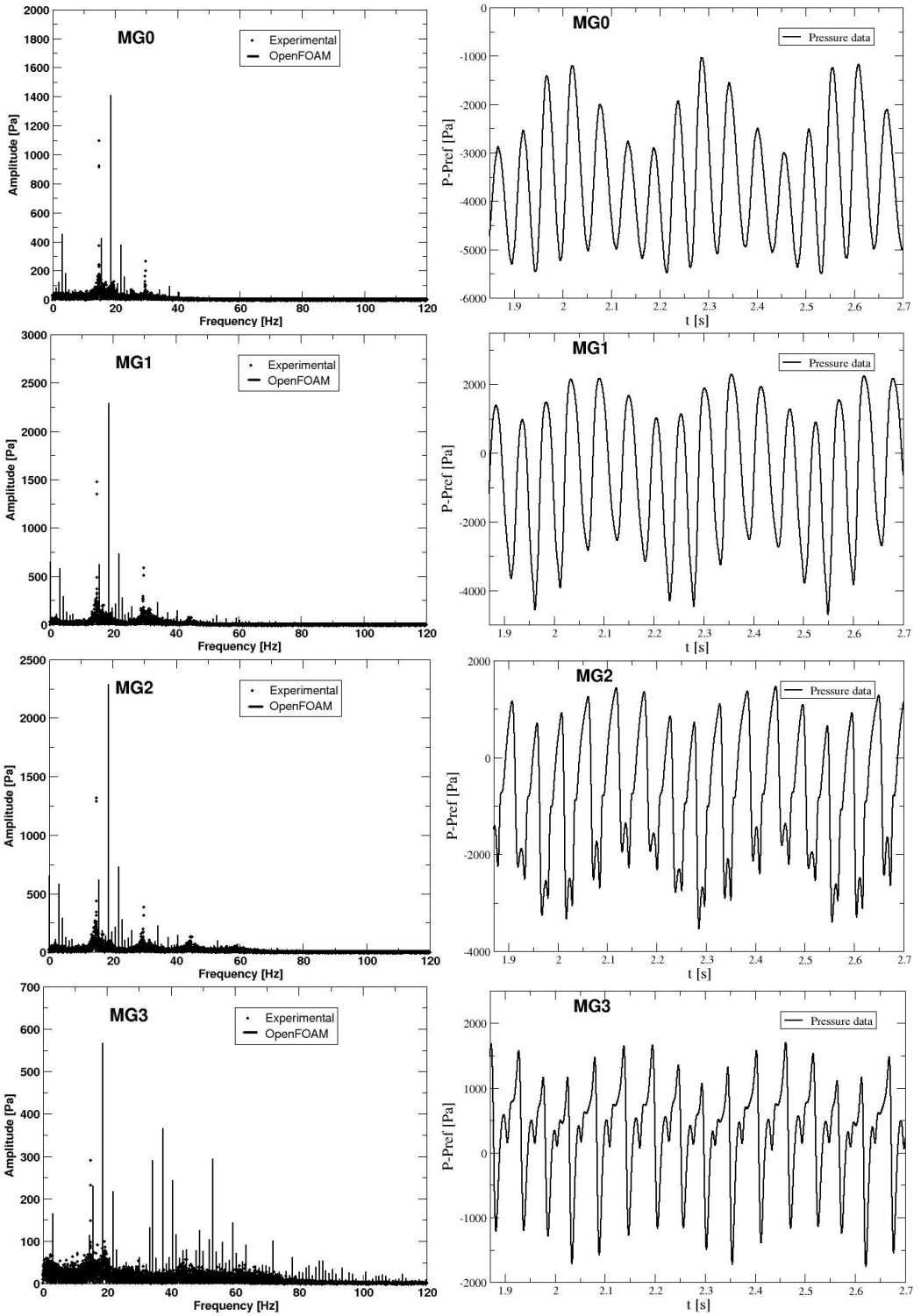
Fig. 10 Fourier analysis (left) of the numerical pressure data (right) at the four positions MG0-MG3 (from top to down)

4.4 Importance of the time step in transient rotor-stator simulations

As the numerical simulation solves the Unsteady Reynolds Averaged Navier-Stokes equation, the time dependency is taken into account. Fig. 11 presents a comparison between the previously described simulation, Case 1, with a time step of $2,35 \cdot 10^{-4}$ s, yielding a maximum Courant number of 5 and an angle of 1.3°per time step, and a more detailed simulation, Case 2, with a time step of $4,76 \cdot 10^{-5}$ s, yielding a maximum Courant number of 1, and an angle of 0.25° per time step. Both simulations start from the same initial conditions from the same settings as Case 1. Thus the Case 2 results experience an initial transient, and the flow is not to be considered developed. Case 2 predicts the wakes of the runner blades at MG0, while Case 1 doesn't (Fig. 11). Moreover, one can see that the prediction of the vortex rope frequency in Case 2 seems to develop to a lower one than in Case 1. However, the computation time is increase by a factor of 4,5 for Case 2, so it is necessary to achieve a balance between the computational time and the accuracy of the results.
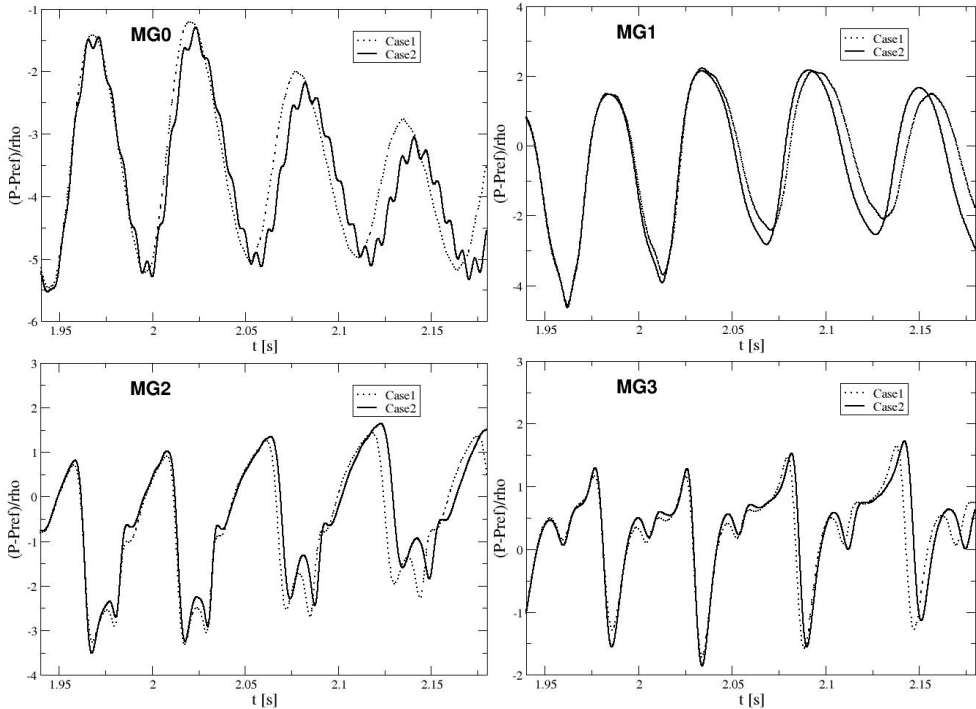

Fig. 11 Comparison between Case 1(Courant number of 5), and Case 2 (Courant number of 1) for the four pressure transducers positions MG0-MG3.

5. Conclusion

We present in this paper the unsteady three-dimensional numerical investigations of the swirling flow with helical vortex breakdown in a conical diffuser, quite similar to the flow encountered in Francis turbines draft tube cone when operating at partial discharge. The three-dimensional computational domain corresponds to the test section installed on test rig at Politehnica University of Timisoara. The full three-dimensional flow is computed with the help of a transient method, using the standard k-ε model available in OpenFOAM.

First, the velocity profiles computed with OpenFOAM are in good agreement with the design profiles upstream and downstream to the free runner. The axial velocity is in very good agreement in both sections, which shows that the discharge imposed in the OpenFOAM simulation is the same as that of the inviscid design theory. As expected, the numerical simulation over-estimates the tangential velocity at section S2, located downstream the runner. The discrepancy corresponds to the difference between design runner speed 870 rpm and value measured on the test rig 920 rpm.

Second, the time average computed velocity profiles are validated with experimental data along to the three sections W0 (situated in the convergent part), W1 and W2 (both displaced in the conical section). The velocity computed by OpenFOAM shows good agreement with experiment data.

Finally, the unsteady pressure computed numerically with OpenFOAM is compared with experimental data. The simulation performed in OpenFOAM overestimates the amplitude of the vortex rope at all the four different probes positions. The fundamental frequency of the vortex rope is rather well predicted, but by reducing the time step of the transient computation, a more accurate prediction of the frequency and amplitude of the vortex rope may be achieved.

Acknowledgements

References

[1] Avellan, F., 2000, "Flow Investigation in a Francis Draft Tube: The FLINDT Project," in Proceedings of the 20th IAHR Symposium on Hydraulic Machinery and Systems, Charlotte, USA, Paper DES-11.

[2] Susan-Resiga, R., Muntean, S., Bosioc, A., Stuparu, A., Milos, T., Baya, A., Bernad, S., and Anton, L.E., 2007, "Swirling Flow Apparatus and Test Rig for Flow Control in Hydraulic Turbines Discharge Cone," in Proceedings 2nd IAHR International Meetings of the Workgroup in Cavitation and Dynamic Problems in Hydraulic Machinery and Systems, Scientific Bulletin of the Politehnica University of Timisoara, Transcations on Mechanics, Vol. 52(66), Fasc.6, pp. 203-216.

[3] Susan-Resiga, R., Muntean, S., Tanasa, C., and Bosioc, A., 2008, "Hydrodynamic Design and Analysis of a Swirling Flow Generator," in Proceedings of the 4th German – Romanian Workshop on Turbomachinery Hydrodynamics (GRoWTH), June 12-15, 2008, Stuttgart, Germany.

[4] Bosioc, A., Susan-Resiga, R., and Muntean, S., 2008, "Design and Manufacturing of a Convergent-Divergent Test Section for Swirling Flow Apparatus," in Proceedings of the 4th German – Romanian Workshop on Turbomachinery Hydrodynamics (GRoWTH), June 12-15, 2008, Stuttgart, Germany.

[5] Susan-Resiga, R., Muntean, S., and Bosioc, A., 2008, "Blade Design for Swirling Flow Generator," in Proceedings of the 4th German – Romanian Workshop on Turbomachinery Hydrodynamics (GRoWTH), June 12-15, 2008, Stuttgart, Germany.

[6] Susan-Resiga, R., Vu, T.C., Muntean, S., Ciocan, G.D., and Nennemann, B., 2006, "Jet Control of the Draft Tube Vortex Rope in Francis Turbines at Partial Discharge," in Proceedings of the 23rd IAHR Symposium on Hydraulic Machinery and Systems, Yokohama, Japan, Paper F192.

[7] Muntean, S., Susan-Resiga, R., Bosioc, A., Stuparu, A., Baya, A., Anton, L.E., 2008, "Mitigation of Pressure Fluctuation in a Conical Diffuser with Precessing Vortex Rope Using Axial Jet Control Method," in Proceedings of the 24th IAHR Symposium on Hydraulic Machinery and Systems, Foz do Iguassu, Brazil.

[8] Muntean, S., Susan-Resiga, R., and Bosioc, A., 2009, "Numerical Investigation of the Jet Control Method for Swirling Flow with Precessing Vortex Rope," in Proceedings of the 3rd IAHR International Meeting of the Workgroup on Cavitation and Dynamic Problems in Hydraulic Machinery and Systems, Vol. I, Brno, Czech Republic. Paper B2 pp. 65-74

[9] Susan-Resiga, R., and Muntean, S., 2008, "Decelerated Swirling Flow Control in the Discharge Cone of Francise Turbines," in Proceedings of the 4th International Symposium on Fluid Machinery and Fluid Engineering, Beijing, China. Paper IL-18.

[10] Bosioc, A., Susan-Resiga, R., and Muntean, S., 2009, "2D LDV Measurements od Swirling Slow in a Simplified Draft Tube," in Proceedings of the CMFF09, Vol. II, Budapest, Hungary. pp. 833-838

[11] Muntean, S., Nilsson, H., and Susan-Resiga, R., 2009, "3D Numerical Analysis of the Unsteady Turbulent Swirling Flow in a Conical Diffuser Using Fluent and OpenFOAM," in Proceedings of the 3rd IAHR International Meeting of the Workgroup on Cavitation and Dynamic Problem in Hydraulic Machinery and Systems, Brno, Czech Republic.

[12] Nilsson, H., Page, M., Beaudoin, M. and Jasak H., 2008, "The OpenFOAM Turbomachinery Working Group, and Conclusions from the Turbomachinery Session of the Third OpenFOAM Workshop," in Proceedings of the 24th IAHR Symposium on Hydraulic Machinery and Systems, Foz do Iguassu, Brazil.

[13] Beaudoin, M., and Jasak, H., 2008, "Development of a Generalized Grid Interface for Turbomachinery simulations with OpendFOAM," in Proceedings of the OpenSource CFD International Conference, Berlin, Germany.

[14] Petit, O., Nilson, H., Page, M. and Beaudoin, M., 2009, "The ERCOFTAC Centrifugal Pump OpenFOAM Case-Study," in Proceedings of the 3rd IAHR International Meeting of the Workgroup on Cavitation and Dynamic Problem in Hydraulic Machinery and Systems, Brno, Czech Republic.

[15] Zangeneh, M, 1991, "A Compressible Three-Dimensional Design Method for Radial and Mixed Flow Turbomachinery Blades," International Journal for Numerical Methods in Fluids, 13, pp. 599-624.

[16] Tanasa C., Susan-Resiga R., Bosioc A. and Muntean S., 2010, "Mitigation of Pressure Fluctuations in the Discharge Cone of Hydraulic Turbines Using Flow-Feedback," in Proceedings of the 25th IAHR Symposium on Hydraulic Machinery and Systems, Timisoara, Romania (IOP Conf. Series: Earth and Environmental Science 12 012067 doi:10.1088/1755-1315/12/1/012067.

[17] Bosioc. A., Tanasa C., Muntean S. and Susan-Resiga F., 2010, "Unsteady Pressure Measurements and Numerical investigation of the Jet Control Method in a Conical Diffuser with Swirling Flow," in Proceedings of the 25th IAHR Symposium on Hydraulic Machinery and Systems, Timisoara, Romania (IOP Conf. Series: Earth and Environmental Science 12 012017 doi:10.1088/1755-1315/12/1/012017.

[18] Bergman O., 2010, "Numerical Investigation of the Flow in a Swirl Generator, Using OpenFOAM," Master's Thesis in Fluid Mechanics, Chalmers University of Technology, Division of Fluid Mechanics.

Paper IV

Numerical Investigations of Unsteady Flow in a Centrifugal Pump with a Vaned Diffuser

By

O. Petit and H. Nilsson

Numerical Investigations of Unsteady Flow in a Centrifugal Pump with a Vaned Diffuser

Olivier Petit[*]
Department of Fluid Dynamics
Chalmers University of Technology

Håkan Nilsson[†]
Department of Fluid Dynamics
Chalmers University of Technology

Abstract

Computational Fluid Dynamics (CFD) analyse were made to study the unsteady three-dimensional turbulent flow in the ERCOFTAC centrifugal pump test case. The simulations were carried out using the OpenFOAM Open Source CFD software. The test case consists of an unshrouded centrifugal impeller with seven blades and a radial vaned diffuser with 12 vanes. A large number of measurements are available in the radial gap between the impeller and the diffuser where large unsteadiness occurs, making this case ideal for validating numerical methods.

A 3D block-structured fully hexahedral mesh was generated in ICEM-CFD. The computational domain includes the whole geometry, from the inlet pipe to the diffuser radial exit. Results of steady and unsteady calculation are compared with the experimental ones, and four different turbulent models are analyzed, $k - \varepsilon$, realizable $k - \varepsilon$, RNG $k - \varepsilon$ and $k - \omega$ SST. The steady simulation uses the frozen rotor concept, where the results are a crude estimation of the ensemble-averaged flow for a fixed rotor position. A series of such snapshots gives an estimation of the flow unsteadiness in the pump. The unsteady simulation uses a fully resolved sliding grid approach.

The comparisons show that the unsteady numerical results accurately predict the unsteadiness of the flow, demonstrating the validity and applicability of that methodology for unsteady incompressible turbomachinery flow computations. The steady approach is less accurate, with an unphysical advection of the impeller wakes, but accurate enough for a crude approximation. The different turbulence models predict the flow to the same level of accuracy, with slightly different results. The differences between the measured and calculated flows may to some extent be caused by the lack of tip clearance between the impeller blades and the shroud in the present work.

Nomenclature

D_1	Impeller inlet diameter [mm]
D_2	Impeller outlet diameter [mm]
D_3	Diffuser inlet diameter [mm]
D_4	Diffuser outlet diameter [mm]
b	Impeller blade span [mm]
U_2	Impeller trailing edge velocity [m/s]
z_d	Number of diffuser vanes
z_i	Number of impeller blades
Q	Flow rate [m^3/s]
φ	Flow rate coefficient, $4Q/(U_2\pi D_2^2)$
Ψ	Total pressure rise coefficient, $2(p_{out} - p_{in})/\rho U_2^2$
$\tilde{C}_p$	Static pressure coefficient, $2(p - p_{in})/\rho U_2^2$
p_{in}	Static pressure at the inlet of pump [Pa]

---
[*]Corresponding author: Address: Chalmers University of Technology, Department of Fluid Dynamics, Hörsalsvägen 7A, 41296 Gothenburg, Sweden; phone: +46(0)31-772 52 95; fax: +46(0)31-18 09 76; e-mail:`olivierp@chalmers.se`

[†]e-mail:`hani@chalmers.se`

p_{out}	Static pressure at the outlet of the pump [Pa]
n	Rotational speed [rpm]
Re	Reynolds number, $U_2 l/\nu$
ν	Kinematic viscosity [m^2/s]
l	Impeller chord length [m]
G_i	Circumferential pitch, $2\pi/z_i$
T_i	Rotor blade passing period, $2\pi/nz_i$
y_i	Circumferential coordinate in the relative frame
W_r	Radial velocity [m/s]
W_u	Tangential velocity [m/s]
ρ	Fluid density [kg/m^3]
f_r	Frequency of the rotor [Hz]
f_i	Frequency of the impeller blade [Hz]
f_d	Frequency of the diffuser vane [Hz]

1 Introduction

In centrifugal pumps, the relative motion between the rotor and stator, and the small radial gap between the impeller blades and diffuser vanes, result in a highly unsteady flow. This unsteadiness creates high pressure fluctuations, which are in turn responsible for unsteady dynamic forces that create vibrations and can cause damage. A large amount of detailed experimental investigations have therefore been dedicated to understanding the flow in centrifugal pumps. Among those, Dring et al. [1] showed that the two major sources of unsteadiness are potential and blade/wake interactions. In centrifugal turbomachines, the effects of these sources of unsteadiness become comparable [2]. On the basis of the studies mentioned above, Ubaldi et al. [3] built a simplified model of a centrifugal pump with a rotatable vaned diffuser to study rotor-stator interaction. They then investigated the upstream effect of the vaned diffuser on the impeller outflow in the radial gap of the model, as well as the flow in the impeller [4, 5, 6].

The experimental work contributes to an understanding of the flow complexity owing to rotor-stator interaction in the centrifugal pump. However, the knowledge is limited to the number of measurement points. For an extensive and detailed analysis of the flow, many different probes must be positioned in the geometry, although the complete flow field is not monitored. Computational Fluid Dynamics (CFD) techniques have been shown in the recent decades to be a useful complement to experiments. CFD calculations can provide more extensive results in the whole domain, giving a better overall understanding of the flow in the whole turbo-machine. In recent years, improved computational algorithms and hardware development shown convincing evidence that CFD calculations are reliable tools that can be used to analyze the unsteadiness of the flow [7]. However, the methods and software used to make the CFD calculations must be validated by experiments. To achieve this, the European Research Community on Flow Turbulence and Combustion (ERCOFTAC), together with Ubaldi et al. [3], adopted the centrifugal test rig as a test case for joint experimental and theoretical investigations of rotor flow and rotor-stator interaction. The original test case was presented by Combès [8] at the Turbomachinery Flow Prediction ERCOFTAC Workshop in 1999. Intensive studies were then carriedout using proprietary CFD software. 2D numerical simulation was initially the only approach permitted by computer hardware limitations. Bert et al. [9] presented a 2D analysis of the ERCOFTAC centrifugal pump. Following the development of hardware, 3D unsteady studies were then done [10, 11]. The geometry of the ERCOFTAC centrifugal pump is shown in Fig. 1.

Large meshes and short time steps are often used in 3D unsteady calculations, making the simulations computationally heavy. Simulations of this kind are decomposed for parallel processing. This becomes costly when proprietary software is used, where there is an additional license cost for each process. To offer a viable alternative, the community-driven OpenFOAM Turbomachinery Working Group extends and validates OpenFOAM for turbomachinery applications [12]. OpenFOAM is an Open Source library written in C++ [13]. It is based on the finite volume method and has proven to be as accurate as proprietary codes for many applications [14, 15, 16]. 2D numerical simulations of the ERCOFTAC centrifugal pump were previously made using OpenFOAM by Petit et al. [17]. The general behavior of the flow was well captured, but the results suggested the use of 3D simulations for better capturing the unsteadiness of the flow.
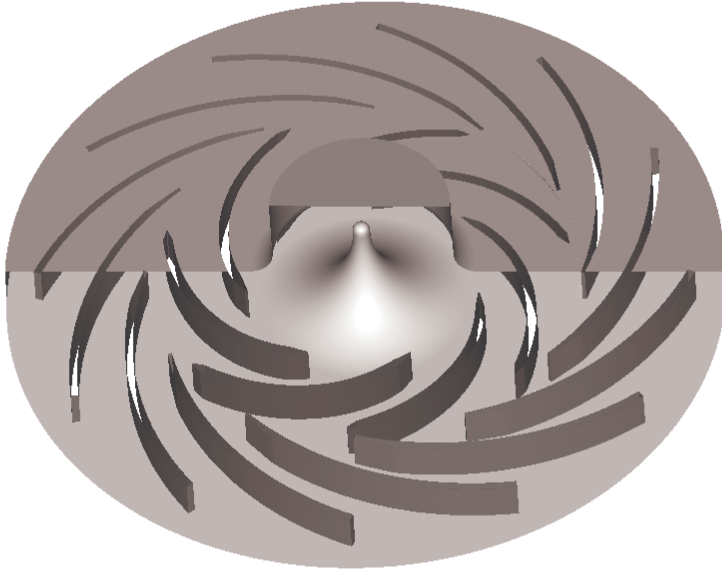
Figure 1: Geometry of the ERCOFTAC centrifugal pump

The present work reports the unsteady flow field of the ERCOFTAC centrifugal pump obtained by 3D steady and unsteady CFD calculation. The steady simulation uses the frozen rotor concept, where the results are a crude estimation of the ensemble-averaged flow for a fixed rotor position. A series of such snapshots gives an estimation of the unsteadiness of the flow in the pump. The unsteady simulation uses a fully resolved sliding grid approach. The unsteady flow is computed using four different turbulent models, the $k - \varepsilon$, the realizable $k - \varepsilon$, the RNG $k - \varepsilon$ and the $k - \omega$ SST. The results are analyzed and compared in detail with the measurements performed by Ubaldi *et al.* [3] in the radial gap between the impeller and diffuser.

2   Test Case and Operating Conditions

The ERCOFTAC centrifugal pump test rig was built by Ubaldi *et al.* [3] and consists of a 420mm diameter unshrouded centrifugal impeller and a 644mm diameter radial vaned diffuser. Details on the geometry and coordinates of the impeller blade and diffuser vane profiles are given in Ubaldi *et al.* [3]. The impeller has 7 untwisted constant thickness backswept blades, and the diffuser has 12 vanes. There is a 6% vaneless radial gap between the impeller and diffuser. The tip clearance can be varied but is set at a value of 0.4mm, corresponding to 1% of the blade span. The tip clearance is not included in the present simulations however.

The measuring techniques used were hot wire anemometry and fast response pressure transducers. The hot wire probe was used to measure the unsteady 3D flow in the vaneless gap at a radial distance of 4mm from the trailing edge of the blade and 8mm from the leading edge of the vane. The unsteady static pressure was measured at the front cover facing the unshrouded impeller passages. The experiments were conducted at a constant rotational speed of 2000 rpm, at the nominal operating condition described in Table.1. The model operates in an open air circuit directly discharged into the atmosphere from the radial diffuser. The inlet air temperature was 298 K and the air density 1.2 kg/m^3.

Impeller	
$D_1 = 240$ mm	Inlet blade diameter
$D_2 = 420$ mm	Outlet diameter
$b = 40$ mm	Blade span
$z_i = 7$	Number of blades
Diffuser	
$D_3 = 444$ mm	Inlet vane diameter
$D_4 = 664$ mm	Outlet vane diameter
$b = 40$ mm	Blade span
$z_d = 12$	Number of vanes
Operating conditions	
$n = 2000$ rpm	Rotational speed
$U_2 = 43.98$ m/s	Impeller tip speed
$\varphi_c = 0.0048$	Flow rate coefficient
$\Psi_c = 0.65$	Total pressure rise coefficient
$Re = 6.5 * 10^5$	Reynolds number

Table 1: Geometric data and operating conditions

3 Computational domain and Numerical Setup

The meshes for the impeller and diffuser regions were generated separately, see Fig. 2. Both of the mesh regions are block structured and were generated using the ICEM-CFD software, with O-grids around the blades and the diffuser vanes and H-grids in the blade passages. Angular geometrical periodicity is used to mesh the different blades. The impeller tip clearance is not included in the present simulations. The mesh has a total of 2 074 078 nodes. The angles of the cells are between $30°$ and $140°$ degrees, with 92% between $70°$ and $100°$. The y^+ values at the walls yield an average value of 50.
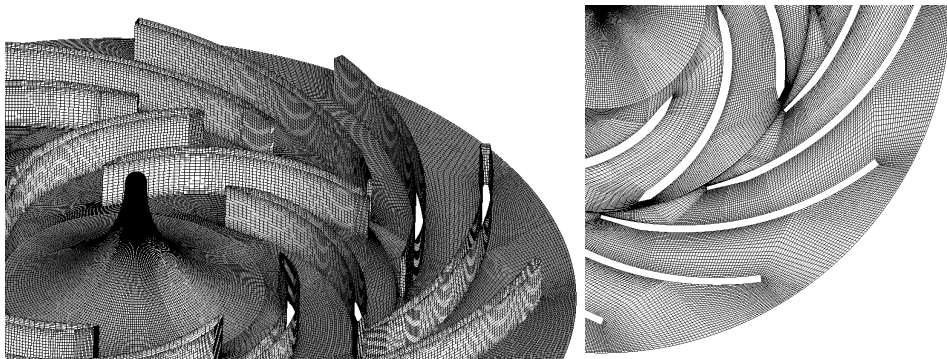

Figure 2: Computational mesh

The continuity equation and the 3D incompressible unsteady Reynolds-averaged Navier-Stokes equations are solved. The eddy-viscosity assumption is used to model the turbulence Reynolds stress tensor, and the standard log-law wall function is used at the walls. A second-order, linear-upwind scheme [18] is used to discretize the convection terms, and the second-order backward scheme is used to discretize the time derivative. The number of iterations in the transient SIMPLE algorithm at each time step is set to 10. This number of iterations is enough to reduce the residuals by three orders of magnitude. The final residuals are below 10^{-6} except for the pressure, which has a final residual of 10^{-5}. The inlet velocity is set to a constant purely axial component, and the inlet turbulence intensity is assumed to be 5%, with a viscosity ratio of 10. At the outlet, all variables are given a zero gradient boundary condition, except for the pressure, which is set to 0. The time step for the unsteady simulations was fixed to $7e^{-5}$ s, which gives a maximum Courant number of 6. The calculations are carried out

Olivier Petit

4

on a cluster, using 8 nodes equipped with 4 cores each. Using these parameters, one impeller rotation in the unsteady simulation takes 48 hours to compute.

Two different rotor-stator interaction methods are used in this work. The first is a steady-state multiple frame of reference approach, where the impeller flow field is solved in a rotating frame of reference and the diffuser flow in a fixed frame of reference [17]. The local fluxes at the interface are transferred using a General Grid Interface (GGI), implemented in OpenFOAM by Beaudoin and Jasak [19] and validated by 2D simulations of the ERCOFTAC centrifugal pump [17]. It is a method commonly used in proprietary CFD codes, where it is referred to as *frozen rotor*. This approach resembles a snapshot of the flow, frozen in time, thus failing to predict the unsteadiness of the flow between the diffuser vanes. It also gives an incorrect advection of the impeller wakes in the vaned diffuser. It is a fast preliminary method however, and gives satisfying results in the radial gap between the impeller and diffuser that can also serve as a good initial condition for unsteady simulations. The second rotor-stator interaction method resolves the flow unsteadiness using a *sliding grid* approach. This transient method rotates the impeller part of the mesh with respect to the stator part at each time step. In this cases, the local fluxes are also transferred using the GGI interface, which is updated every time step. The interaction between the impeller and diffuser is thus fully resolved. The chosen time step corresponds to a rotation of the impeller of about $0.84°$. Previous studies have shown that this angular time step is sufficient to allow the transient solver to catch the unsteadiness of the flow [20].

The results from two different rotor-stator interaction approaches are first compared with each other and with the measurement database, using the standard $k - \varepsilon$ turbulence model to model the eddy-viscosity. A comparison is then made of the results from four different turbulence models. An extensive comparison of the different RANS turbulence models available in OpenFOAM was made by Moradnia [21]. The focus in Moradnia's study was particularly on high and low Reynolds number two-equation eddy-viscosity turbulence models, and on Reynolds Stress Transport turbulence models. The conclusion of the study by Moradnia was that four high Reynolds turbulence models were better at predicting the flow while preserving numerical stability and efficiency. These are the $k - \varepsilon$ [22], the realizable $k - \varepsilon$ [23], the RNG $k - \varepsilon$ [24] and the $k - \omega$ SST [25] turbulence models. These models were thus been chosen for comparisons in the present work.

4   Results and Discussion

The following sections present and discuss the results of the steady and unsteady rotor-stator interaction approaches using the standard $k - \varepsilon$ turbulence model. The results are compared with the experimental database. We also discuss the main differences between the results from the frozen rotor and sliding grid approaches. Finally, comparisons of the unsteady results using four turbulence models, $k - \varepsilon$, realizable $k - \varepsilon$, RNG $k - \varepsilon$ and $k - \omega$ SST, are presented.

All the kinematic quantities are normalized with the rotor tip speed, U_2. The circumferential rotor relative coordinate, y_i, and the axial coordinate, z, are made non-dimensional by means of the circumferential pitch of the rotor, $G_i = 2\pi r/z_i$, and the blade span at the rotor outlet, b, respectively. The velocity comparisons are made at mid-span in the radial gap, at a radius of $1.02 * R_2$. The time, t, is normalized by the rotor blade passing period, T_i. Triangles and squares in the plots describe the positions of the impeller blades and diffuser vanes, respectively. The results are observed in the relative frame, such that the impeller blades (triangles) have a fixed position in time, while the diffuser vanes (square) move from left to right.

4.1   Steady-State Results with the $k - \varepsilon$ Turbulence Model

Figures 3 and 4 show the ensemble-averaged experimental and calculated radial and tangential velocities in the radial gap at $R = 1.02 * R_2$ over two impeller pitches between the hub (z/b = 0.05) and the shroud (z/b= 0.95). The behavior of the flow is roughly captured by the simulation. However, a shift of the predicted wakes can be observed in Fig. 4. Figure 5 extracts the same results at mid-span (z/b=0.5). Although the radial velocity is reasonably well predicted, the phase shift can also be observed. The tangential velocity is incorrectly predicted after the rotor blade passage, as the wake remains at the same place, and aligns with the local relative streamlines, instead of being advected into the diffuser vanes channel and dissolving.

t/T_i represents the position of the impeller blade relative to the diffuser vane. For steady simulation, t/T_i does not vary over time. The rotor part of the mesh must be rotated to get a new position for the impeller blade, and the flow must be computed once again. A sequence of many steady simulations with different angular positions for the impeller blades will then give a sequence of snapshots of the unsteadiness of the flow.
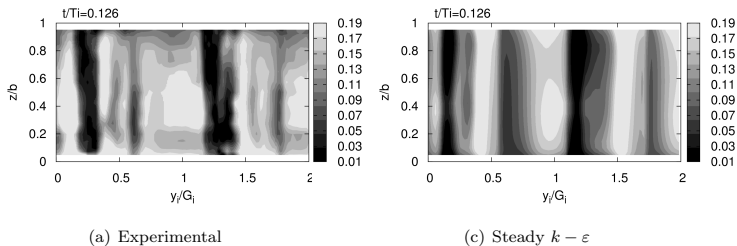

(a) Experimental   (c) Steady $k - \varepsilon$

Figure 3: Experimental and calculated radial velocity in the radial gap for the steady-state simulation using the $k - \varepsilon$ turbulence model

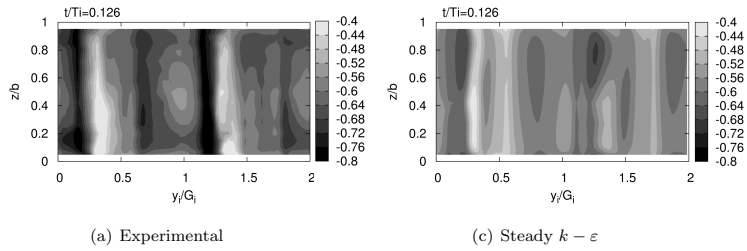(a) Experimental   (c) Steady $k - \varepsilon$

Figure 4: Experimental and calculated tangential velocity field in the radial gap for the steady-state simulation using the $k - \varepsilon$ turbulence model

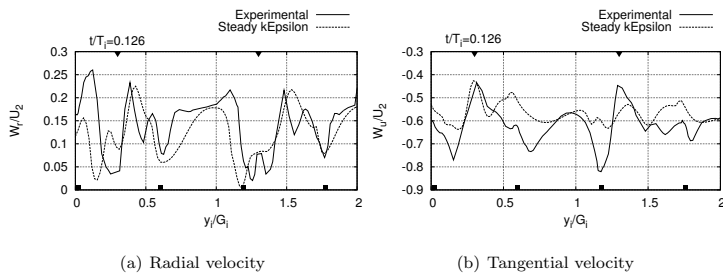(a) Radial velocity   (b) Tangential velocity

Figure 5: Radial and tangential velocity at the impeller outlet at mid-span for the steady-state simulation using the $k - \varepsilon$ turbulence model

Olivier Petit   7

4.2 Unsteady Results with the $k - \varepsilon$ Turbulence Model

The instantaneous distributions of the ensemble-averaged radial and tangential velocity in the radial gap at mid-span when using the $k-\varepsilon$ turbulence model are presented in Figs. 6 and 7, respectively. The calculated profiles are in good agreement with the measurements. They show a good prediction of the wake position, and of the potential interaction linked to the diffuser vane leading edge, corresponding to low radial velocity peaks. However, some differences are still visible. The calculations over-predict the maximum of the wake for the tangential velocity, and a slight phase shift is still visible at the maximum of the wakes. This can be explained by Figs. 8 and 9, where it can be seen that the wakes predicted by the calculation are orthogonal to the shroud, while the measured ones are slightly inclined. This creates a phase shift at mid-span. A comparison of the static pressure is presented in Fig. 10. The general evolution of the pressure is well predicted, but a slight phase shift is also present, and the global fluctuation of the mean pressure level is not accurately predicted. It is important to remember that some secondary flows were not included in this calculation. For example, Ubaldi *et al.* [6] explained that the low pressure region located in the blade passage near the suction side seemed to be caused by the tip clearance vortex. Some near-wall effects in the experiments could also have an impact on the experimental results and may explain the difference between the calculated and experimental results.

Figure 11(a) shows the pressure signals obtained by two probes located in the radial gap and at the outlet of the diffuser. The frequency contents of the signals are shown in Figs. 11(b). The reconstructed signals using selected frequencies are shown in Figs.11(c). The frequency of the rotor is $f_r = 2000/60 = 33.3$ Hz. The frequency of the impeller blades is $f_i = f_r * z_i = 232$ Hz and that of the diffuser vanes $f_d = f_r * z_d = 400$ Hz. The signal in the radial gap is dominated by the impeller blades' frequency and its multiples, f_i, see Fig. 11(b). The impeller wakes are high energy regions and decay very rapidly in the radial gap. At the outlet of the diffuser, a similar signal is shown in Fig. 11(c), but a reduction in amplitudes with values lower than those found in the pump is apparent.
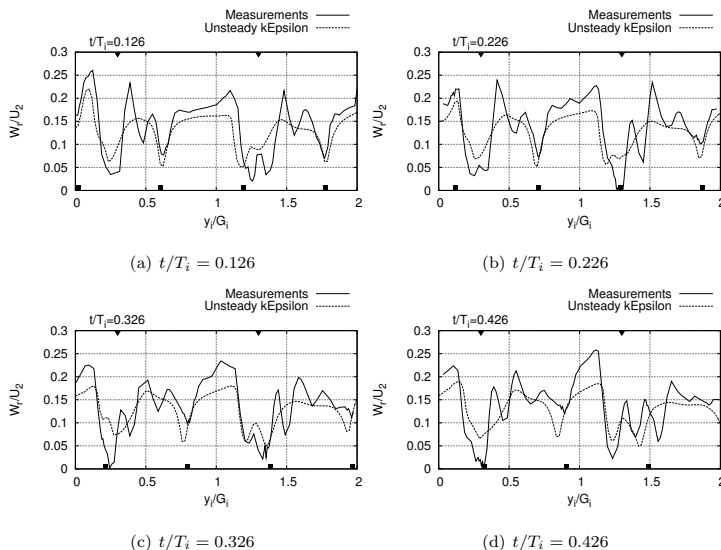

(a) $t/T_i = 0.126$

(b) $t/T_i = 0.226$

(c) $t/T_i = 0.326$

(d) $t/T_i = 0.426$

Figure 6: Radial velocity in the radial gap ($R/R_2 = 1.02$) at mid-span for the unsteady simulation using the $k - \varepsilon$ turbulence model

(a) $t/T_i = 0.126$ (b) $t/T_i = 0.226$

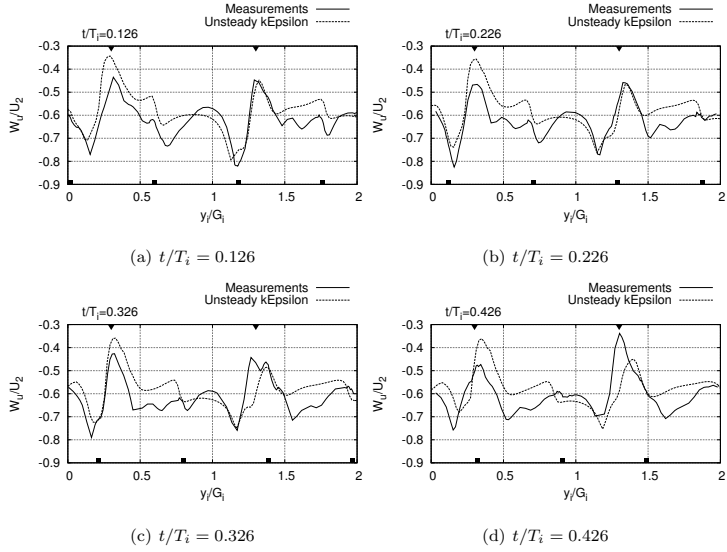(c) $t/T_i = 0.326$ (d) $t/T_i = 0.426$

Figure 7: Tangential velocity in the radial gap ($R/R_2 = 1.02$) at mid-span for the unsteady simulation using the $k - \varepsilon$ turbulence model
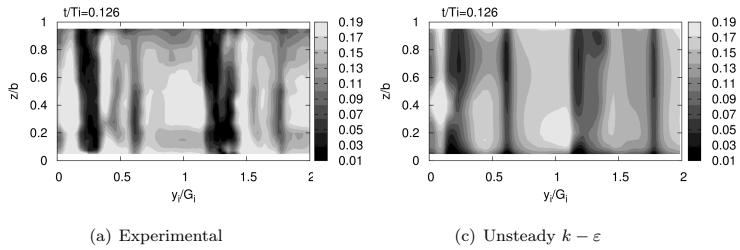

(a) Experimental   (c) Unsteady $k - \varepsilon$

Figure 8: Experimental and calculated radial velocity in the radial gap for the unsteady simulation using the $k - \varepsilon$ turbulence model

Olivier Petit   9

t/Ti=0.126

(a) Experimental
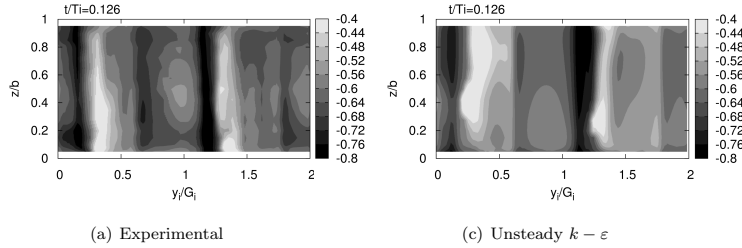
t/Ti=0.126

(c) Unsteady $k - \varepsilon$

Figure 9: Experimental and calculated tangential velocity in the radial gap for the unsteady simulation using the $k - \varepsilon$ turbulence model
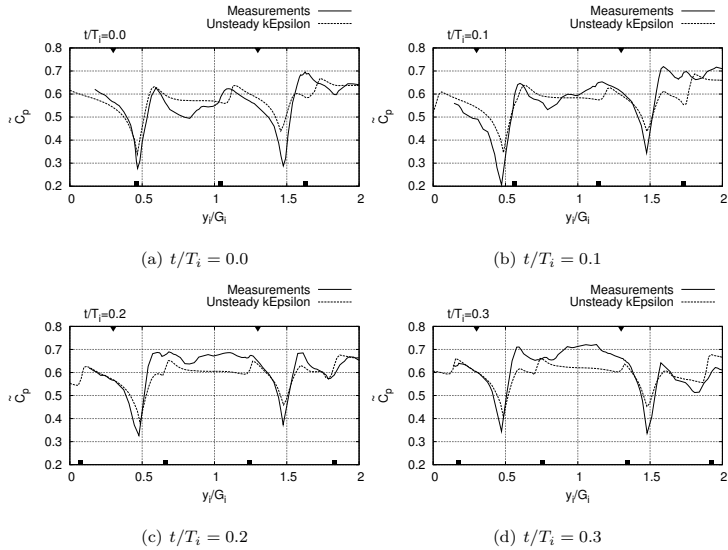
Measurements
Unsteady kEpsilon

t/T$_i$=0.0

Measurements
Unsteady kEpsilon

t/T$_i$=0.1

(a) $t/T_i = 0.0$

(b) $t/T_i = 0.1$

Measurements
Unsteady kEpsilon

t/T$_i$=0.2

Measurements
Unsteady kEpsilon

t/T$_i$=0.3

(c) $t/T_i = 0.2$

(d) $t/T_i = 0.3$

Figure 10: Static pressure coefficient $\tilde{C}_p$ in the radial gap ($R/R_2 = 1.02$) at mid-span for the unsteady simulation using the $k - \varepsilon$ turbulence model

(a) Original signal

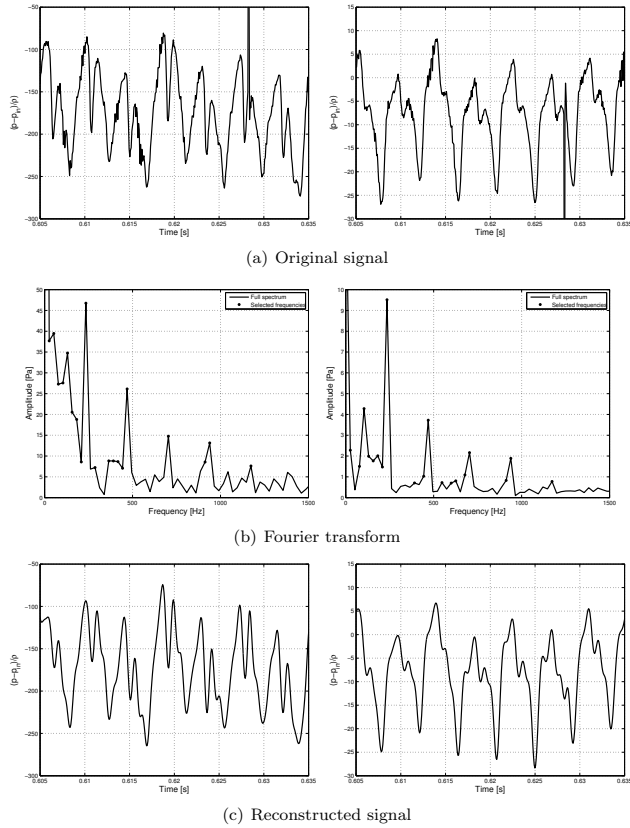(b) Fourier transform

(c) Reconstructed signal

Figure 11: Pressure signal for the probe located at the outlet of the impeller (left) and at the outlet of the diffuser (right). The signal in (c) is reconstructed using the 20 main frequencies selected in (b).

4.3 Comparison the Frozen Rotor and Sliding Grid Approaches.

Fig. 12 illustrates the main difference between the frozen rotor and sliding grid results. The velocity magnitude behind the rotor blades in the frozen rotor simulation is shown in Fig. 12(a). Figures .12(b) - 12(c) show the velocity magnitude behind the rotor blades at different time steps for the sliding grid approach. The wakes in the frozen rotor simulation suddenly change direction when they enter the absolute frame of reference, in the impeller region. The wakes are aligned with the local streamlines, which is a fundamental problem with the frozen rotor concept. The wakes advected in the sliding grid approach do not change direction when they enter the diffuser region, but are advected in the diffuser vane passages and cut by the diffuser vanes.
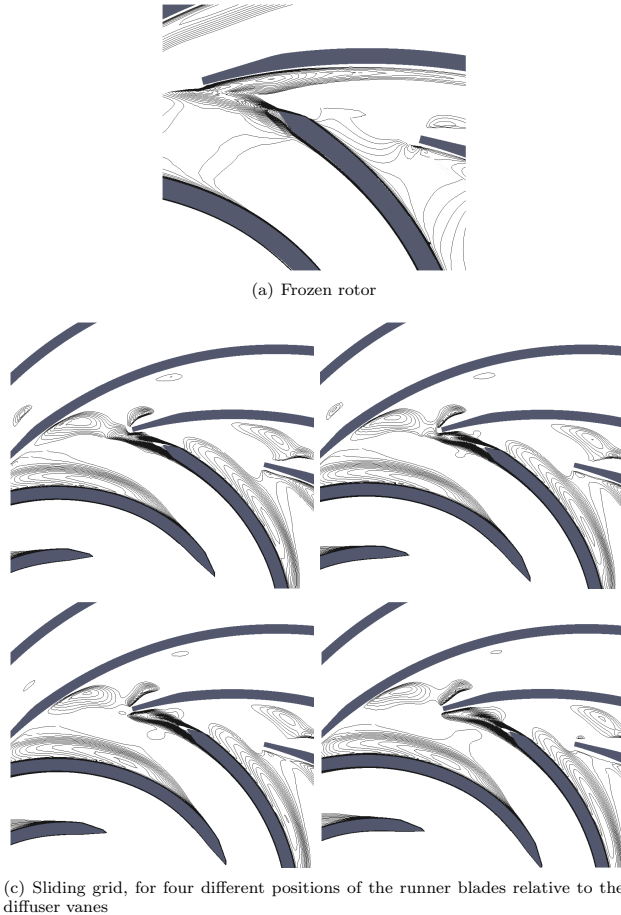

(a) Frozen rotor

(c) Sliding grid, for four different positions of the runner blades relative to the diffuser vanes

Figure 12: Prediction of the wake behind the impeller for the frozen rotor and sliding grid approaches

4.4 Comparison Between Four Turbulence Models

The four two-equation turbulence models, $k - \varepsilon$ [22], realizable $k - \varepsilon$ [23], RNG $k - \varepsilon$ [24] and $k - \omega$ SST [25], used with the sliding grid approach are here compared for one position of the impeller blades with respect to the diffuser. The position differs for the pressure and velocity comparisons since Ubaldi *et al.* presented the velocity measurements for $t/T_i = 0.126$ and the pressure measurements for $t/T_i = 0$. Figures 13 and 14 show that all four turbulence models predict the flow distribution very well. The differences between the numerical and experimental results may be explained by the lack of tip clearance secondary flow in the numerical model, as suggested by Ubaldi *et al.* [3]. It is interesting to note that the calculation using the realizable $k - \varepsilon$ turbulence model very accurately predicts the maximum and minimum peak values of the wakes for the radial velocity, although the wakes are thinner than the ones of the experimental results. However, the tangential velocity in the impeller wakes is largely over-predicted when the realizable $k - \varepsilon$ turbulence model is used. Figure 15 shows that all four turbulence models predict the pressure drop in the wakes behind the impeller but fail to predict the pressure fluctuations in the diffuser vanes passage. In general, the four different turbulence models seem to over-predict the tangential velocity, as shown in Fig. 16. This could be explained by the lack of leakage flow, as well as the use of the wall function approach, which fails to predict an accurate boundary layer flow. Figure 17 shows that all the models predict the large radial velocity at mid-span near the pressure side of the blades. This was not predicted at al in previous studies by Combès *et al.* [26] and Petit *et al.* [17]. The calculations made with the $k - \varepsilon$ and the RNG $k - \varepsilon$ turbulence models predict this feature in the lower part of the channel rather than centered in the mid-span, as shown in Fig. 17.
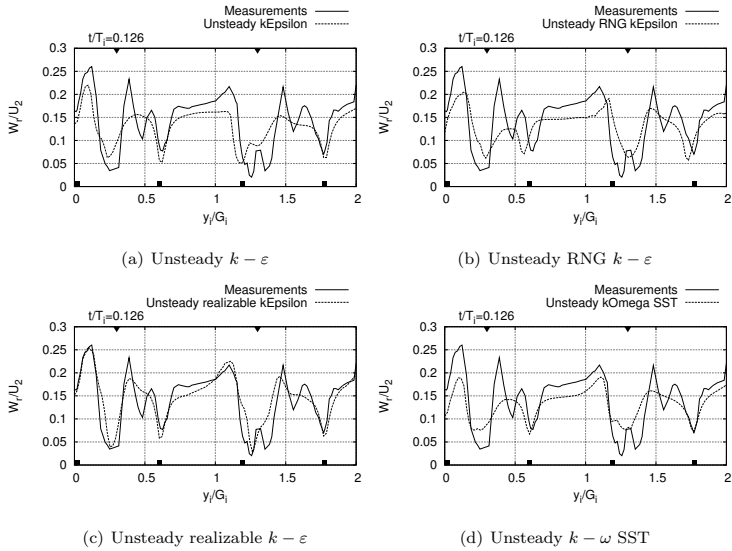

(a) Unsteady $k - \varepsilon$

(b) Unsteady RNG $k - \varepsilon$

(c) Unsteady realizable $k - \varepsilon$

(d) Unsteady $k - \omega$ SST

Figure 13: Radial velocity in the radial gap ($R/R_2 = 1.02$) at mid-span

(a) Unsteady $k - \varepsilon$ (b) Unsteady RNG $k - \varepsilon$

(c) Unsteady realizable $k - \varepsilon$ (d) Unsteady $k - \omega$ SST
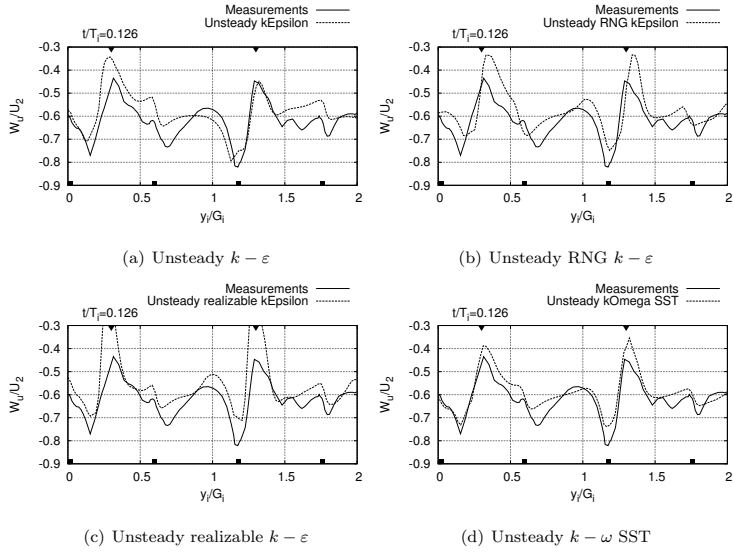
Figure 14: Tangential velocity in the radial gap ($R/R_2 = 1.02$) at mid-span

(a) Unsteady $k - \varepsilon$ (b) Unsteady RNG $k - \varepsilon$

(c) Unsteady realizable $k - \varepsilon$ (d) Unsteady $k - \omega$ SST
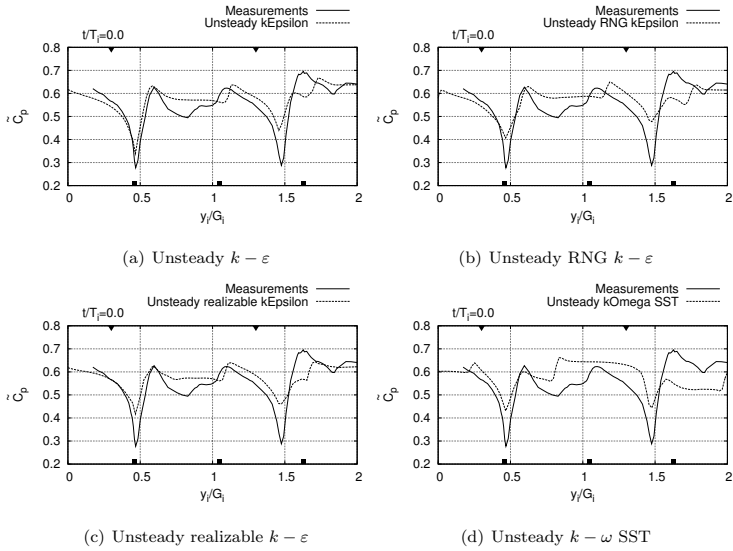
Figure 15: Static pressure coefficient, $\tilde{C}p$, in the radial gap ($R/R_2 = 1.02$) at mid-span.

Olivier Petit   14

(a) Experiment

(b) Unsteady $k - \varepsilon$

(c) Unsteady RNG $k - \varepsilon$

(d) Unsteady realizable $k - \varepsilon$

(e) Unsteady $k - \omega$ SST
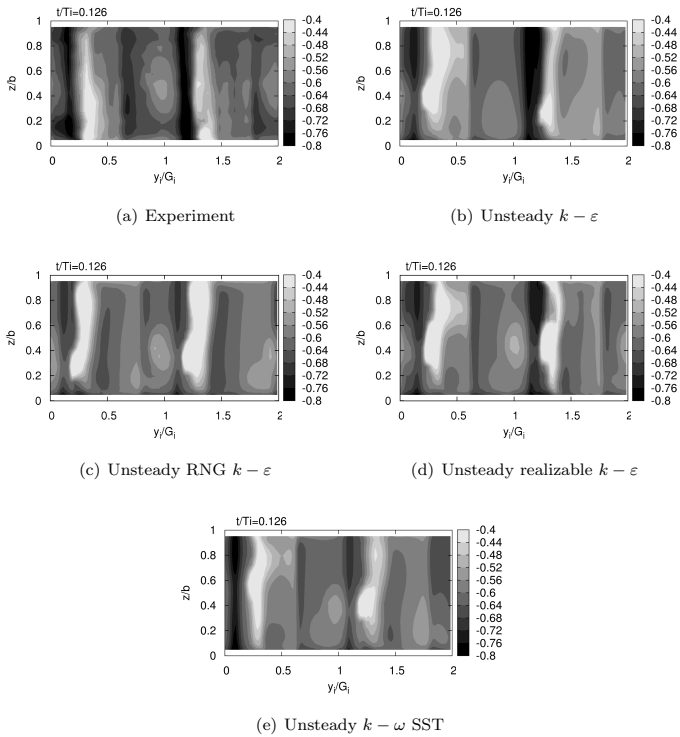
Figure 16: Tangential velocity in the radial gap ($R/R_2 = 1.02$)

(a) Experiment

(b) Unsteady $k - \varepsilon$

(c) Unsteady RNG $k - \varepsilon$

(d) Unsteady realizable $k - \varepsilon$
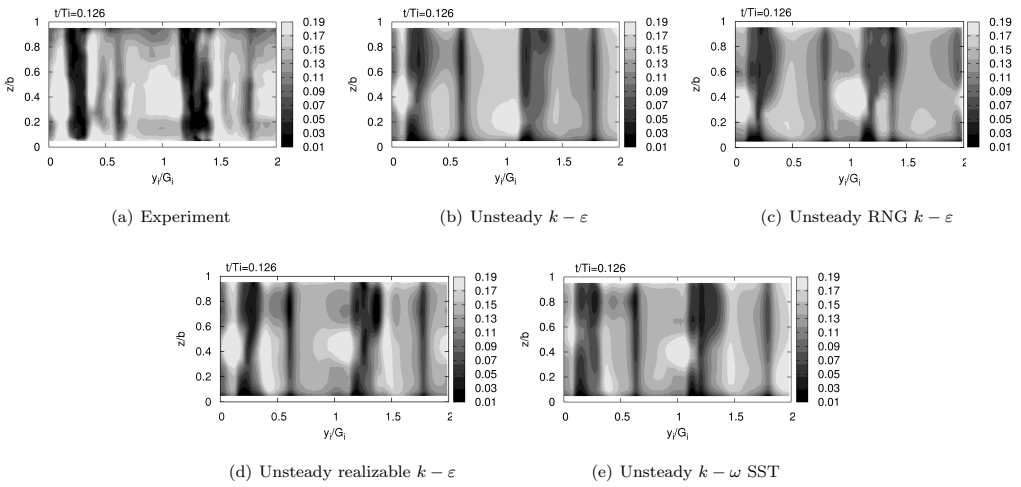
(e) Unsteady $k - \omega$ SST

Figure 17: Radial velocity in the radial gap ($R/R_2 = 1.02$)

5   Conclusion

3D steady and unsteady simulations were carried out with the OpenFOAM CFD tool to study rotor-stator interaction in a centrifugal pump with a vaned diffuser. The four basic turbulence models, $k - \varepsilon$, realizable $k - \varepsilon$, RNG $k - \varepsilon$ and $k - \omega$ SST, were used to perform calculations. The results were compared with the experimental investigation presented by Ubaldi *et al.* [3]. Although the secondary leakage flow was not included in the numerical model, the results show qualitatively good agreement with the experimental results.

The steady numerical simulation with the $k - \varepsilon$ turbulence model shows reasonably good agreement with the measurements, although it obviously does not predict the important unsteadiness. The numerical results in the radial gap yield good agreement with the experimental ones, but the flow in the diffuser passage is incorrectly predicted. The corresponding unsteady simulation resolves most of the unsteadiness and accurately predicts the behavior of the flow. Analyzing the pressure signals at the impeller and diffuser exits, it was observed that the impeller wakes are advected to the exit of the diffuser.

The results of four different turbulence models were compared with the experimental results. The turbulent models yield slightly different results but predict the flow unsteadiness to the same level of accuracy.

To further improve the numerical results, the leakage flow between the impeller blades and the shroud should be taken into account. Large Eddy Simulation (LES) or hybrid methods such as Detached Eddy Simulation (DES) are suggested to more accurately resolved the flow unsteadiness.

6   Acknowledgments

References

[1] R.P. Dring, H.D. Joslyn, L.W. Hardin, and J.H. Wagner. Turbine Rotor-Stator Interaction. *A.S.M.E Journal of Engineering for Power*, 104(4):729–742, 1982. DOI: 10.1115/1.3227339.

[2] N. Arndt, A.J. Acosta, C.E Brennen, and T.K. Caughey. Experimental Investigation of Rotor-Stator Interaction in a Centrifugal Pump with Several Diffusers. *A.S.M.E transactions*, 112:98–108, 1990.

[3] M. Ubaldi, P. Zunino, G. Barigozzi, and A. Cattanei. An Experimental Investigation of Stator Induced Unsteadiness on Centrifugal Impeller Outflow. *Journal of Turbomachinery*, 118(1):41–54, 1996. DOI: 10.1115/1.2836604.

[4] M. Ubaldi, P. Zunino, G. Barigozzi, and A. Ghiglione. Non-intrusive Measurements of the Unsteady Flow in the Radial Gap between Centrigugal Impeller and Vaned Diffuser. *12th Symposium on Measuring Techniques for Transonic and Supersonic Flow in Cascades and Turbomachines*, 1994.

[5] M. Ubaldi, P. Zunino, G. Barigozzi, and A. Ghiglione. LDV Investigation of the Rotor-Stator Aerodynamic Interaction in a Centrifugal Turbomachine. *8th International Symposium on Applications of Laser Techniques to Fluid Mechanics*, 1996.

[6] M. Ubaldi, P. Zunino, and A. Ghiglione. Detailed Flow Measurements within the Impeller and the Vaneless Diffuser of a Centrifugal Turbomachine. *Experimental Thermal and Fluid Science*, 17:147–155, 1998.

[7] H. Keck and M. Sick. Thirty Years of Numerical Flow Simulation in Hydraulic Turbomachines. *Acta Mechanica*, 201(1-4):211–229, 2008. DOI: 10.1007/s00707-008-0060-4.

[8] J.F. Combes. Test Case U3: Centrifugal Pump with a Vaned Diffuser. *ERCOFTAC Seminar and Workshop on Turbomachinery Flow Prediction VII*, 1999.

[9] P.F. Bert, M. Pessiani, J.F. Combes, and J.L Kueny. Unsteady Flow Calculation in a Cross Flow Fan Using a Finite Element Method. *A.S.M.E paper, int. Gas Turbine and Aeroengine Congress*, 1996.

[10] M. Zhang, H. Wang, and H. Tsukamoto. Numerical Analysis of Unsteady Hydrodynamic forces on a Diffuser Pump Impeller due to Rotor-Stator Interaction. *A.S.M.E Joint U.S.-European Fluids Engineering Division Conference*, 2002.

[11] K. Majidi. Numerical Study of Unsteady Flow in a Centrifugal Pump. *Journal of Turbomachinery*, 127:363–371, 2005.

[12] H. Nilsson, M. Page, M. Beaudoin, and H. Jasak. The OpenFOAM Turbomachinery Working Group, and Conclusions from the Turbomachinery Session of the Third OpenFOAM Workshop. *3rd IAHR International Meeting of the Workgroup on Cavitation and Dynamic Problems in Hydraulic Machinery and Systems - Brno*, 2009.

[13] H.G. Weller, G. Tabor, H. Jasak, and C. Fureby. A Tensorial Approach to Computational Continuum Mechanics using Object-Oriented Techniques. *Computers in Physics*, Vol.12(No.6), 1998.

[14] O. Petit, H. Nilsson, T. Vu, O. Manole, and S. Leonsson. The Flow in the U9 Kaplan Turbine - Preliminary and Planned Simulations Using CFX and OpenFOAM. *24th IAHR Symposium on Hydraulic Machinery and Systems*, 2008.

[15] S. Muntean, H. Nilsson, and R.F. Susan-Resiga. 3D Numerical Analysis of the Unsteady Turbulent Swirling Flow in a Conical Diffuser Using Fluent and OpenFOAM. *3rd IAHR International Meeting of the Workgroup on Cavitation and Dynamic Problems in Hydraulic Machinery and Systems - Brno*, 2009.

[16] H. Nilsson. Evaluation of OpenFOAM for CFD of Turbulent Flow in Water Turbines. *23rd IAHR Symposium on Hydraulic Machinery and Systems*, 2006.

[17] O. Petit, M. Page, M. Beaudoin, and H. Nilsson. The ERCOFTAC Centrifugal Pump OpenFOAM Case-Study. *3rd IAHR International Meeting of the Workgroup on Cavitation and Dynamic Problems in Hydraulic Machinery and Systems - Brno*, 2009.

[18] H.K. Versteeg and Malalasekera W., editors. *An Introduction to Computational Fluid Dynamics: the Finite Volume Method*. Pearson Education Ltd, 2007. ISBN: 13:978-0-13-127498-3.

[19] M. Beaudoin and H. Jasak. Development of a Generalized Grid Interface for Turbomachinery Simulations with OpenFOAM. *Open Source CFD International Conference - Berlin*, 2008.

[20] O. Petit, A.I. Bosioc, H. Nilsson, S. Muntean, and R. F.Susan-Resiga. Unsteady Simulations of the Flow in a Swirl Generator, Using OpenFOAM. *International Journal of Fluid Machinery and Systems*, 4:199–208, 2008.

[21] P. Moradnia. CFD of Air Flow in Hydro Power Generators. Licentiate thesis, Division of Fluid Dynamics, Chalmers University of Technology, 2010.

[22] F.S. Lien and M.A. Leschziner. Computational Modeling of 3D Turbulent Flow in s-diffuser and Transition Ducts. *2nd International Symposium of Engineering Turbulence Modeling and Experiments*, 2:217–228, 1993.

[23] V. Yakhot, S.A. Orszag, S. Thangam, T.B. Gatski, and C.G. Speziale. Development of Turbulence Models for Shear Flows by a Double Expansion Technique. *Physics of Fluids*, 4(7), 1992. DOI: 10.1063/1.858424.

[24] T.H. Shih, W. Liou, A. Shabbir, Z. Yang, and J. Zhu. A New $k - \varepsilon$ Eddy-Viscosity Model for High Reynolds Number Turbulent Flows. *Computers and Fluids*, 24(3):227–238, 1995. 10.1016/0045-7930(94)00032-T.

[25] F.R. Menter. Two-Equation Eddy-Viscosity Turbulence Models for Engineering Applications. *AIAA Journal*, 32(8):1598–1605, 1994. ISSN: 0001-1452.

[26] J.F. Combès, P.F. Bert, and J.L Kueny. Numerical Investigation of the Rotor-Stator Interaction in a Centrifugal Pump Using a Finite Element Method. *A.S.M.E Fluids Engineering Division Summer Meeting*, 1997.

Paper V

Towards a Full Prediction of the 3D Unsteady Flow in the U9 Kaplan Turbine Model

By

O. Petit and H. Nilsson

Towards a Full Prediction of the 3D Unsteady Flow
in the U9 Kaplan Turbine Model

O.Petit[a,*], H.Nilsson[a]

[a]*Chalmers University of Technology, Department of Fluid Dynamics, Hörsalsvägen 7A, 41296 Gothenburg, Sweden*

Abstract

The present work presents unsteady simulations of the flow in the U9 Kaplan turbine model. The computational domain includes the complete geometry, from the high-pressure tank to the draft-tube outlet. The interaction between the rotating and stationary parts is treated with a sliding grid interface. The $k - \varepsilon$, RNG $k - \varepsilon$, realizable $k - \varepsilon$ and $k - \omega$ SST turbulence models are applied, and the results are compared with available LDA measurements. The comparisons show that the different turbulence models give quite similar results and compare well with the measurements up to the runner. The numerical results differ from the experimental results downstream of the runner, in the axi-symmetric part of the draft tube. One reason for this is that the blade clearances were omitted to save computational effort. Another reason is that the swirling flow in the adverse pressure gradient of the diffuser is very difficult to simulate.

Of particular interest is the impact of the intake pipe design, which comprises a sharp bend followed by a small cross-section area expansion. The results demonstrate a strong impact of the intake pipe on the flow at the spiral casing inlet, which suggests that the commonly used plug flow spiral casing inlet condition is inappropriate.

The simulations were done with the OpenFOAM-1.5-dev CFD tool, running in parallel on 32 cores, with a block-structured 13 million cell mesh.

Keywords: CFD, OpenFOAM, Kaplan, Hydro Power, Sliding Grid, Turbulent Flow

Nomenclature

LDA	laser Doppler anemometry
BEP	best efficiency point
CFD	computational fluid dynamics
D	runner diameter [m]
N	runner speed [rpm]
Q	flow rate [m^3/s]
H	head of the turbine [m]
r*	normalized radius
R	runner radius [m]
R_1	radius of the inlet of the spiral casing [m]

1. Introduction

For design and research in hydro turbines, the use of Computational Fluid Dynamics (CFD) has steadily increased in the past decades. CFD permits an extensive analysis of the flow that gives a better understanding of the flow in the whole machine. In recent years, improved computational algorithms and hardware

---

*Corresponding author
Email addresses: `olivierp@chalmers.se` (O.Petit), `hani@chalmers.se` (H.Nilsson)

development have given convincing evidence that CFD calculations are reliable tools for analyzing the unsteadiness of the flow in hydro turbines [1]. Nowadays, it is common practice to simulate the flow in isolated parts of the hydro turbines to understand the development of the flow, particularly under the design phase. Sometimes the turbine is simulated together with the distributor and draft tube, using the steady state frozen rotor or stage approaches. The frozen rotor approach mostly includes the complete runner, but its position is frozen and the rotation is accounted for by source terms. The frozen rotor approach yields an unphysical advection of the wakes between the rotating and the steady parts of the domain [2]. The stage approach also applies source terms for the rotation, but instead applies a circumferential average at the interface between the rotating and stationary parts of the domain. Thus, it is sufficient to include only one blade in each stage and assume that the flow is periodic for the other blades in the same stage. The stage approach does not include the rotor-stator interaction through tangential variation, such as wakes. Thus, although the frozen rotor and stage approaches give a good overview of the overall behavior of the flow, those approaches do not correctly predict the rotor-stator interacion.

To fully understand the flow and accurately predict the interaction between the different components of the hydro turbine, the whole geometry needs to be included in the computational domain, and 3D transient calculations need to be performed. Since such simulations are computationally heavy and time consuming, few such papers have been published that highlight 3D unsteady simulation of the whole hydro turbine. Ruprecht *et al.* [3] presented early work on the unsteadiness of the flow in a Francis turbine, Labrecque *et al.* [4] studied the interactions between the different components of a Francis turbine and Li *et al.* [5] focused on the transients phenomena in a Francis turbine. To date, most of the work focused on 3D unsteady flow have been done for Francis turbines. Liu *et al.* [6] is one of few such studies in the Kaplan turbine.

Common practice for full water turbine simulations is to set a plug flow inlet boundary condition at the inlet of the spiral casing. However the upstream penstock is sometimes bent with a sharp angle close to the inlet of the spiral casing. In this case, a plug flow at the inlet of the spiral casing is not realistic [7]. Such a bent in the inlet pipe is present in the Porjus hydro power plant, located in the north of Sweden. One of its Kaplan units, called U9, was replaced by a research prototype during the past decade. The new turbine is somewhat smaller than the previous unit, and a sharply bent pipe was inserted into the old penstock when assembling the new prototype. The prototype Kaplan turbine has a diameter of 1.55 m and an operational head of 55 m, with a maximum discharge capacity of 20 m$^3/s$ for a power of 10 MW. It is composed of a bent inlet pipe, a spiral casing, 18 stay vanes, 20 guide vanes, six runner blades and an elbow draft tube. A 1:3.1 scale model of the same geometry is available for scientific studies, and a detailed measurement database is available to validate CFD methods [8].

The present work presents 3D unsteady simulations of the full U9 Kaplan turbine model, from the high pressure tank to the outlet of the draft tube, using a 13 million cell mesh. Four different turbulence models and the wall-function approach were employed. This becomes costly when using proprietary software, where there is an additional license cost for each process. The present work uses the OpenFOAM-1.5-dev CFD tool to make the calculations. OpenFOAM is an Open Source library written in C++ [9]. It is based on the finite volume method and has proven to be as accurate as proprietary codes for many applications [10, 11, 12]. The results are analyzed and compared in detail with the velocity measurements performed by Mulu *et al.* [13, 14, 15] and Jonsson *et al.* [16] at different positions in the Kaplan turbine model.

2. Test rig, test conditions and experimental database

The U9 Kaplan turbine test rig, located at Vattenfall Research and Development in Älvkarleby, Sweden, is shown in Fig. 1. Detailed measurements were made by Mulu *et al.* [13, 14, 15] and Jonsson *et al.* [16]. The measurements were carried out at three different loads, at best operating point of the turbine and at two off-design operating points (to the left and right of the propeller curve). Table 1 summurizes the working guide vane angle and the volume flow rate for the three working conditions.The operational net head $H = 7.5$ m, the runner blade angle $\beta = 0.8$ and a runner speed of n=696.3 rpm were used throughout the entire period of measurements.

The velocity measurements were made using a two-component LDA (Laser Doppler Anemometry) technique. The measurements were made at the inlet of the spiral casing, in the spiral casing and in the draft
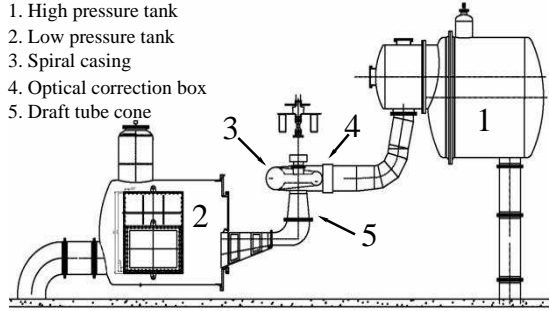
Figure 1: Test rig for the U9 Kaplan turbine model

Operating point	Left	BEP	Right
Guide vane angle (°)	20	26	32
Volume flow rate (m^3/s)	0.62	0.71	0.76

Table 1: Test conditions parameters

(a) Measurement positions at the inlet of the spiral casing
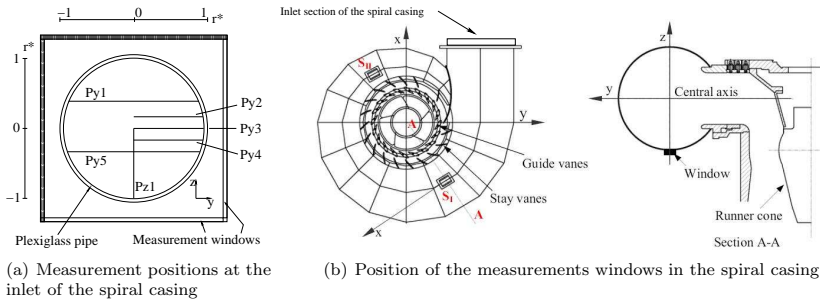
(b) Position of the measurements windows in the spiral casing

Figure 2: LDA measurement positions at the inlet of the spiral casing (a) and inside the spiral casing (b). At the inlet of the spiral casing, the axial velocity and the velocity orthogonal to each measurement axis were measured along five horizontal (P_{y1}-P_{y5}) and one vertical axis (P_{z1}). In the spiral casing, the tangential and radial velocity were measured along the z-axis through two windows, SI and SII, placed at the center of the spiral casing.

tube cone, see Figs. 2 and 3.

The inlet of the spiral casing is a circular pipe with an inner radius of 316mm. To avoid refraction caused by the surface curvature of the inlet pipe, a 290mm long square optical box filled with index matching liquid was placed around the pipe [13]. Using the LDA technique, the axial velocity and the velocity orthogonal to each measurement axis were measured along five horizontal (P_{y1}-P_{y5}) and one vertical axis (P_{z1}), see Fig. 2(a). It was only possible to measure half-way through the pipe, so axes P_{y1} and P_{y5} were measured in two steps from two sides.

In the spiral casing, two windows were installed at the bottom, and at the angular positions -56.25° for window SI and -236.25° for window SII, see Fig. 2(b). The windows were placed at the center of the casing. The tangential and radial velocity are measured using the LDA technique, starting from each window along the z-direction. It was not possible to cover the entire height of the casing.

In the draft tube cone, windows were mounted at four different angular positions, a: 0°, b: 90°, c: 180° and d: 270° see Fig. 3. The LDA velocity measurements were made at sections I, II and III for the four
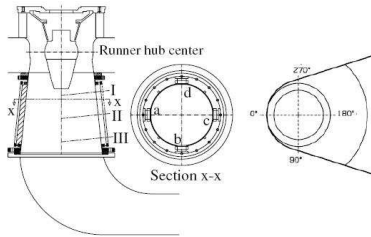
3

Figure 3: LDA window locations in the draft tube cone where a is at 0°, b at 90°, c at 180° and d at 270°. The velocity measurements were made at sections I, II and III.

different angular positions. For these measurements, the axis is orthogonal to the window and has an angle of 6.1° with the draft tube cone axis. Thus, the tangential velocity is measured while a combination of the axial and radial velocity is obtained for the other component. However, the small angle ($\alpha = 6.1°$) combined with a comparatively small radial velocity allows the assumption that the measured velocity is the axial velocity. The error is estimated to be below 1% [14].

The current work focuses on comparisons with the velocity measurements, although pressure measurements made in the spiral casing and in the draft tube are also available [15, 16, 17]. The results presented in the following sections focus on one working load of the turbine, at best efficiency point.

3. Computational domain, and numerical set-up

The computational domain is shown in Fig. 4. It includes the last part of the high-pressure tank, the curved inlet pipe, the spiral casing, the distributor, the Kaplan runner and the draft-tube. In the rig, a perforated plate is located just before the last part of the high pressure tank, approximately yielding a plug flow. This cross-section was thus selected as the most appropriate location for the inlet boundary in the present work. The computational mesh is block structured and was generated using the ICEM-CFD
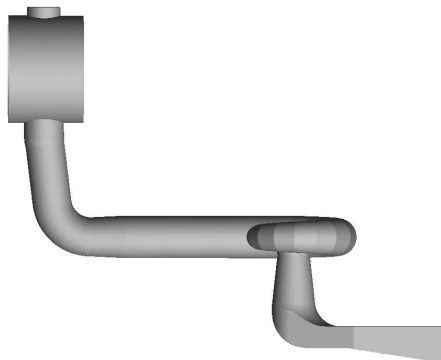

Figure 4: Computational domain

software, see Fig. 5. The different parts were meshed separately and are coupled using the General Grid Interface (GGI) implemented in OpenFOAM by Beaudoin and Jasak [18]. The runner blade passage was meshed using O-grids around the blades and H-grids between the blades. It was made for one blade and copied to the other five blades. The runner blade end tip clearances and the guide vanes clearances are not

4

included in the present simulations. The mesh has a total of about 13 million hexahedral cells. The cell angles are between $30°$ and $150°$, but 90% of the angles are between $60°$ and $120°$.

The continuity equation and the three-dimensional incompressible unsteady Reynolds-averaged Navier-Stokes equations are solved. The domain is coupled between the rotor and stator using the sliding grid approach. This transient approach rotates the runner part of the mesh with respect to the stationary parts at each time step. The local fluxes between the rotating and stationary parts of the domain are determined by a GGI that updates every time step. The rotor-stator interaction is thus fully resolved.

The eddy-viscosity assumption is used to model the Reynolds stress tensor. An extensive comparison of the turbulence models available in OpenFOAM was made by Moradnia [19]. The Moradnia's focus was particularly on high and low Reynolds number, two-equation, eddy-viscosity turbulence models, as well as Reynolds Stress Transport turbulence models. The outcome of the study of Moradnia was that four high Reynolds turbulence models were better at predicting the flow, while maintaining numerical stability. Those are the $k - \varepsilon$ [20], realizable $k - \varepsilon$ [21], RNG $k - \varepsilon$ [22] and the $k - \omega$ SST [23] turbulence models. Those models have thus been chosen to be compared to each other and to the measurements in the present study.

The flow rate, turbulence intensity and viscosity ratio are specified at the inlet of the computational domain. The velocity is set to a plug flow, according to the experimental volume flow, and the turbulence intensity is assumed to be 10% with a turbulent to laminar viscosity ratio of 10. At the outlet, with the exception of the pressure, all variables are given a zero gradient boundary condition. All the walls use a wall-function boundary condition, appropriate for the y^+ values obtained (50-70). The time step was fixed to $2.4e^{-4}$ s, which gives a maximum Courant number of 10. This corresponds to a rotation of the runner of about $1°$ per time step. Previous studies have shown that this angular time step is small enough to allow the transient solver to accurately capture the unsteadiness of the flow [24]. The number of iterations per time step in the transient SIMPLE algorithm is set to 5. This number of iterations is sufficient to reduce the residuals by three orders of magnitude. The final residuals are below 10^{-8} except for the pressure, which has a final residual of 10^{-5}. A second-order linear-upwind scheme [25] is used to discretize the convection terms. The second-order backward scheme is used to discretize the time derivative.
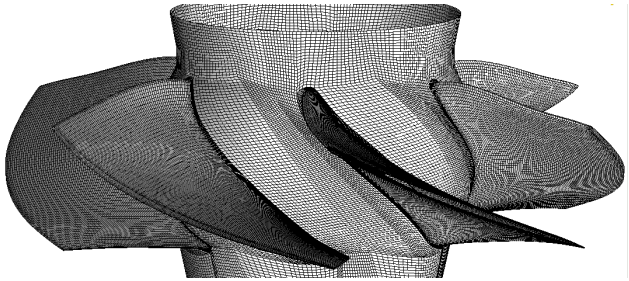
The calculations are carried out on a cluster, using 8 nodes equipped with 4 cores each. Before any analysis is performed, the simulations run for 30 full runner rotations to make sure that the flow is fully developed.
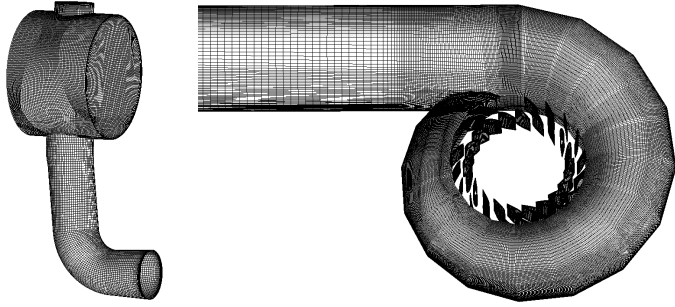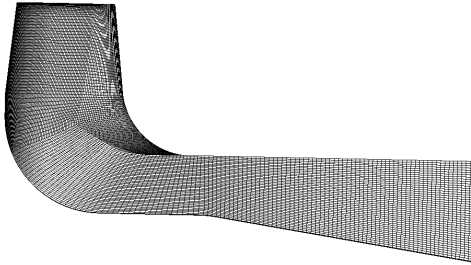
(a) Part of high-pressure tank, inlet pipe, and spiral casing
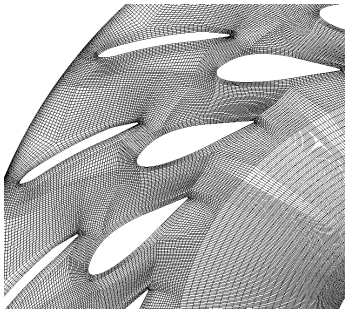
(b) Stay and guide vanes

(c) Runner

(d) Draft tube

Figure 5: Close-up of different parts of the computational mesh

4. Results and discussion

The following sections report the unsteady numerical results. The simulation using the standard $k - \varepsilon$ turbulence model is first presented, and the velocity components are compared with the measurements at the inlet of the spiral casing, in the spiral casing and in the draft tube. The results from the four simulations using the four different turbulence models, the $k - \varepsilon$, RNG $k - \varepsilon$, realizable $k - \varepsilon$ and $k - \omega$ SST turbulence models, are then compared to each other and to the measurements.

At the inlet of the spiral casing, all the kinematic quantities are normalized with the velocity from the flow rate and the spiral casing inlet radius, $R_1 = 0.316$ m. The radii were made dimensionless with the same inlet radius, and $r^* = 0$ at the center of the pipe, as shown in Fig. 2(a). The axial velocity is defined as positive in the direction of the flow.

In the spiral casing, all the kinematic quantities are normalized with the same reference velocity as for the inlet of the spiral casing. The survey axis, z, was made dimensionless with the same inlet radius. Based on the measurements, the radial velocity is defined as positive towards the wicket gate, and the tangential velocity is defined as positive in the flow direction. The measurements axes start at $z^* = 0$ at the windows, i.e. at the lower wall of the spiral casing. All the kinematic quantities in the draft tube are normalized with the velocity obtained from the flow rate and the radius of the runner, $R = 0.25$ m. The radii were made dimensionless with the runner radius. The positive directions for the axial and tangential velocities are defined vertically downward through the draft tube cone and clockwise, seen from the top of the runner, respectively.

4.1. Unsteady results with the k-ε turbulence model

Figure 6 shows an overview of the velocity distribution in the U9 Kaplan turbine model, computed using the $k - \varepsilon$ turbulence model. A recirculation is present after the bend of the inlet curved pipe. The separation is generated by the sudden change of direction of the pipe, and by the small increase in area. This disturbance in the flow is transported to the inlet of the spiral casing, and the flow that enters the spiral casing is thus non-uniform. This emphasizes the importance of setting the inlet boundary condition in an appropriate location. The standard approach is to set a plug flow at the inlet of the spiral casing. This does not include the disturbance created by the curved inlet pipe. This might affect the solution in the spiral casing and runner, and might thus give an incorrect prediction of the downstream flow. From the spiral casing and wicket gate, a quite uniform flow is distributed to the runner. Below the runner, the runner blade wakes are visible until at least the end of the runner cone. They are then diffused in the draft tube cone.

Figure 7 shows the axial velocity at the inlet of the spiral casing at 5 different axes where the LDA measurements were taken. The M-shape characteristics of the velocity distribution after the bend appear in both the measured and computed velocity. Although the 3D unsteady calculation predicts this behavior, the recirculation is over-estimated. The axial velocity is under-predicted at the center of the pipe and over-estimated close to the wall.

Figure 8 presents the radial and tangential velocity profiles at the two spiral casing windows. The calculated radial velocity presents a slightly more intense secondary flow at window SI than the measured one. The experimental radial velocity preserves its shape until window SII, where the simulation yields a more constant radial velocity.

Figsures 9, 10 and 11 show the measured and computed axial and tangential velocity profiles at sections I, II and III. The unsteady wakes from the runner blades are still visible at section I but are advected downstream of the draft tube cone and do not appear at sections II and III. Both the experimental and numerical velocity profiles have a negligible variation between positions a, b, c and d. Thus, for clarity, the velocity profiles are presented only for window a. Although some of the behavior of the flow is rather well predicted, there are significant differences between the measured and computed velocity profiles. A vortex is created below the runner cone, generating a region where high velocities and large velocity gradients can be found. This is not well predicted by the simulation. The computed velocities at $r^* \simeq 0.2$ do not show the same increase as the experimental ones. The shroud boundary layer is much wider in the numerical results than is found in of the experimental results. These differences between the measured and simulated

7

velocity profiles are most likely the result of the simplifications made in the computational domain. The clearances for the guide vanes and the runner blades are not included in the present work in order to reduce computational effort. Nilsson [26] showed that the runner blade hub and shroud tip clearances are of great importance for the flow below the runner. This secondary flow delays the separation at the walls and reduces the vortex radius below the runner cone. The flow separates early in the present simulation, as shown in Fig. 12, both at the shroud of the draft tube and at the runner cone. By adding the tip clearances in the computational domain, the secondary flow that is induced should help the flow to stay attached to the shroud and runner cone, yielding much better agreement with the experimental velocity profiles.

4.2. Comparison between four turbulence models

The $k - \varepsilon$ [20], realizable $k - \varepsilon$ [21], RNG $k - \varepsilon$ [22] and the $k - \omega$ SST [23] turbulence models are compared here for the flow in the full U9 model, from upstream of the tank to the outlet of the draft tube. Figure 13 presents the normalized axial velocity at the inlet of the spiral casing for the four turbulence models. The $k - \varepsilon$ turbulence models yield similar results, while the $k - \omega$ SST turbulence model seems to more accurately predict the separation at the bend of the inlet pipe. The calculation using the $k - \omega$ SST turbulence model however still over-estimates the velocity close to the lower wall of the inlet pipe. The radial and tangential velocity profiles in the spiral casing for the different turbulence models are presented in Fig. 14. The predicted velocity profiles at window SI for the $k - \omega$ SST turbulence model are in very good agreement with the measurements. The other turbulence models over-predict the secondary flow. This might be a result of the over-estimation of the detached region after the inlet pipe bend. None of the turbulence models succeed in capturing the behavior of the radial velocity at window SII and predict instead a quasi-constant radial velocity throughout the survey axis.

Fig. 15 shows the axial and tangential velocity profiles in the draft tube cone, at sections Ia, IIa and IIIa. None of the models accurately predict the vortex below the runner cone, and the shroud boundary layer is too wide for all four calculations. This reinforces the hypothesis that the major differences between the computed and measured velocity profiles below the runner originate in the lack of runner blade end tip clearances rather than the choice of turbulence model.
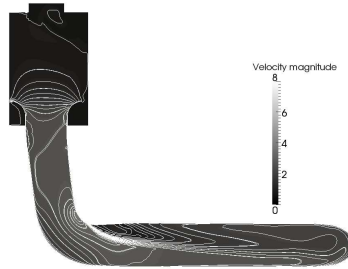
(a) Velocity magnitude in the inlet pipe bend, at mid-span
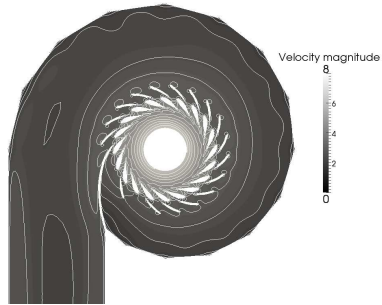
(b) Velocity magnitude in the spiral casing and distributor, at mid-span
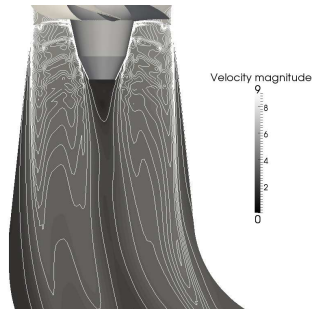
(c) Velocity magnitude in the draft tube cone, at mid-span

Figure 6: Computed velocity magnitude in different parts of the computational domain, using the $k - \varepsilon$ turbulence model
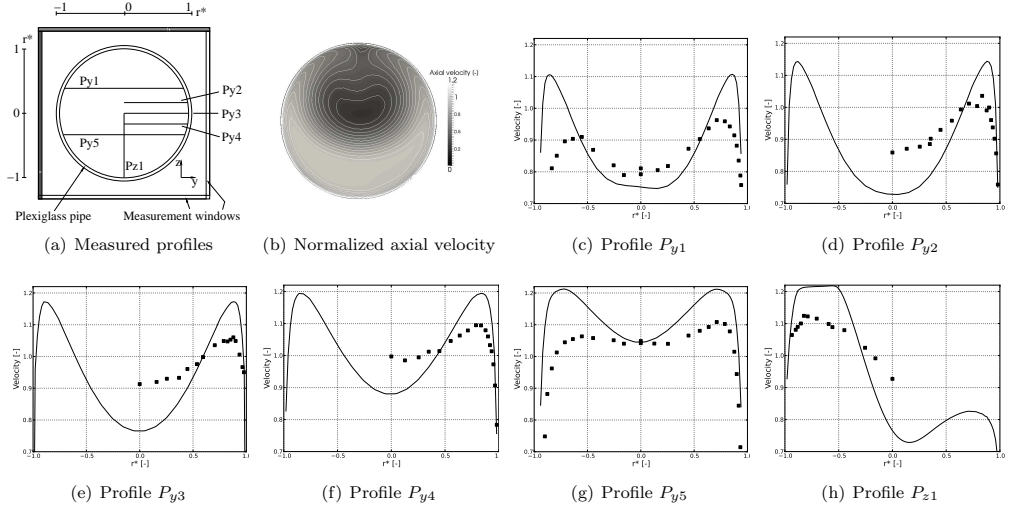
(a) Measured profiles (b) Normalized axial velocity (c) Profile P_{y1} (d) Profile P_{y2}

(e) Profile P_{y3} (f) Profile P_{y4} (g) Profile P_{y5} (h) Profile P_{z1}

Figure 7: Normalized axial velocity profiles at the axes used for the LDA measurements. The solid line and the squares represent the computed and measured distributions, respectively. The calculation was made using the $k-\varepsilon$ turbulence model.
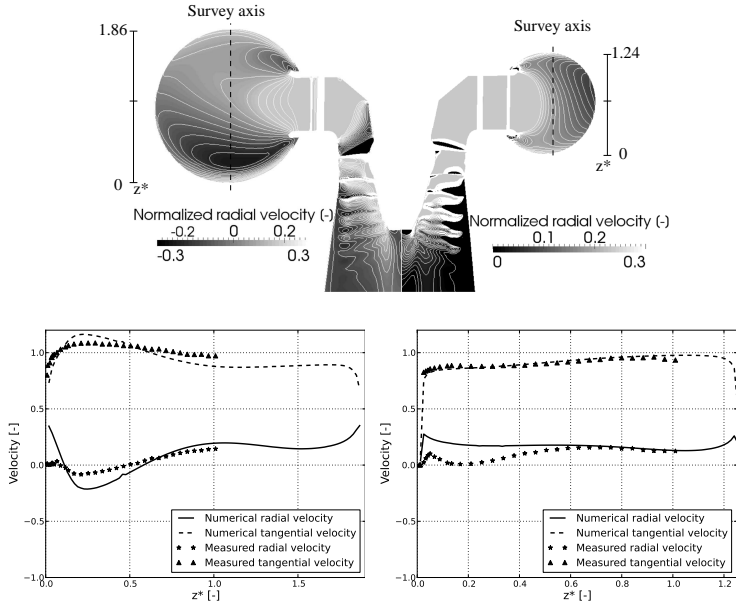
Figure 8: Radial and tangential velocity profiles at windows SI and SII in the spiral casing. The radial velocity is defined as positive towards the wicket gate. The tangential velocity is constant in the flow direction. The positions of the two windows, SI and SII, can be found in Fig. 2(b). The calculation was made using the $k-\varepsilon$ turbulence model.
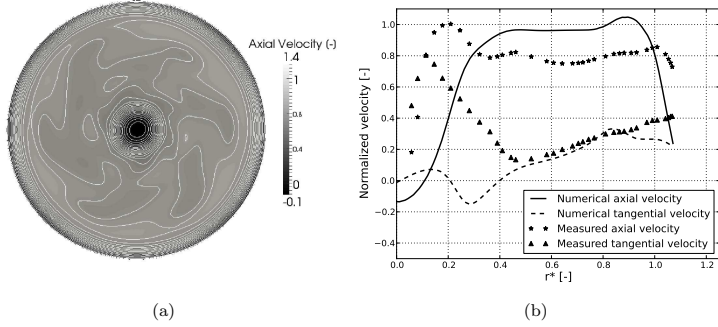
Figure 9: Normalized axial velocity at section I (a) and normalized tangential and axial velocity profiles at section Ia (b) using the $k - \varepsilon$ turbulence model. The position of section Ia can be found in Fig. 3.
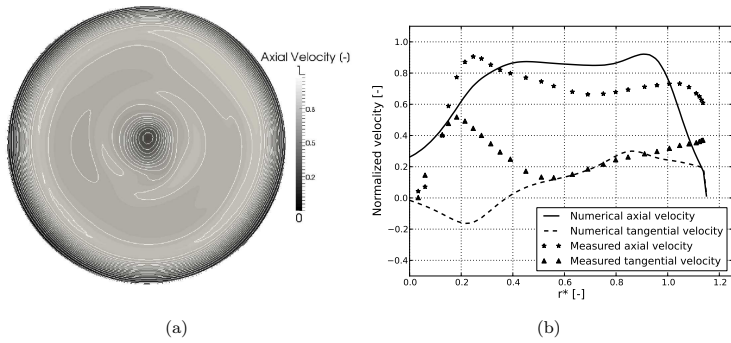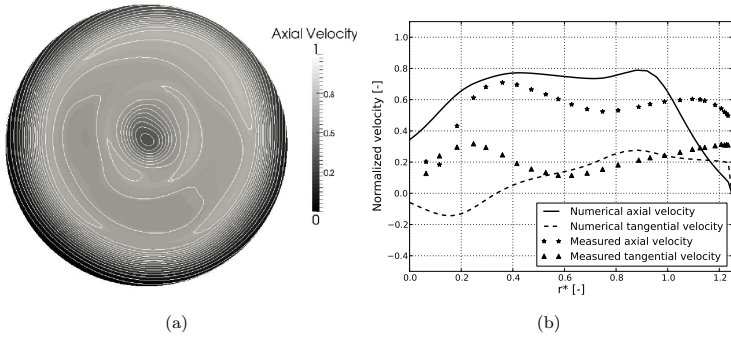

Figure 10: Normalized axial velocity at section II (a) and normalized tangential and axial velocity profiles at section IIa (b) using the $k - \varepsilon$ turbulence model. The position of section IIa can be found in Fig. 3.

Figure 11: Normalized axial velocity at section III (a) and normalized tangential and axial velocity profiles at section IIIa (b) using the $k - \varepsilon$ turbulence model. The position of section IIIa can be found in Fig. 3.
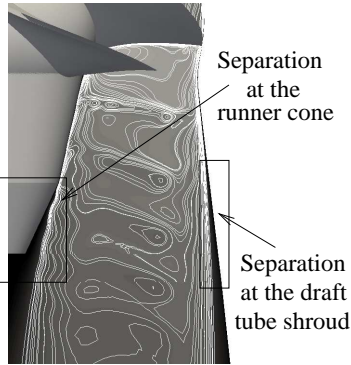
11

Figure 12: Close-up of Fig. 6(c). The wakes of the runner blades in the draft tube cone are visible, as are the separation at the draft tube shroud and the runner cone.

(a) Profile P_{y1}

(b) Profile P_{y2}

(c) Profile P_{y3}

(d) Profile P_{y4}

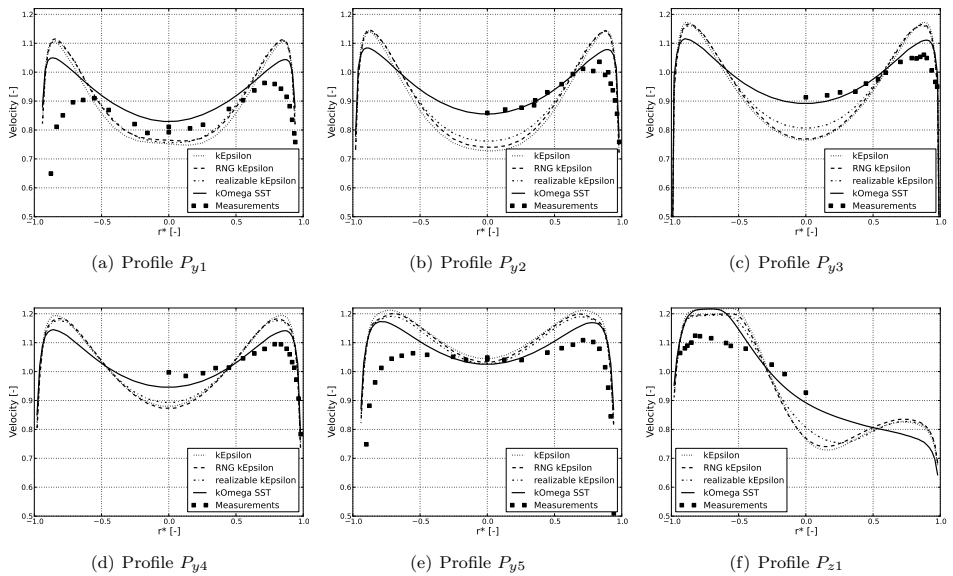(e) Profile P_{y5}

(f) Profile P_{z1}

Figure 13: Comparison of the normalized axial velocity profiles for the $k - \varepsilon$, realizable $k - \varepsilon$ RNG $k - \varepsilon$ and $k - \omega$ SST turbulence models at the axes used for the LDA measurements.
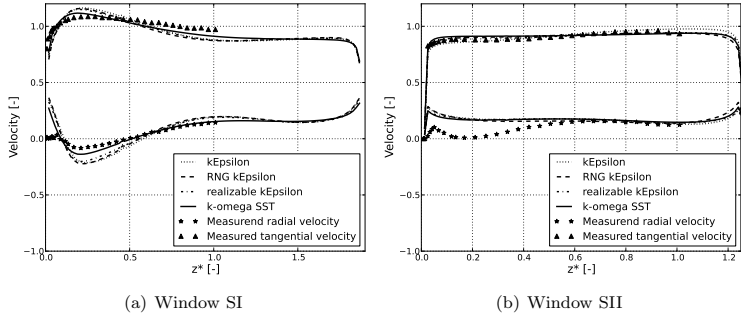
Figure 14: Comparison of the normalized radial and tangential velocity profiles for the $k - \varepsilon$, realizable $k - \varepsilon$, RNG $k - \varepsilon$ and $k - \omega$ SST turbulence models at windows SI and SII in the spiral casing.
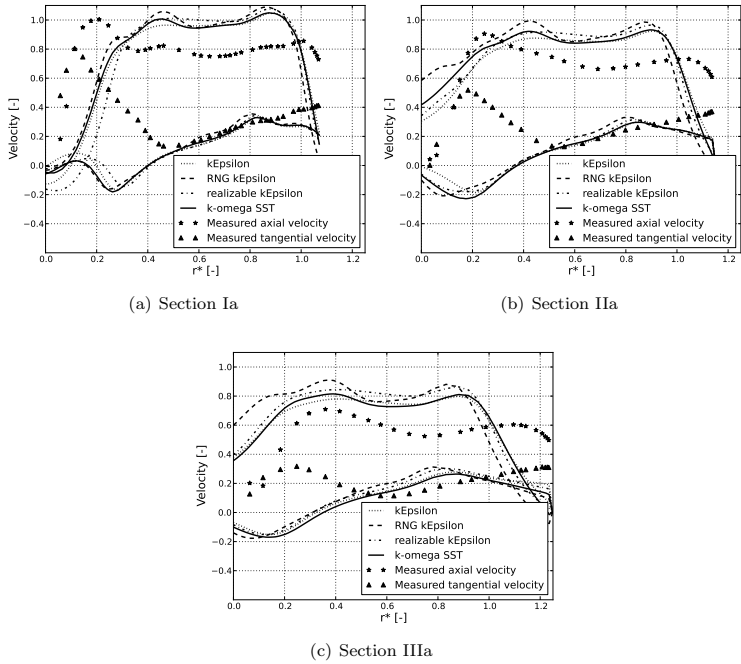

Figure 15: Comparison of the normalized axial and tangential velocity profiles for the $k - \varepsilon$, realizable $k - \varepsilon$, RNG $k - \varepsilon$ and $k - \omega$ SST turbulence models in the draft tube at sections Ia (a), IIa (b) and IIIa (c).

13

5. Conclusion

Unsteady calculations are presented of the flow in a full Kaplan turbine model, from the high pressure tank through the curved inlet pipe, spiral casing, stay and guide vanes, runner and into the draft tube. The rotor-stator interaction is fully resolved using the sliding grid interface, based on GGI available in OpenFOAM-1.5-dev. Four turbulence models were used to perform the calculations, the $k - \varepsilon$, realizable $k - \varepsilon$, RNG $k - \varepsilon$ and the $k - \omega$ SST turbulence models. The results were compared with the experimental investigation reported by Mulu *et al.* [13, 14, 15]. The simulations show that the disturbance created by the inlet pipe bend is transported to the inlet of the spiral casing. The strong impact of the intake pipe on the flow at the spiral casing inlet suggests that the commonly used plug flow spiral casing inlet boundary condition is inappropriate. This disturbance needs to be included in order to set a reasonable boundary condition at the inlet of the spiral casing. The $k - \omega$ SST turbulence model shows the best agreement with the measurements before the runner. Below the runner, the simulations fail to accurately predict the experimental velocity profiles. That none of the turbulence models improves the flow prediction in the draft tube reinforces the hypothesis that the difference in the draft tube between numerical and experimental results is due to the lack of runner blade tip clearances. The general behavior of the flow is nevertheless captured, and the calculated velocity profiles are of the same magnitude as the measured ones.

6. Acknowledgments

References

[1] H. Keck and M. Sick. Thirty Years of Numerical Flow Simulation in Hydraulic Turbomachines. *Acta Mechanica*, 201(1-4):211–229, 2008. DOI: 10.1007/s00707-008-0060-4.

[2] O. Petit, M. Page, M. Beaudoin, and H. Nilsson. The ERCOFTAC Centrifugal Pump OpenFOAM Case-Study. *3rd IAHR International Meeting of the Workgroup on Cavitation and Dynamic Problems in Hydraulic Machinery and Systems - Brno*, 2009.

[3] A. Ruprecht. Unsteady Flow Analysis in Hydraulic Turbomachinery. *Proceedings of the 20th IAHR Symposium on Hydraulic Machinery and Systems*, 2000.

[4] Y. Labrecque, M. Sabourin, and C. Deschênes. Numerical Simulation of a Complete Turbine and Interaction between Components. *Modeling, Testing and Monitoring for Hydro Powerplants*, 1996.

[5] J. Li, J. Yu, and Y. Wu. 3D Unsteady Turbulent Simulations of the Runaway Transients of the Francis Turbine. *Journal of Hydroelectric Engineering*, 2010. DOI: CNKI:SUN:SFXB.0.2008-06-029.

[6] S. Liu, Q. Chen, and Y. Wu. Unsteady Cavitating Turbulent Flow Simulation in a Kaplan Turbine. *2nd International Meeting of the Workgroup on Cavitating and Dynamic Problems in Hydraulic Machinery and Systems*, 2007.

[7] B. Mulu and M. Cervantes. Effects of Inlet Boundary Conditions on Spiral Casing Simulation. *Scientific Bulletin of the "Politehnica" University of Timisoara Transactions on Mechanics*, Tom 52(66), Fascicola 6, 2007.

[8] M.J. Cervantes, I. Jansson, A. Jourak, S. Glavatskikh, and J.O. Aidanpää. Porjus U9, a Full-scale Hydropower Research Facility. *24th IAHR Symposium on Hydraulic Machinery and Systems - Foz Do Iguassu*, 2008. ISBN: 978-85-60858-13-1.

[9] H.G. Weller, G. Tabor, H. Jasak, and C. Fureby. A Tensorial Approach to Computational Continuum Mechanics using Object-Oriented Techniques. *Computers in Physics*, 12(6):620–631, 1998.

[10] O. Petit, H. Nilsson, T. Vu, O. Manole, and S. Leonsson. The Flow in the U9 Kaplan Turbine - Preliminary and Planned Simulations Using CFX and OpenFOAM. *24th Symposium on Hydraulic Machinery and Systems*, 2008.

[11] H. Nilsson and L. Davidson. A Numerical Comparison of Four Operating Conditions in a Kaplan Water Turbine, Focusing on Tip Clearance Flow. *20th IAHR Symposium on Hydraulic Machinery and Systems*, 2000.

[12] S. Muntean, H. Nilsson, and R.F. Susan-Resiga. 3D Numerical Analysis of the Unsteady Turbulent Swirling Flow in a Conical Diffuser Using Fluent and OpenFOAM. *3rd IAHR International Meeting of the Workgroup on Cavitation and Dynamic Problems in Hydraulic Machinery and Systems - Brno*, 2009.

[13] B. Mulu and M. Cervantes. Experimental Investigation of a Kaplan Model with LDA. *33rd IAHR Congress: Water Engineering for a Sustainable Environment*, 2009.

[14] B. Mulu and M. Cervantes. LDA Measurements in a Kaplan Spiral Casing Model. *13th International Symposium on Transport Phenomena and Dynamics of Rotating Machinery*, 2010.

[15] B. Mulu, P. Jonsson, and M. Cervantes. Experimental Investigation of a Kaplan Draft Tube - Part I: Best Efficiency Point. *Journal of Applied Energy*, 93:695–706, 2012. DOI: 10.1016/j.apenergy.2012.01.004.

[16] P. Jonsson, B. Mulu, and M. Cervantes. Experimental Investigation of a Kaplan Draft Tube - Part II: Off-Design Conditions. *Journal of Applied Energy*, 94(2):71–83, 2012. DOI: 10.1016/j.apenergy.2012.01.032.

[17] P. Jonsson and M. Cervantes. Time Resolved Pressure Measurements on a Kaplan Model. *33rd IAHR Congress: Water Engineering for a Sustainable Environment*, 2009.

[18] M. Beaudoin and H. Jasak. Development of a Generalized Grid Interface for Turbomachinery Simulations with Open-FOAM. *Open Source CFD International Conference - Berlin*, 2008.

[19] P. Moradnia. CFD of Air Flow in Hydro Power Generators. Licentiate thesis, Division of Fluid Dynamics, Chalmers University of Technology, 2010.

[20] F.S. Lien and M.A. Leschziner. Computational Modeling of 3D Turbulent Flow in s-diffuser and Transition Ducts. *2nd International Symposium of Engineering Turbulence Modeling and Experiments*, 2:217–228, 1993.

[21] V. Yakhot, S.A. Orszag, S. Thangam, T.B. Gatski, and C.G. Speziale. Development of Turbulence Models for Shear Flows by a Double Expansion Technique. *Physics of Fluids*, 4(7), 1992. DOI: 10.1063/1.858424.

[22] T.H. Shih, W. Liou, A. Shabbir, Z. Yang, and J. Zhu. A New $k - \varepsilon$ Eddy-Viscosity Model for High Reynolds Number Turbulent Flows. *Computers and Fluids*, 24(3):227–238, 1995. 10.1016/0045-7930(94)00032-T.

[23] F. Menter and T. Esch. Elements of Industrial Heat Transfer Predictions. *16th Brazilian Congress of Mechanical Engineering*, 2001.

[24] O. Petit, A.I. Bosioc, H. Nilsson, S. Muntean, and R. F.Susan-Resiga. Unsteady Simulations of the Flow in a Swirl Generator, Using OpenFOAM. *International Journal of Fluid Machinery and Systems*, 4:199–208, 2008.

[25] H.K. Versteeg and Malalasekera W., editors. *An Introduction to Computational Fluid Dynamics: the Finite Volume Method*. Pearson Education Ltd, 2007. ISBN: 13:978-0-13-127498-3.

[26] H. Nilsson. Evaluation of OpenFOAM for CFD of Turbulent Flow in Water Turbines. *23rd IAHR Symposium on Hydraulic Machinery and Systems*, 2006.